Parameter Evaluation and Sensitivity Analysis for an Automotive Damper Model

A Thesis

Presented in Partial Fulfillment of the Requirements for the Degree Master of Science in the Graduate School of The Ohio State University

By

Ben J. Thornton, B.S.

Graduate Program in Mechanical Engineering

The Ohio State University

2012

Master's Examination Committee:

Dr. Marcelo J. Dapino, Advisor

Dr. Gary Heydinger

Abstract

Physical models are commonly used in the automotive industry. Accurate models exist for most automotive systems. However, few accurate models have been developed to model the individual components of automotive suspension dampers. Damper modeling is challenging due to the complexities associated with fluid flow and clearance nonlinearities, fluid-structure coupling, and overall sensitivity to parameter variations. This thesis focuses on the evaluation of gas bulk modulus, oil bulk modulus, Coulomb friction, effective mass of the body and valve resistance. The effect of these parameters on damper performance are analytically evaluated. The results show that the model is most sensitive to valve fluid resistance. Two experiments are presented. In the first experiment a simplified loading pattern was applied to the shims using steel forks. In the second experiment the displacement of the shims was measured while fluid was flowing through the valve. Although these experiments did not match exactly, valve shim stiffness calculated from each experiment led to accurate results when the model was run with these stiffness values. The overall model accuracy is adequate, though further work is needed to improve th modeling of shims and other components.

Acknowledgments

I would like to express my sincere gratitude to Professor Marcelo Dapino for providing with me with the resources, guidance, and support that allowed me to complete this thesis. Your expertise in the field was greatly appreciated throughout the course of this project.

I would also like to thank Professor Gary Heydinger for attending my defense as a member of my examination committee and for thoroughly reviewing my thesis. I am grateful for the advice and critiques that you have offered and I believe that they have significantly improved this document.

I would like to thank John Yu, and Bryan Johnson from Honda R&D for providing your time and expertise. I am honored to be able to carry out a project with such a prestigious research facility.

I would like to thank Tony King for working side by side with me on this project. Tony made significant contributions to the project which helped keep the project on schedule while maintaining high standards of quality.

Thank you to Brian Schoeny and Showa R&D for the time and resources that were devoted to this project. On several occasions Brian provided his time and expertise at no benefit to himself.

Finally, I would like to thank Keith Malarik for operating the HRA dynamometer and for your help in troubleshooting the fluid shim stiffness testing.

Vita

April 7,1988 .... Born - Columbus, OH

June 2006 .... Bishop Watterson High School

August 2011 .... B.S. Mechanical Engineering, Magna Cum Laude, The Ohio State University

2011 - Present .... Graduate Research Associate, The Ohio State University

Fields of Study

Major Field: Mechanical Engineering

Studies in Mechanical Dynamics: Dr. Marcelo Dapino

Table of Contents

List of Tables

List of Figures

List of Symbols

Symbol	Description	Unit
F_1	External Force Applied to Damper Rod	lbf
F_2	External Force Applied to Damper Body	lbf
F_r	Coulomb friction force	lbf
X	Displacement of Damper Rod	in
Y	Displacement of Damper Body	in
Z	Relative Displacement of Damper Rod With Respect to the Damper Body	in
L_1	Initial Length of Chamber 1	in
L_2	Initial Length of Chamber 2	in
m_r	Mass of Rod and Piston	slug·ft/in
m_b	Mass of Damper Body	slug·ft/in
P_1	Pressure in Chamber 1	psi
P_2	Pressure in Chamber 2	psi
P_3	Pressure in Chamber 3	psi
V_1	Volume of Chamber 1	psi
V_2	Volume of Chamber 2	psi
V_{31}	Volume of Gas in Chamber 3	psi
V_{32}	Volume of Oil in Chamber 3	psi
β_1	Effective Bulk Modulous of Oil in Chamber 1	psi
β_2	Effective Bulk Modulous of Oil in Chamber 2	psi
β_{31}	Effective Bulk Modulous of Oil in Chamber 3	psi

Symbol	Description	Unit
β_{32}	Effective Bulk Modulous of Gas in Chamber 3	psi
k_1	Stiffness of Shim Stack 1	lbf/in
k_2	Stiffness of Shim Stack 2	lbf/in
k_3	Stiffness of Shim Stack 3	lbf/in
k_4	Stiffness of Shim Stack 4	lbf/in
x_1	Displacement of Shim Stack 1	in
x_2	Displacement of Shim Stack 2	in
x_3	Displacement of Shim Stack 3	in
x_4	Displacement of Shim Stack 4	in
q_{12}	Flow Through Check Valve 12	in^3/s
q_{22}	Flow Through Check Valve 22	in^3/s
q_{32}	Flow Through Check Valve 32	in^3/s
q_{42}	Flow Through Check Valve 42	in^3/s
q_{11}	Flow Through Bleed Valve 11	in^3/s
q_{31}	Flow Through Bleed Valve 31	in^3/s
$q_{\beta 1}$	Effective Flow Due to Fluid Compressibility in Chamber 1	in^3/s
$q_{\beta 2}$	Effective Flow Due to Fluid Compressibility in Chamber 2	in^3/s
$q_{\beta 3}$	Effective Flow Due to Fluid Compressibility in Chamber 3	in^3/s
A_r	Area of Rod	in^2
A_p	Area of Piston	in^2
n_{11}	Number of Holes That Make Up Bleed Valve 11	–
n_{31}	Number of Holes That Make Up Bleed Valve 31	–
n_{12}	Number of Holes That Make Up Check Valve 13	–
n_{22}	Number of Holes That Make Up Check Valve 22	–
n_{32}	Number of Holes That Make Up Check Valve 32	–
n_{42}	Number of Holes That Make Up Check Valve 42	–

Symbol	Description	Unit
C_{d11}	Dynamic Discharge Coefficient For Bleed Valve 11	–
C_{d31}	Dynamic Discharge Coefficient For Bleed Valve 31	–
C_{d12}	Dynamic Discharge Coefficient For Bleed Valve 12	–
C_{d22}	Dynamic Discharge Coefficient For Bleed Valve 22	–
C_{d32}	Dynamic Discharge Coefficient For Bleed Valve 32	–
C_{d42}	Dynamic Discharge Coefficient For Bleed Valve 42	–
A_{11}	Area of Bleed Valve 11	in^2
A_{31}	Area of Bleed Valve 31	in^2
A_{12}	Area of Check Valve 13	in^2
A_{22}	Area of Check Valve 22	in^2
A_{32}	Area of Check Valve 32	in^2
A_{42}	Area of Check Valve 42	in^2
D_{v12}	Diameter of Hole Pattern of Check Valve 13	in
D_{v22}	Diameter of Hole Pattern of Check Valve 22	in
D_{v32}	Diameter of Hole Pattern of Check Valve 32	in
D_{v42}	Diameter of Hole Pattern of Check Valve 42	in
ρ	Density of Hydraulic Oil	slug·ft/in^4
$F_{1\Delta p}$	Force On Shim Stack 1 Due to Pressure Drop Across Valve 12	lbf
$F_{2\Delta p}$	Force On Shim Stack 2 Due to Pressure Drop Across Valve 22	lbf
$F_{3\Delta p}$	Force On Shim Stack 3 Due to Pressure Drop Across Valve 32	lbf
$F_{4\Delta p}$	Force On Shim Stack 4 Due to Pressure Drop Across Valve 42	lbf
$F_{1inertia}$	Force On Shim Stack 1 Due to Change in Fluid Inertia	lbf
$F_{2inertia}$	Force On Shim Stack 2 Due to Change in Fluid Inertia	lbf
$F_{3inertia}$	Force On Shim Stack 3 Due to Change in Fluid Inertia	lbf
$F_{4inertia}$	Force On Shim Stack 4 Due to Change in Fluid Inertia	lbf

Symbol	Description	Unit
V_{32o}	Initial Volume of Gas in Chamber 3	in^3
V_3	Total Volume of Chamber 3	in^3
p_{3o}	Initial Pressure in Chamber 3	psi

Chapter 1: INTRODUCTION

1.1 Motivation

The automotive industry has become one of the most competitive industries of today's economy. Efficient use of time and resources is crucial in such an industry. A tool that has significantly improved the efficiency of automotive design and development is physical modeling of the automobile. Theoretical physical models help engineers to better understand exactly how automotive systems work. Insight to how these systems work ultimately leads to the ability to improve upon them. Automotive companies have invested massive amounts of resources into research that aims to model the dynamics of an automobile using physical mathematical equations. To do this the automobile is broken down into numerous systems. Each of these systems can be characterized using several equations. Many of these systems can be characterized quite accurately using physically intuitive equations.

The damper is one of the more difficult systems to model. There is an overt need in the automotive industry for an accurate physical damper model which can be used in larger vehicle system models and as an individual tool for damper design. Unfortunately, few detailed analytical damper models exist in scholarly literature. A major reason for this is that the damper is characterized by phenomena that are difficult to predict theoretically without empirical knowledge of certain parameters such

as friction coefficients, discharge coefficients, and effective stiffness values of various parts. In the absence of a true physical damper model engineers have developed other methods of damper design. Many of these methods involve trial and error. Trial and error methods have been replaced in most other areas of automotive design due their inherent inefficient use of time as well as their lack of precision. It is possible that this method prevails in damper design because it is highly compatible with the subjective methods used to evaluate passenger comfort. In spite of this advantage of the trial and error method, a better understanding of the physical processes that take place in the damper would be extremely beneficial to the damper design process.

1.2   Project Objectives

The objective of this study is to create a analytical damper model. This model will calculate the force output from the damper based on a dynamic input displacement. The parameters of this model will be based on a specific damper and will be evaluated using theoretical and experimental methods. The stiffness of the damper piston check valves is to be evaluated using two different experimental methods. One method involves a purely mechanical test while the other involves application of fluid pressure to the shims. The final model will be validated with at least 80% accuracy.

1.3   Background

The damper is an important part of the automotive suspension. This is the device that dissipates unwanted vertical and lateral energy from the automobile. If the suspension consisted only of a spring with no energy dissipation, any input to the system would result in perpetual harmonic motion. Energy would convert between

kinetic energy and potential energy but would never leave the system. The damper converts kinetic energy to thermal energy thus effectively dissipating it from the system.

The dampers used in this study are dual tube dampers. As can be seen in Figure 1.1, these dampers consist of three chambers. These are the rebound, compression, and reserve chambers. For the purpose of this paper these three chambers will be denoted as chamber 1, chamber 2, and chamber 3 respectively. Chambers 1 and 2 consist entirely of hydraulic oil and are separated by a piston attached to the damper rod. Most of the damping is generated by flow of oil between chambers 1 and 2 through orifices in this piston. Chamber 3 makes up the space between the inner and outer tubes. This chamber consists of nitrogen gas and hydraulic oil which are separated by gravity. The purpose of chamber 3 is to allow the rod to be inserted into chamber 1 without creating a large increase in pressure. When the rod is inserted, the nitrogen in chamber 3 compresses to account for the change in volume caused by the insertion of the rod. Due to the low bulk modulus of nitrogen gas, the rod can be inserted without significantly increasing the internal pressure of the damper.

The characteristics of the piston orifices play a large role in the dynamics of the damper. They control the flow of hydraulic oil from chamber 1 to 2. There are two types of orifices in the damper piston. One of these orifices is a constant area bleed valve. This orifice is open regardless of pressure and allows flow in both directions. The piston also contains two variable area check valves. The check valves are different from the bleed valve in several ways. Unlike the bleed valve, the check valves close at low pressure differentials. Also, each check valve will only allow flow in one direction. Lastly, the cross sectional area of each check valve changes depending

3
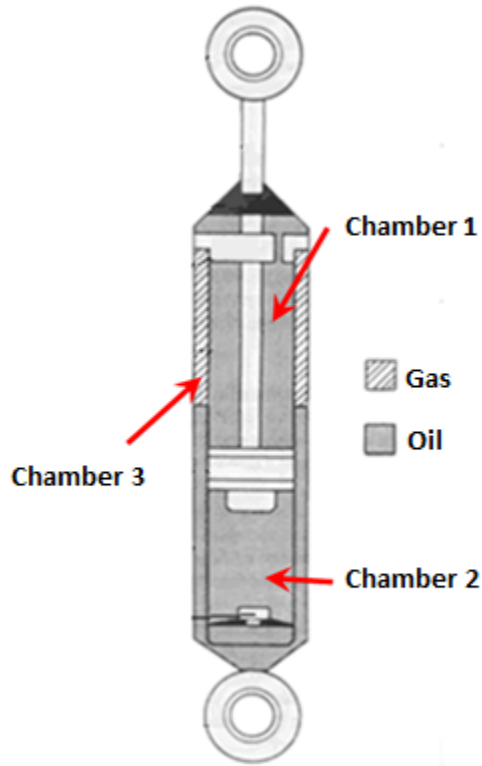
Figure 1.1: Diagram of Dual Tube Damper [4]

upon the pressure difference across the valve. These check valves are made up of orifices sealed at one opening by circular cantilevered shims. These can be seen in Figure 1.2. As the difference in pressure across the valve increases, more force is applied to the shim. This force causes the shim to deflect allowing flow through the orifice. The orifice area is directly related to the deflection of the shim and therefore the pressure differential.

The geometry of the piston valves can vary between different types of dampers. Since the valves have a large effect on the dynamics of the damper it is important to

4
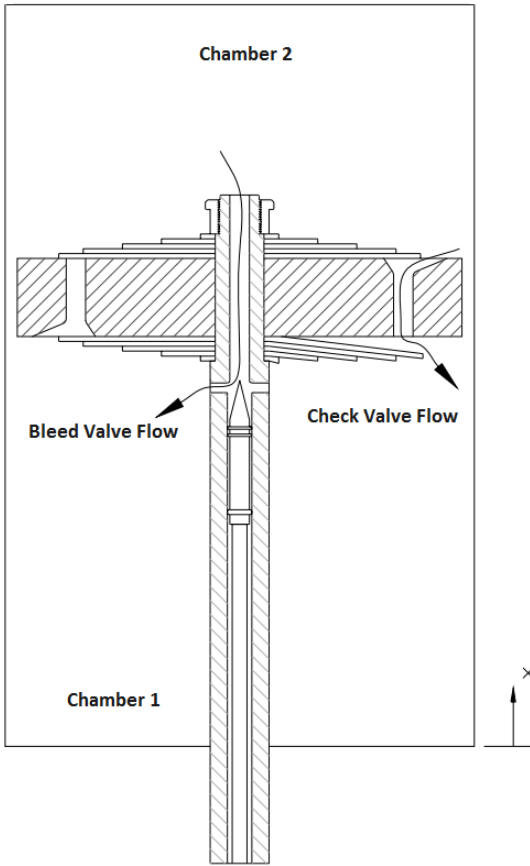
Figure 1.2: Diagram of Damper Piston Valves [10]

note the geometry of the specific damper that is to be modeled. The most unique part of the damper that is being studied is the bleed valve. Instead of having a seperate orifice as a bleed valve as shown in Figure 1.2, this piston head has slots in the piston face to allow fluid flow even when the shims have not deflected. These slots are shown in Figure 1.3.

Figure 1.3: Photograph of Slots in Piston Face

Chapter 2: LITERATURE REVIEW

There were several goals in mind during the conduction of the literature review. One goal was to identify the damper parameters that are relevant for creating an accurate parametric model. The second goal of the literature review was to investigate the various methods that have been used in the past for measuring these parameters. Each of the relevant parameters that were identified in the literature research is discussed in this section.

2.1 Valve Characterization

Many researchers including Lang [4] and Talbott [10] have modeled the characteristics of damper valves using equations for orifice flow. The areas of these orifices were modeled as functions of shim displacement. Talbott also developed analytical equations for shim stiffness using formulas from Roark [12]. One drawback of this method was that the effective location at which the fluid pressure is acting on the shim is unknown. Talbott chose a value that best fit his experimental data. In 2007 Shams [9] published an article researching a much more sophisticated method of characterizing damper valves. Shams used FEA and CFD to model the characteristics of damper valves. Shams created a 3D CFD model of the valve. Shams conducted simulations for seven different shim deflections. For each shim deflection the simulation

was conducted for six different piston velocities. This simulation provided a relationship between resultant shim force and shim deflection for various piston velocities. Shams then conducted an FEA simulation to determine the relationship between resultant shim force and elastic shim deflection. These two relationships were coupled to determine the relationship between piston velocity and shim deflection.

In 2008 Tom Walters conducted an experiment in which he measured the displacement of a reed deforming under fluid pressure [11]. He was able to do this using a laser displacement transducer. His research showed that it is feasible to measure the dynamics of an object submerged in hydraulic fluid. A method similar to his could be used to measure the dynamics of the valve while fluid is flowing through it.

2.2 Fluid Compressibility

In 2004 Lee and Sun [5] developed equations for the effective bulk modulus of the fluid in a damper. This effective bulk modulus accounts for the compliance of all the internal components of the damper. This includes the fluid, gas, and chamber. Lee and Sun determined the bulk modulus of the fluid experimentally. The gas was modeled using the ideal gas equations. Lee and Suns most significant contribution was their analytical methods of determining the effective bulk modulus of the chambers of the damper. Using these methods they showed that the compliance of the damper chamber is significant in comparison to the bulk modulus of the fluid.

There are many methods that have been used in the past for measuring the bulk modulus of a fluid. Many of these methods involve measuring the speed of sound through the fluid. The speed of sound is related to the bulk modulus and the density

and the density of the fluid by

$$\beta = \rho c^2.$$

If the density and the speed of sound are both known, the bulk modulus can be determined. Balasubramanian [1] presents a method of measuring the speed of sound through a fluid. Balasubramanian used a plunger to apply pressure pulses to the fluid in a rigid container. Three pressure transducers were installed at various distances from the plunger. The time lag between the signals measured by each of these pressure transducers could be used to determine the speed of sound through the fluid.

2.3   Dynamic Discharge Coefficient

In Langs thesis [4] he experimentally determined dynamic discharge values for all the valves in a specific damper. He correlated these dynamic discharge values with acceleration number as well as Reynolds Number. The results of his research showed that the dynamic discharge coefficients for each of the valves were very close to 0.7. Many subsequent studies including Rhoads [8] and Talbott [10] have used 0.7 as a starting point and later adjusted the dynamic discharge coefficient such that a better correlation could be achieved between the model and the data.

2.4   Coulomb Friction

According to Duym [3], large friction effects occur within the damper when it is subjected to side loading. However, in the absence of side loading the Coulomb friction force can be assumed to have a constant magnitude. The direction of this friction will always oppose velocity. Duym states that friction forces are typically between 0 to 100 N. Talbott [10] presents a method of measuring this friction force. In order

to measure the coulomb friction force the viscous friction force must be minimized. This was done by cycling the damper at extremely low velocities. To further reduce viscous effects the valve shims were removed allowing unrestricted flow through the damper. Talbotts results are shown Figure 3.
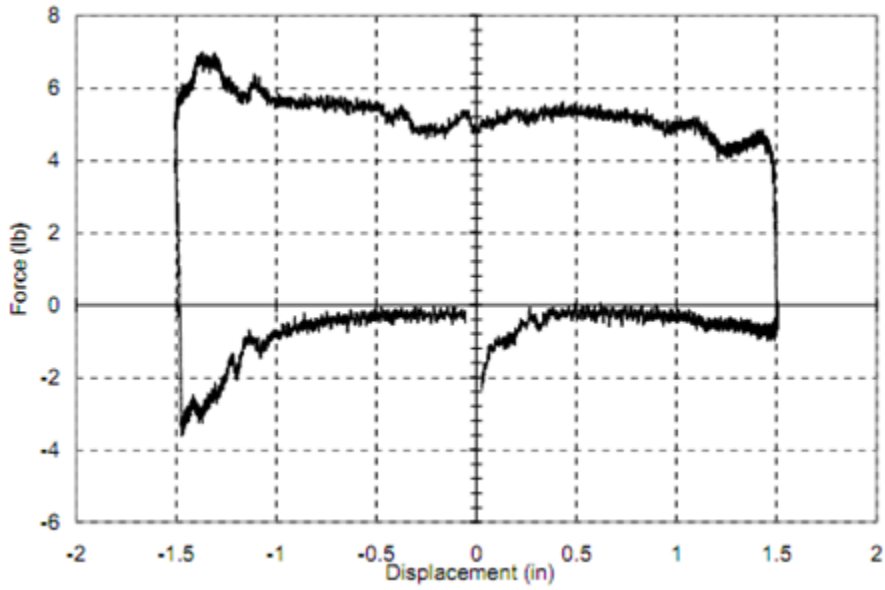
Figure 2.1: Coulomb Friction Results [10]

Chapter 3: ANALYTICAL MODEL

Figure A.1 shows the diagram that was used to derive the analytical damper equations. It should be noted that this diagram is not geometrically accurate. The actual geometry of the damper can be seen in Figure 1.1. The governing equations for this model are based on four considerations. These are Newtons second law, fluid continuity, orifice flow, fluid inertia, and fluid compressibility.
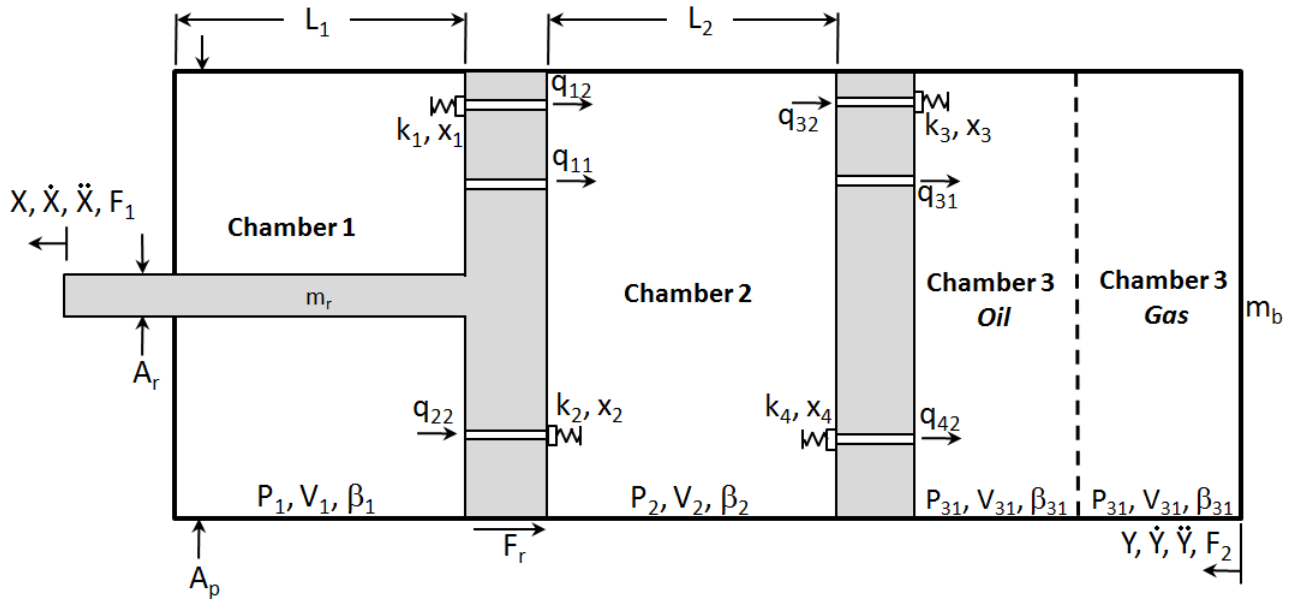
Figure 3.1: Diagram of Analytical Damper Model

3.1 Force Balance Equations

Unlike other damper models, this model has two degrees of freedom. The model takes into consideration the movement of the damper as well as the movement of the piston instead of considering only the movement of the piston. This has two advantages over assuming that the damper body is fixed and the piston is moving. One is that it is consistent with the experimental testing in which the piston and rod are fixed while motion is excited in the damper body. Another reason is that during actual use the damper body and the piston are both moving independently. This could not be modeled using only one degree of freedom. In order to account for both piston and body movement a separate force balance equation was developed for the piston and for the body. The difference between the external forces acting upon the damper body and piston rod will be due solely to the difference in inertia between the damper body and the piston. These two force balances are defined as

$$F_1 = m_r \ddot{X} - p_2 A_p + p_1 (A_p - A_r) + F_r sgn(\dot{Z}) \tag{3.1}$$

and

$$F_2 = m_b \ddot{Y} - p_2 A_p + p_1 (A_p - A_r) + F_r sgn(\dot{Z}). \tag{3.2}$$

The model is sensitive to the the variables X and Y but is also sensitive to a variable Z given as

$$Z = X - Y. \tag{3.3}$$

3.2   Chamber 1 Continuity Equation

This equation simply states that the sum of flows in or out of the chamber in addition to the change in volume due to fluid compressibility is equal to the total change in volume of the chamber. The chamber 1 continuity equation is

$$q_{11} + q_{12} + q_{22} + q_{\beta 1} = \ddot{Z}(A_p - A_r).\tag{3.4}$$

Each of the flow variables in Equation (3.4) is defined in the following sections.

3.3   Chamber 1 Orifice Flow Equations

The piston separating chamber 1 from chamber 2 contains a bleed valve and a check valve. The bleed valve flow can be modeled using the laminar orifice flow equation and is given as

$$q_{11} = n_{11} C_{d11} A_{A11} sgn(p_1 - p_2)\sqrt{\frac{2|p_1 - p_2|}{\rho}}.\tag{3.5}$$

The design of the check valves allows flow in only one direction. A piecewise function is used to model this. The piecewise function sets the flow to zero instead of allowing flow in the reverse direction. The flow through valve 12 can be modeled as

$$q_{12} = \begin{cases} 0 & p_1 \geq p_2 \\ -C_{d12} A_{12}\sqrt{\frac{2|p_1 - p_2|}{\rho}} & p_1 < p_2 \end{cases}.\tag{3.6}$$

Similarly, the flow through valve 22 can be modeled as

$$q_{22} = \begin{cases} 0 & p_1 \leq p_2 \\ C_{d22} A_{22}\sqrt{\frac{2|p_1 - p_2|}{\rho}} & p_1 > p_2 \end{cases}.\tag{3.7}$$

3.4   Chamber 1 Fluid Compressibility Equations

The volume change of the fluid due to fluid compressibility is derived from the equation for fluid bulk modulus. The bulk modulus is a function of pressure that is determined experimentally. The change of volume due to fluid compressibility is defined as

$$q_{\beta 1} = \frac{(L_1 - Z)(A_p - A_r)}{\beta_1}\dot{p}_1 \qquad (3.8)$$

where

$$\beta_1 = \beta_1(p_1).$$

3.5   Chamber 1 Orifice Area Equations

The areas of the smallest orifices through which the fluid flows are given by

$$A_{12} = \pi D_{v12} x_1 \qquad (3.9)$$

and

$$A_{22} = \pi D_{v22} x_2 \qquad (3.10)$$

where D_{v22} and D_{v12} are the diameters of the orifice patterns and x_1 and x_2 are the shim displacements defined in the following section.

3.6   Chamber 1 Shim Displacement

The displacement of the shims is related to the force and the stiffness of the shim stack. The force on the shim is the sum of the force due to differential pressure and the force due to change in fluid inertia. The forces due to differential pressure and

change in fluid inertia respectively are defined as

$$F_{1\Delta p} = |p_1 - p_2| A_{f12} n_{12} \tag{3.11}$$

and

$$F_{1inertia} = \rho \frac{q_{12}^2}{A_{f12} n_{12}} \tag{3.12}$$

for valve 12. For valve 22 the forces due to differential pressure and change in fluid inertia are

$$F_{2\Delta p} = |p_1 - p_2| A_{f22} n_{22} \tag{3.13}$$

and

$$F_{2inertia} = \rho \frac{q_{22}^2}{A_{f22} n_{22}} \tag{3.14}$$

respectively. The relationship between shim displacement and total resultant force on the shims for valve 12 is defined as

$$x_1 = \frac{F_{1\Delta p} + F_{1inertia}}{k_1} \tag{3.15}$$

and

$$x_2 = \frac{F_{2\Delta p} + F_{2inertia}}{k_2} \tag{3.16}$$

$$x = \frac{F_p + F_i}{k} \tag{3.17}$$

for valve 22 where k_1 and k_2 are the effective shim stiffness values.

The equations for chamber 2 are very similar to the chamber 1 equations and are given in Appendix A.

3.7   Chamber 3 Continuity Equation

The chamber 3 continuity equation is similar to the chamber 1 continuity equation (3.4) and is given as

$$q_{31} + q_{32} + q_{42} - q_{\beta 31} - q_{\beta 32} = 0. \tag{3.18}$$

The individual flow variables used in Equation 3.18 are defined in the following section.

3.8   Chamber 3 Fluid Comporessibility Equations

Chamber three is unique to the other chambers in that its volume is fixed. However, the individual volumes of gas and oil within chamber three are not fixed. These two volumes can be related by

$$V_{31} + V_{32} = V_3 \tag{3.19}$$

where V_{31} is the volume occupied by the fluid in chamber 3 and V_{32} is the volume occupied by the gas in chamber 3. The individual flows used in Equation 3.18 can then by defined as

$$q_{\beta 31} = \frac{V_{31}}{\beta_{31}} \dot{p}_3 \tag{3.20}$$

and

$$q_{\beta 32} = \frac{V_{32}}{\beta_{32}} \dot{p}_3 \tag{3.21}$$

where

$$\beta_{31} = \beta_{31}(p_3) \tag{3.22}$$

and

$$\beta_{32} = \beta_{32}(p_3). \tag{3.23}$$

16

The volume of the gas within chamber 3 can then be related to the pressure of chamber 3 by

$$V_{32} = V_{32_0}(1 - \frac{p_3 - p_{30}}{\beta_{32}})$$
(3.24)

where V_{32_o} is the initial volume of gas in chamber 3.

Chapter 4: BULK MODULUS

4.1 Gas Bulk Modulus

4.1.1 Background and Theory

The bulk modulus of a fluid is defined as

$$\beta = -V\frac{\delta P}{\delta V}.$$ (4.1)

During adiabatic compression the bulk modulus of an ideal gas is related to the gas pressure by

$$\beta = -kp_o$$ (4.2)

where k is the adiabatic index of the gas. During isothermal compression the bulk modulus of an ideal gas is is related to the gas pressure by

$$\beta = -p_o$$ (4.3)

In this study the gas is primarily nitrogen. For this reason an adiabatic index of 1.4 is used.

4.1.2 Procedure

The bulk modulus testing was done by compressing the experimental fluid and measuring the fluid pressure at different volumes. For the gas this was able to be done in the damper allowing for an effective bulk modulus to be obtained. This effective bulk modulus includes the bulk modulus of the gas as well as the stiffness of the damper chamber.

Prior to testing, the piston valve shims and reserve valve shims were removed. This setup allowed the initial fluid volume to be the combined volume of chambers 1, 2, and 3. This resulted in a total initial volume of 42.66 in^3. The change in volume was only due to the insertion of the piston rod. When the piston rod is compressed there is a transient increase in pressure that is due to viscous flow through the piston orifices. In order to measure only the increase in pressure due to the compression of the fluid, a static compression was applied until the pressure reached a steady state value. This steady state value was used for the bulk modulus calculations. Once δd and δP were known, Equation (4.1) could be used to calculate the bulk modulus given

$$\delta V = A\, \delta d. \tag{4.4}$$

A diagram of the setup is shown in Figure 4.1.

The test was performed using a damper dynamometer. This machine was able to apply a known displacement and measure the reaction force of the damper. In order to measure pressure and temperature within the damper, custom chamber accessible dampers were built by Showa R&D. These dampers have a pressure sensor installed in each of the three chambers. The dampers also have a thermocouple installed in chamber 3. The damper used for gas bulk modulus testing is shown in Figure 4.2.

19
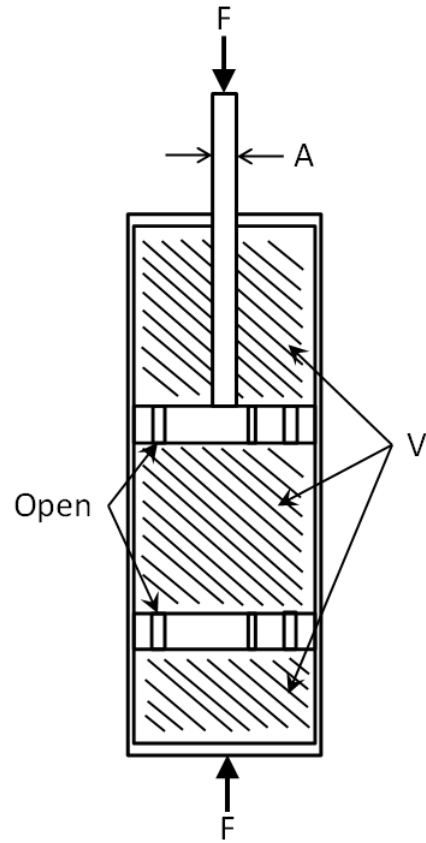
Figure 4.1: Bulk Modulus Test Setup
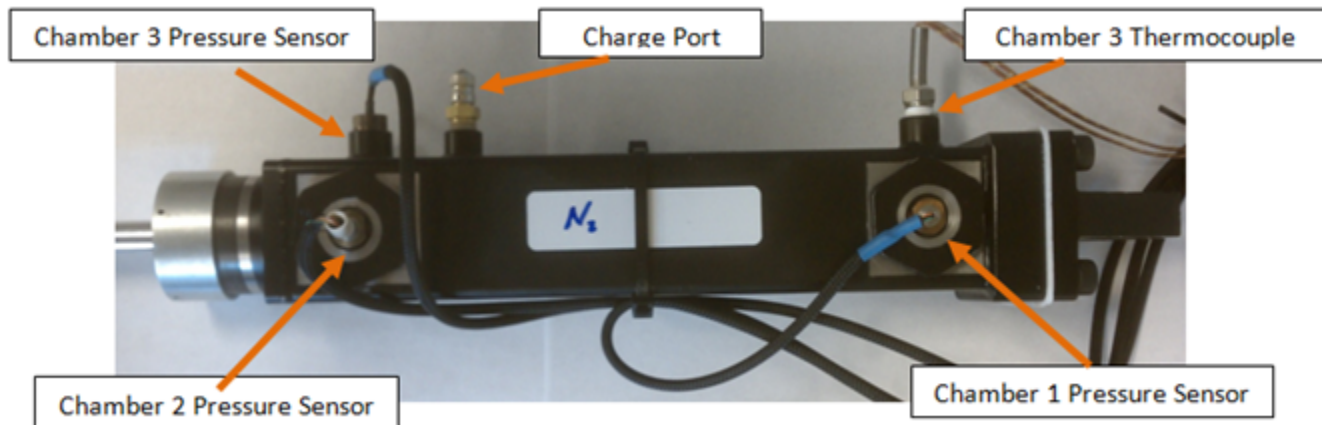
Figure 4.2: Chamber Accessible Damper

Twelve tests were conducted to obtain the gas pressure at thirteen volumes including the initial volume. During each test the displacement of the rod started at zero. The rod displacement was then ramped to the desired value where it was held for thirty seconds before returning to zero. The desired displacement started at 10 mm and was increased by 10 mm each test until it reached 120 mm.

4.1.3   Results

Figure 4.3 shows the chamber volume and steady state pressure for each rod displacement. To obtain the bulk modulus of the fluid the pressure can be plotted against the volumetric strain as shown in Figure 4.4. Volumetric strain is defined as

$$\varepsilon_v = \frac{\delta V}{V_o}. \tag{4.5}$$

The bulk modulus is equal to the negative slope of the pressure versus volumetric strain plot represented by

$$\beta = -\frac{\delta P}{\varepsilon_v} \tag{4.6}$$

The resulting effective bulk modulus at 22° C and 140.5 psi is shown and compared to the theoretical value in Table 4.1.

Method	Value (psi)	Percent Difference (%)
Experimental Bulk Modulus	149.3	-
Theoretical Isothermal Bulk Modulus	196.7	+31.7
Theoretical Adiabatic Bulk Modulus	140.5	-5.89

Table 4.1: Bulk Modulus of Nitrogen Gas at 140.5 psi and 22° C
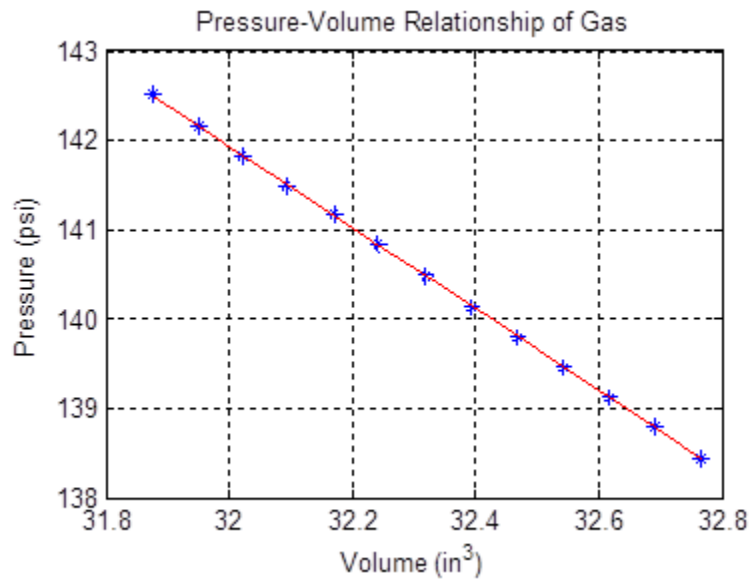
Figure 4.3: Pressure Volume Relationship of Gas
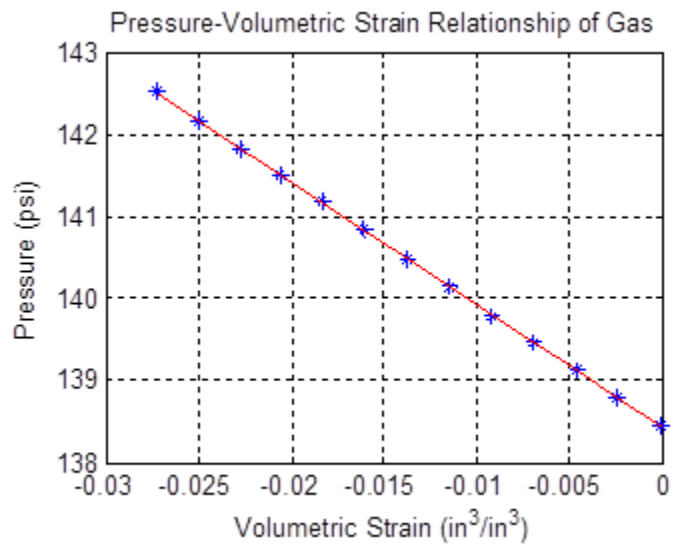
Figure 4.4: Pressure Volumetric Strain Relationship of Gas

4.2   Oil Bulk Modulus

Obtaining the bulk modulus of the fluid was more challenging than it was for the gas due to the time dependency of the fluid bulk modulus. This time dependency is most likely due to changes in the way the gas molecules are contained within the fluid over time. It was observed that, if the fluid was allowed to settle following emulsification, the bulk modulus of the fluid would steadily decrease. The bulk modulus would decrease at a faster rate when the fluid was at higher pressures. This time dependency is not a process that needs to be included in the model because the fluid has no time to settle during normal use. The time dependency of the fluid bulk modulus was only considered because it influenced the measurement of the fluid bulk modulus.

4.2.1   Preliminary Testing

Initially the time dependence of the fluid bulk modulus was not considered. An attempt was made to determine the fluid bulk modulus using the same method used to obtain the gas bulk modulus. This attempt failed because the fluid pressure did not reach steady state following a step volume reduction.

4.2.2   Final Test Procedure

The procedure used to obtain the bulk modulus of the gas was not able to be applied to the fluid due to the time dependency of the fluid bulk modulus. Instead, a quasi-static bulk modulus test was developed. This test used the same equipment as the gas bulk modulus test. The damper was filled completely with oil meaning that the working volume (V) was equal to the sum of the volumes of the three chambers of the damper as shown in Figure 4.1. The volume of the fluid was decreased at
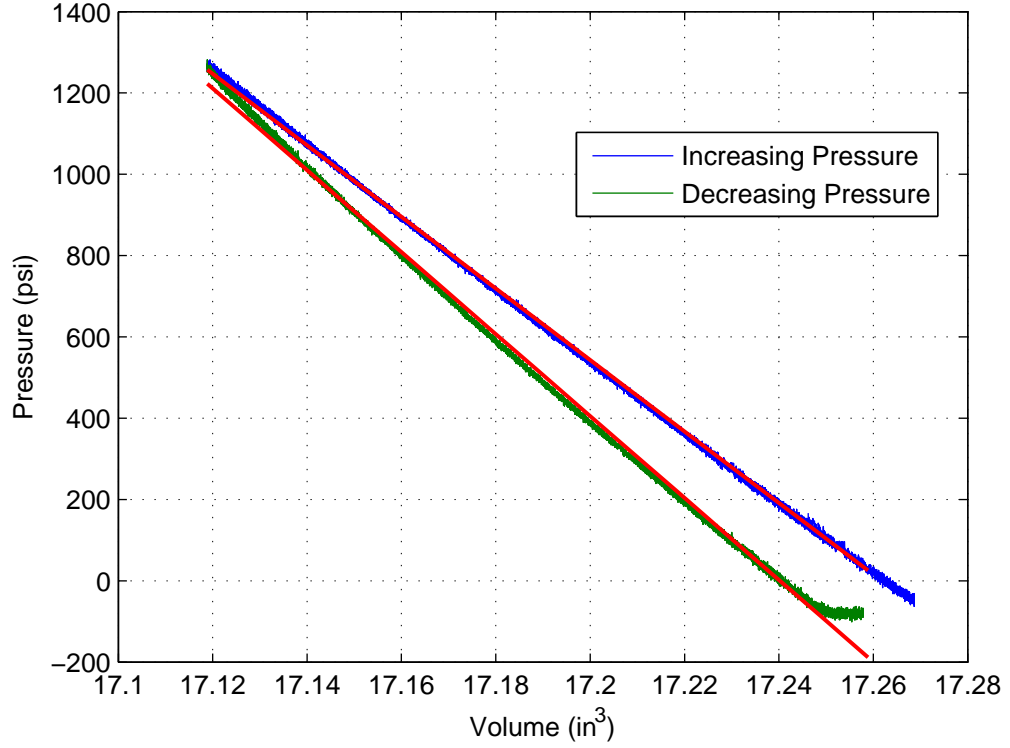
Figure 4.5: Pressure-Volume Relationshiop during Quasi-Static Fluid Bulk Modulus

a constant rate as the pressure in the chambers was measured. The relationship between pressure and volume obtained from this test was used to calculate the bulk modulus of the fluid.

4.2.3 Results

Figure 4.5 shows the relationship between pressure and volume during the quasi-static test for increasing and decreasing pressure. The hysteresis is caused by the reduction in bulk modulus over time. If the effects of time dependency were excluded the pressure volume curve would lie between the two curves shown in Figure 4.5.

Bulk Modulus for Increasing Pressure (psi)	Bulk Modulus for Decreasing Pressure (psi)	Mean Bulk Modulus (psi)
1.519×10^5	1.740×10^5	1.630×10^5

Table 4.2: Mean Bulk Modulus for Increasing and Decreasing Pressure

The bulk modulus was calculated for increasing and decreasing pressure. These values as well as the mean value are shown in Table 4.2.

Chapter 5: COULOMB FRICTION

The damping force from the damper is is made up mainly of forces created by flow through the damper piston. However, Coulomb forces also contribute to this damping force. Coulomb friction is the friction that is caused by contact between two surfaces. In this case the Coulomb friction is due to contact between the piston and cylinder and contact between the rod and seal. Unlike viscous friction, Coulomb friction is not dependent on speed. The Coulomb friction was assumed to have a constant magnitude with a direction that opposed the velocity. This magnitude was measured experimentally. This process is discussed in this chapter.

5.1 Procedure

In order to measure Coulomb friction in the damper, viscous friction must be minimized. Several modifications were made to the damper to minimize viscous friction. The shims were removed to allow unrestricted flow through the piston. Also, chambers one and three were opened to prevent build up of pressure in these chambers. This setup is shown in Figure 5.1.

The damper was cycled at several speeds ranging from 0.5 mm/s to 1000 mm/s. A triangle wave was used as the displacement input. This was done to minimize forces due to inertia.
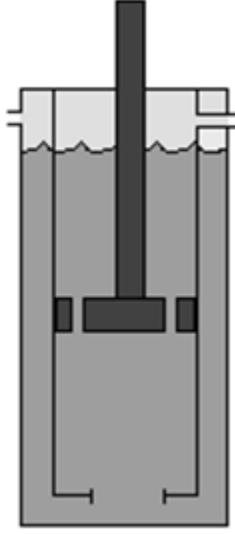
Figure 5.1: Experimental Setup for Coulomb Friction Testing

5.2   Results

The forces exerted on the damper piston at constant velocity are shown in Figure 5.2 for various piston speeds. Just as Talbott described [10], the force is larger during compression. This does not necessarily indicate that the Coulomb friction force is larger during compression. It is possible that other forces are contributing to this measurement.

If the magnitude of the Coulomb friction force is assumed to be independent of direction the force can be calculated as

$$F_c = \frac{F_{Compression} - F_{Rebound}}{2} \tag{5.1}$$

The resulting friction force is shown in Figure 5.3.
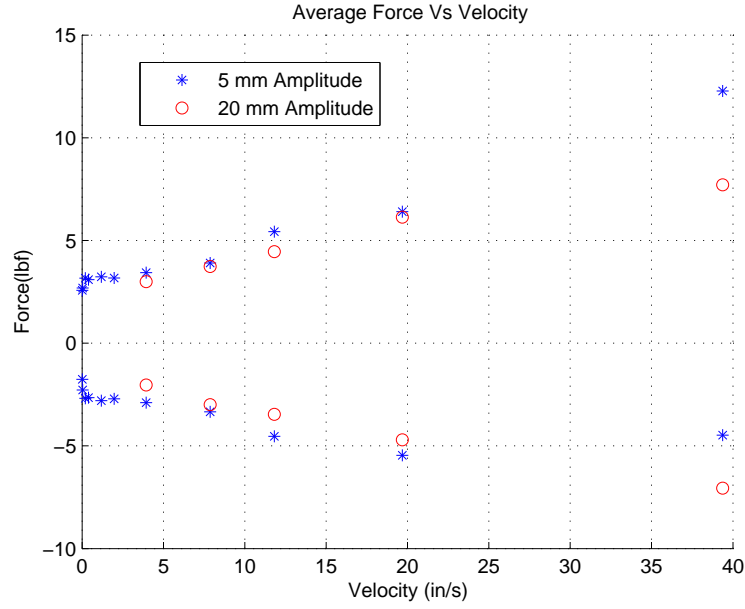
Figure 5.2: Damper Force at Constant Velocity

It is assumed that the Coulomb friction force is not dependent on velocity. The velocity dependence seen in Figure 5.3 is most likely due to viscous damping. To exclude the effect of viscous damping from the Coulomb friction measurement the data was examined at low velocities. A Coulomb friction force value of 2.6 lbf was used as an initial estimate. This value was then multiplied by 1.05 to create a more accurate model. This is discussed in Chapter 10.
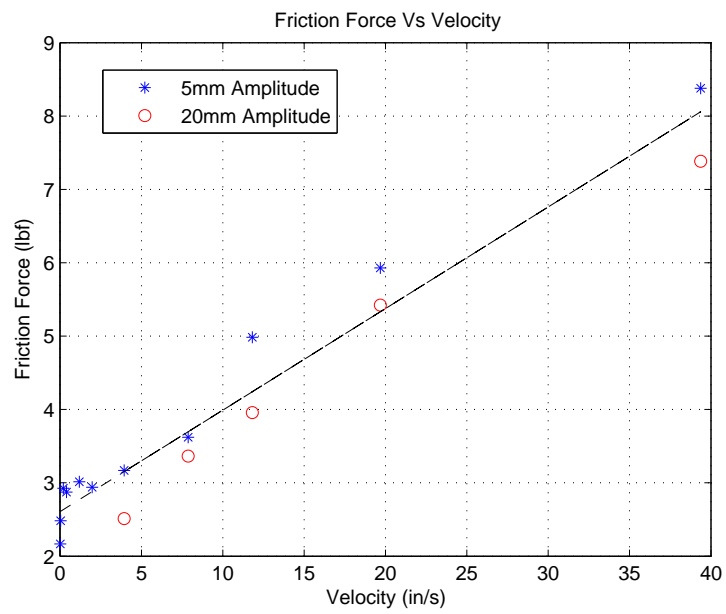
Figure 5.3: Coulomb Friction Force for Various Pistion Velocities

Chapter 6: EFFECTIVE MASS OF DAMPER BODY

The balance of forces shown in Equation (3.2) included a term m_b representing the mass of the damper body. The force due to the acceleration of the damper body is calculated as the product of this mass and the acceleration of the damper body. In reality this calculation is not accurate because the damper body is not actually a rigid body. The acceleration of the casing of the damper body is not necessarily equal to the acceleration of the entire mass of the damper body because the damper fluid can accelerate relative to the damper body. A model that distinguishes the force due to the acceleration of the damper body from the force due to the acceleration of the fluid would be complex and would only yield a small improvement to the accuracy of the damper model. Instead, an effective mass of the damper was found.

The model uses this effective mass as the ratio between force and acceleration of the entire damper body. It is important to note that the force due to acceleration of the damper body is transmitted entirely through the bottom of the damper. In terms of the model, this means that the effective mass of the damper body will affect the calculation of F_2 but will have no effect on F_1. This means that that the effective mass found in this section will be irrelevant to the accuracy of the model since only F_1 is used to validate the model with experimental data. However, the effective mass may be relevant during application of this model if F_2 is to be calculated.
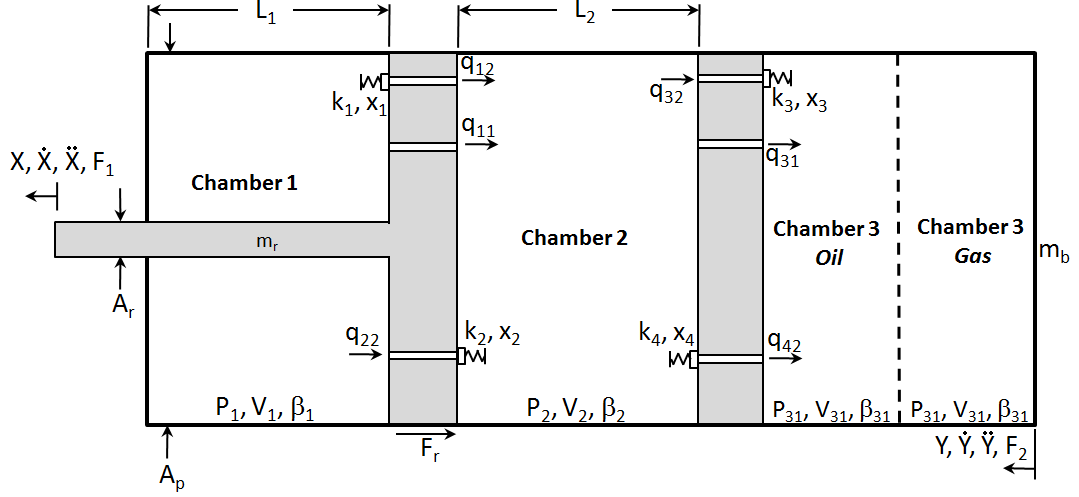
Figure 6.1: Diagram of Analytical Damper Model

6.1 Theory

The effective mass can be derived from Equations (3.1) and (3.2). During the experimental testing the piston rod will be fixed and therefore

$$\ddot{X} = 0.$$

Substituting this into (3.1) and (3.2 gives

$$-F_1 = p_2 A_p - p_1(A_p - A_r) - F_r sgn(\dot{Z}). \tag{6.1}$$

and

$$F_2 = m_{b_{eff}} \ddot{Y} - F_1. \tag{6.2}$$

Rearranging Equation (6.2) gives

$$m_{b_{eff}} = \frac{F_1 + F_2}{\ddot{Y}}. \tag{6.3}$$

6.2 Procedure

The effective mass of the damper can be determined using standard damper testing procedures. However, there were two modifications that were made to the standard damper testing setup. One modification was that an accelerometer was attached to the damper to measure the vertical acceleration of the damper. The second and most important modification was an additional load cell that was placed below the damper. This allowed for the external force to be measured at the top of the damper rod and at the bottom of the damper body. These are forces F1 and F2 respectively from Figure 6.1.

The damper was cycled at several peak speeds between 50 mm/s and 800 mm/s. The data from the low speed tests was not useful for this study due to low acceleration to noise ratios. For this reason the tests with peak speeds of 500 mm/s, 600 mm/s and 800 mm/s are focused on in this study.

6.3 Results

An algorithm was used to determine the value of effective mass that minimized the error between the sum of the two forces and the product of acceleration and effective mass. Two different error functions involving RMS were used. The error for various effective mass values found using the error function

$$e = RMS[\ddot{Y}m_{b_{eff}} - (F_2 + F_1]$$ \hfill (6.4)

is shown in Figure 6.2. The product of the acceleration and the resulting effective mass is compared to the difference in force in Figure 6.3 .

Figure 6.2: Error using (6.4)

Figure 6.3: Product of acceleration and effective mass compared to difference in force using effective mass found through error function shown in (6.4)
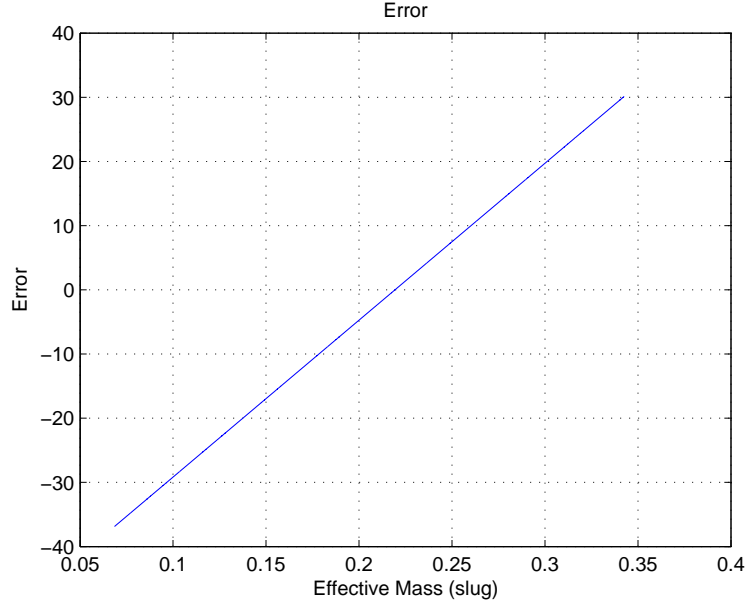
Figure 6.4: Error using (6.5)

The error for various effective mass values found using the error function

$$e = RMS[\ddot{Y}m_{b_{eff}}] - RMS[F_1 + F_2] \tag{6.5}$$

is shown in Figure 6.4. The product of the acceleration and the resulting effective mass is compared to the difference in force in Figure 6.5.

Table 6.1 shows the actual mass compared to the effective masses obtained through the two error functions. Figure 6.6 shows the actual difference in force compared to the difference in force calculated from the two effective mass values. Figure 6.7 is the same plot zoomed to show one peak. The effective mass used in the final model is 0.210 slug.
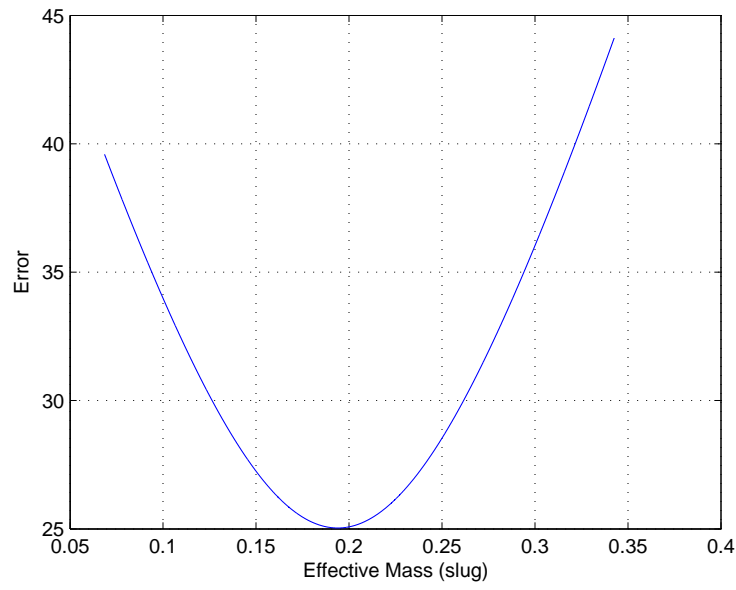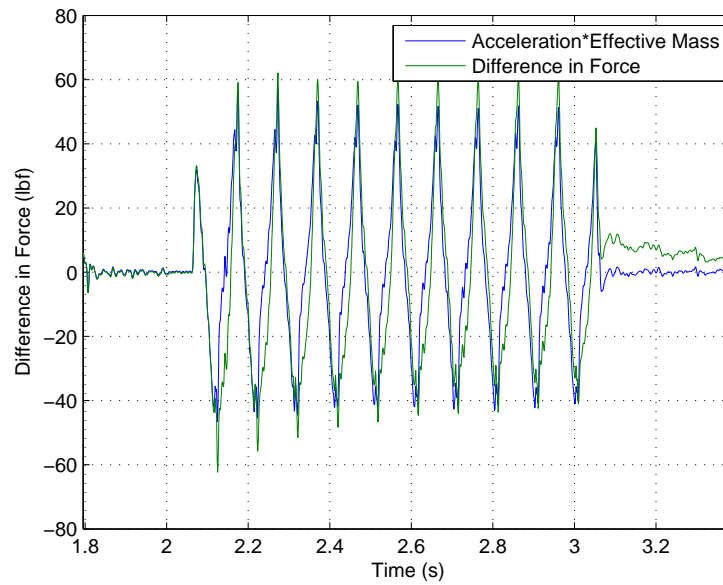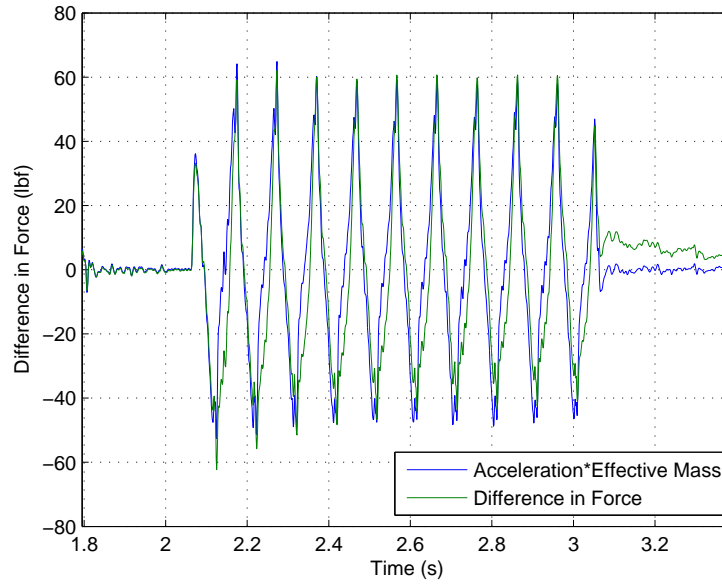
Figure 6.5: Product of Acceleration and Effective Mass Compared to Difference in Force Using Effective Mass Found Through Error Funcion Shown in (6.5)

	Mass (slug)	**% Difference** (%)
Actual	0.124	–
Effective (6.4)	0.194	56.5
Effective (6.5)	0.219	76.6

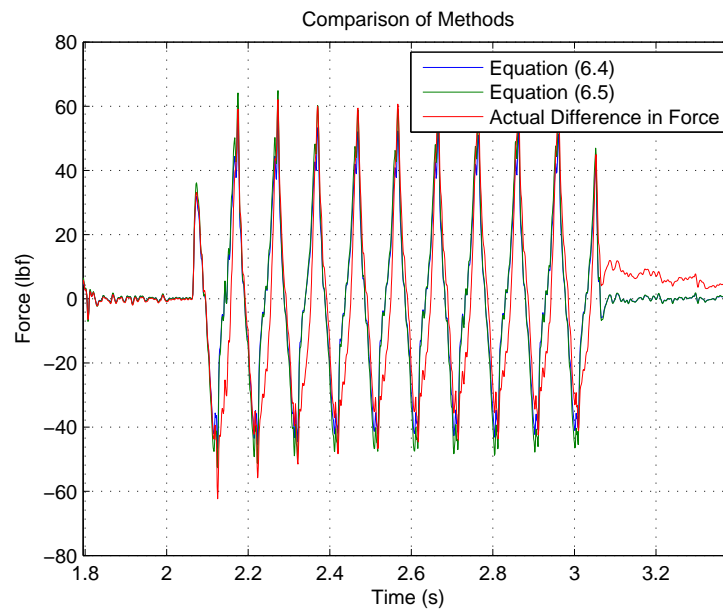Table 6.1: Comparison of Effective and Actual Damper Body Mass
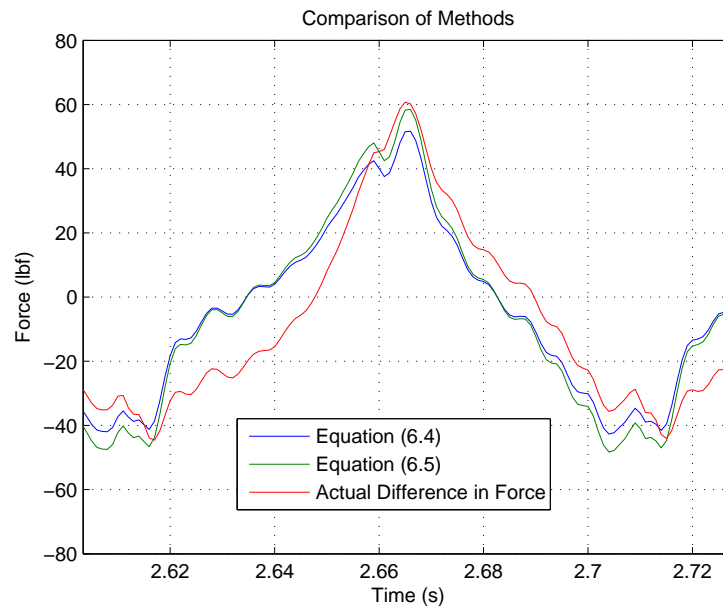
Figure 6.6: Comparrison of Methods

Figure 6.7: Comparrison of Methods (Zoomed)

36

Chapter 7: VALVE RESISTANCE - EXPERIMENTAL SHIM CHARACTERIZATION USING MECHANICAL TESTING

The most significant factor effecting valve resistance is the shim stiffness. Three methods for determining shim stiffness were considered. These three methods are analytical, experimental, and computational. Each of these methods had certain drawbacks. Analytical equations for shim stiffness have been developed using traditional stress and strain equations [12]. Unfortunately, the irregular loading that is seen by the shim is not modeled using these equations. Furthermore, these equations do not model the effects of friction between the individual shims. The friction effects were also unable to be accurately modeled using finite element analysis.

An option that was investigated was to use finite element analysis and model the shim stack as a solid body. The results of this model showed that this is not a valid approximation. Unfortunately no good computational method for determining the stiffness of the shim stack was found. However, computational fluid dynamics could be used to study other aspects of the valve such as the relationship between differential pressure and shim force and the relationship between flow and pressure.

The most viable option for characterizing the shim stiffness proved to be experimental methods. However, this method also had drawbacks. The main drawback

37

being that the loading on the shim cannot be easily recreated in an experiment. Two different experiments were conducted with the goal of determining the stiffness of the shims. The first experiment was a mechanical test that involved simplification of the loading felt by the shims. The second test was a fluid test that involved applying a fluid pressure to the shims while measuring their displacement with a laser displacement transducer. These simulations and experiments as well as their results are discussed in detail over the next three chapters.

The main difficulty when characterizing the stiffness of the shims with a mechanical test is recreating the loading of the shim. One option that was considered was to make forks with prongs that have cross sections similar to the piston orifice pattern. These prongs could be pressed against the surface of the shim to recreate the force of the fluid pressure. The drawback to this option is that parts of the prong would lose contact with the shim as the shim deflects. At any significant deflection, only the inner edge of the prong would still be in contact with the shim. This effect is shown in Figure 7.1.

To prevent this effect from taking place the loading pattern had to be simplified. Orifices with circular cross sections were simplified to point loads while orifices with rectangular cross sections were simplified to line loads. Some accuracy would be lost in this simplification. However, this simplification allowed precise control over the location of the applied load. This section describes this experiment.
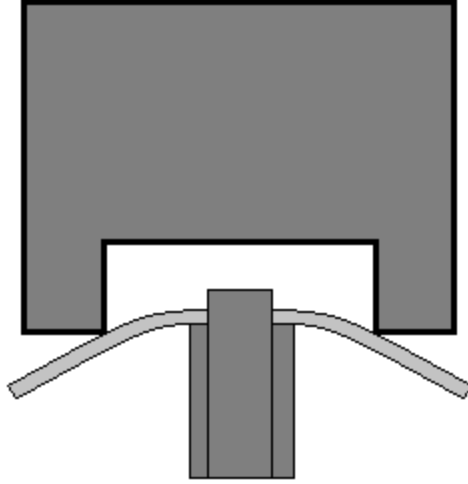
Figure 7.1: Diagram of Shims Loosing Contact with Fork Prongs

7.1 Experimental Setup

The loading forks that were used in this experiment are shown in Figure 7.2. For each valve the valve body is shown to the left and the fork designed to imitate the load is shown on the right. The entire experimental setup is shown in Figure 7.3.

The stiffness of the fixtures used in this experiment is significant. In order to obtain the stiffness of the shims alone, the fixtures and the shims can be modeled as two springs in series. This model is shown in Figure 7.4. In this model, k_{eff} is the stiffness obtained when the load is applied to the shims while k_{fix} is the stiffness obtained when the load is applied to the fixtures with the shims removed. The actual stiffness of the shims can be derived as

$$k_{shims} = \frac{k_{eff}k_{fix}}{k_{fix} - k_{eff}}.$$
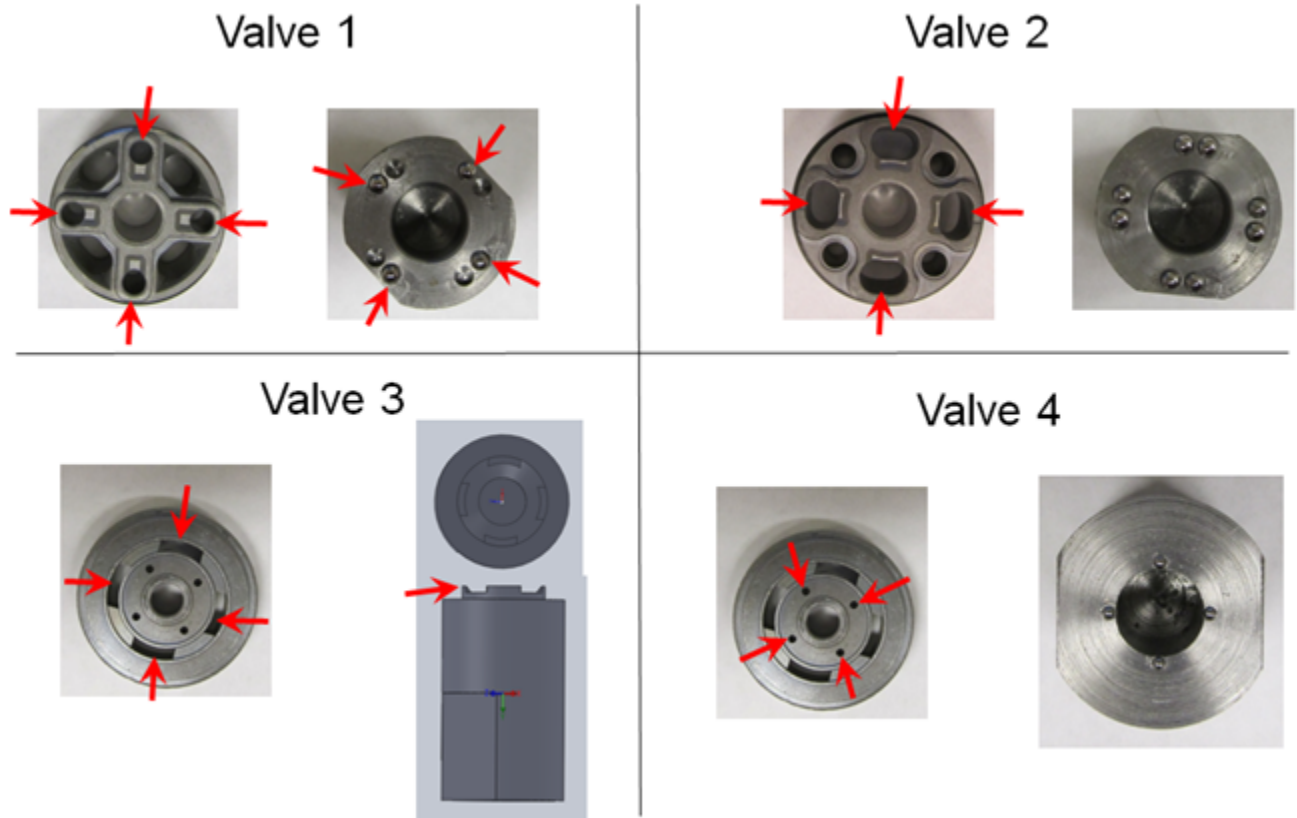
(7.1)

39

Figure 7.2: Load Forks

Preliminary shim stiffness testing showed that the stiffness curve contained three regions. These three regions are can be seen in the results shown in Figure 7.7. The first region is an extremely nonlinear region. This region is caused by slight misalignment between the shims and the loading fork. Because of this misalignment the prongs of the loading fork do not all contact the shim simultaneously. The effective stiffness changes at each instant that a prong comes into contact with the shim. For this reason region 1 is extremely nonlinear.
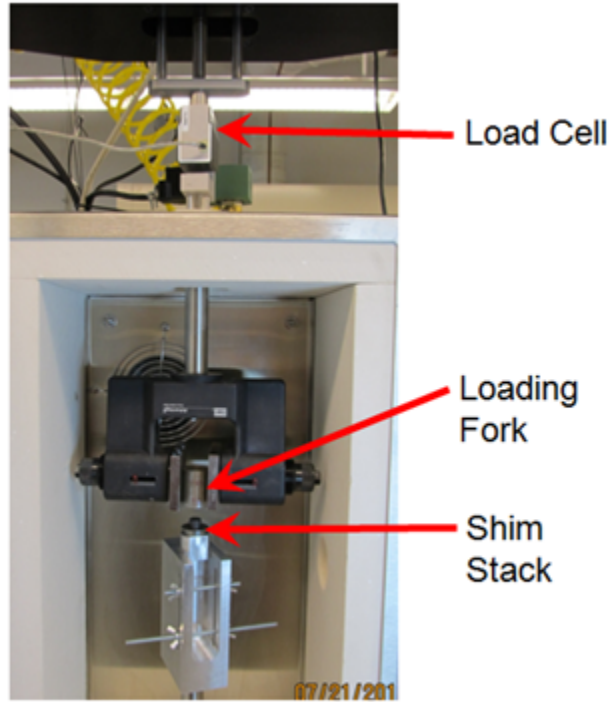
Figure 7.3: Experimental Setup for Shim Stiffness Characterization

The second region begins when the entire loading fork has made contact with the shim. This is the region desired for obtaining the shims stiffness. The third region occurs when the perimeter of the shim comes into contact with the rigid base. In region three the shims effective stiffness increases drastically. In some cases the stiffness of region three is infinite indicating that the shim has become effectively rigid. The causes of the three regions of the shim stiffness curve are illustrated in Figure 7.5.

Identifying region two of the stiffness curve was difficult in some cases. For each valve, the shim stiffness test was conducted three times for three different shim setups for the purpose of distinguishing region two from the other regions. The first test that
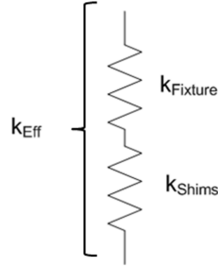
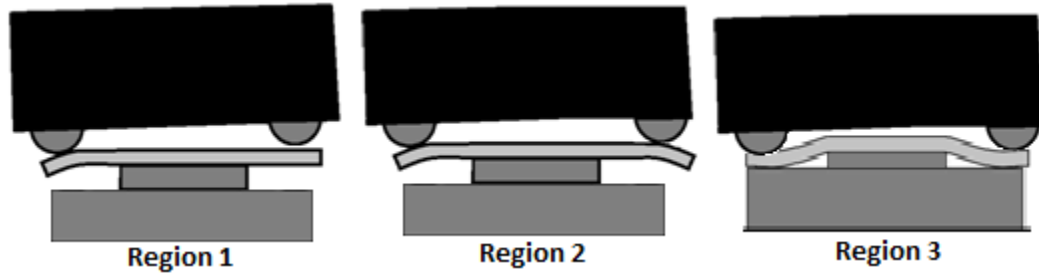Figure 7.4: Diagram of Fixtures and Shims in Series

Figure 7.5: Three Regions of Shim Stiffness Curve

was conducted measured the stiffness of the fixtures with the shims removed. This facilitated the identification of region one which is present with or without the shims. The second test that was conducted measured the stiffness of the standard shim setup. The third test that was conducted measured the shim setup with an additional shim inserted as a spacer between the bottom shim and the rigid base. This spacer caused region three to occur only at higher loads. The effect of the spacer is illustrated in Figure 7.6. When the results of these three tests are plotted together the boundaries of the three regions become much easier to identify.
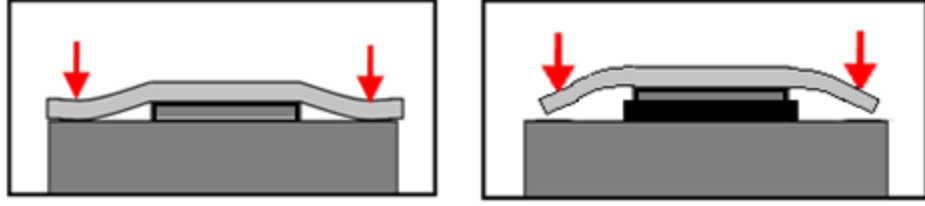
Figure 7.6: Effect of Spacer Inserted Below Bottom Shim

7.2   Valve 1 Results

Figure 7.7 shows the results of the three tests for valve 1. The stiffness curve of the standard shim setup is shown in Figure 7.8 with a first order polynomial trend of regions two and three. The slope of the trend line is equal to the stiffness of the shims and fixtures for each region. Figure 7.9 shows the stiffness curve of the fixtures alone.

The stiffness of region two can be calculated using Equation (7.1) where

$$k_{eff} = 2010 \, \text{lbf/in}$$

and

$$k_{fix} = 21,100 \, \text{lbf/in}.$$

Likewise, the stiffness of region three can be calculated using (7.1) where

$$k_{eff} = 13,700 \, \text{lbf/in}$$

and

$$k_{fix} = 21,100 \, \text{lbf/in}.$$

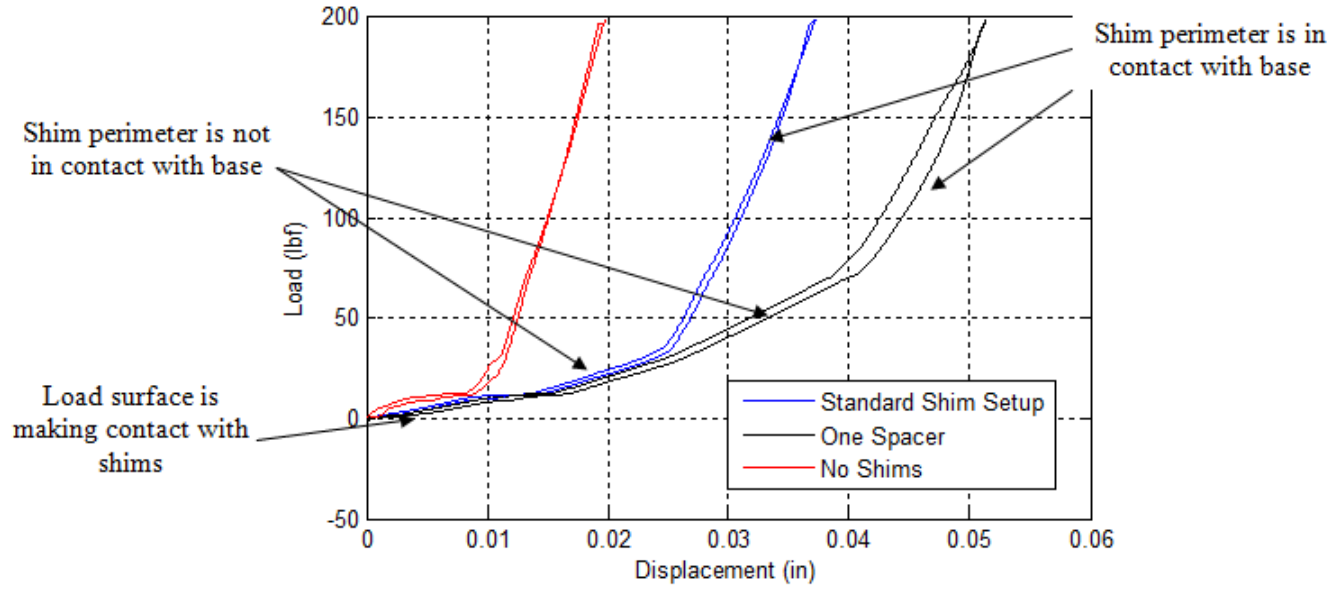The stiffness of shim stack one can be expressed by the piecewise function

43

Figure 7.7: Valve 1 Stiffness of Various Shim Setups

$$k_1 = \left\{ \begin{array}{ll} 2220 \, \text{lbf/in} & F < 34.0 \, \text{lbf)} \\ 39,300 \, \text{lbf/in} & F \geq 34.0 \, \text{lbf} \end{array} \right\}.$$
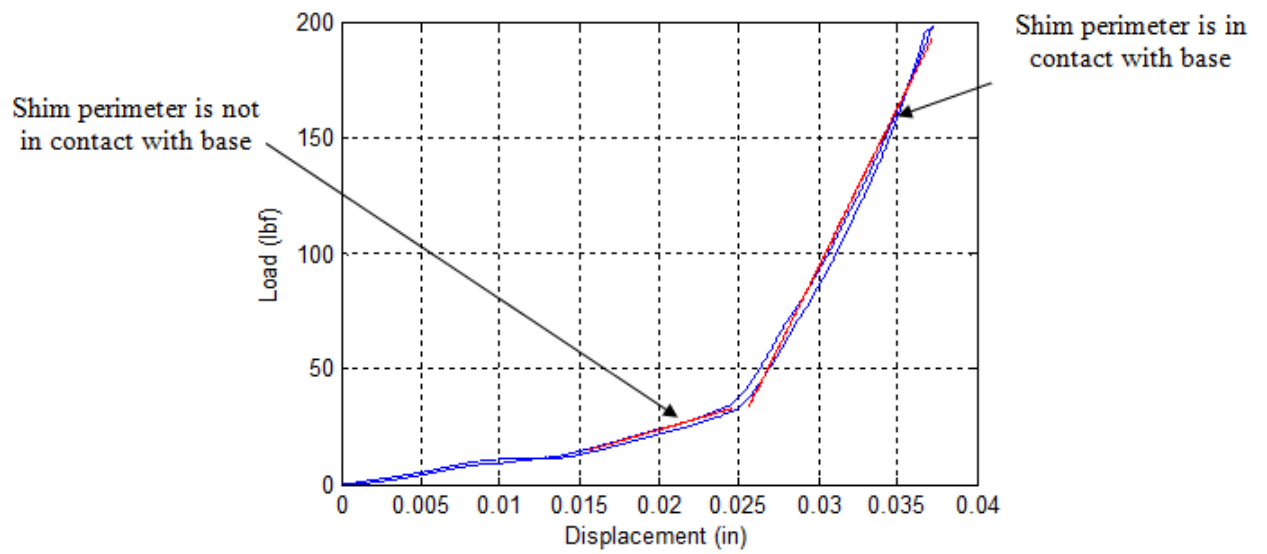
Figure 7.8: Valve 1 Effective Stiffness of Standard Shim Setup
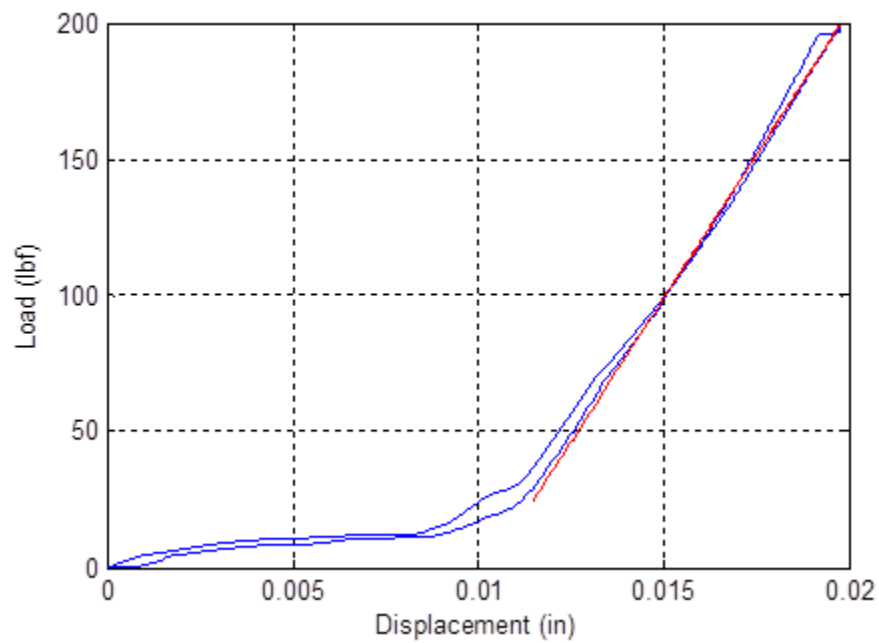

Figure 7.9: Valve 1 Fixture Stiffness

7.3 Valve 2 Results

Valve 2, the valve controlling flow of oil from chamber 1 to chamber 2 is unique from the other valves tested in that its shims can absorb much higher loads before making contact with the base. For this reason the valve 2 shims never made contact with the rigid base during testing and only two regions are seen. Figure 7.10 shows the fixture and shim stiffness. Figure 7.11 and Figure 7.12 show these two stiffness curves as well as linear polynomial trends of each curve.
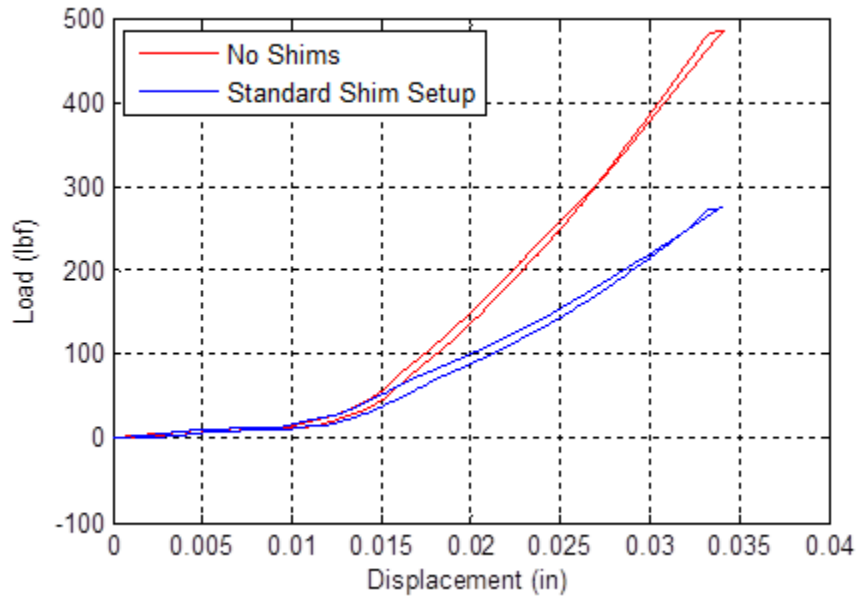

Figure 7.10: Valve 2 Stiffness of Various Shim Setups

The stiffness of this shim stack can be calculated using (7.1) where
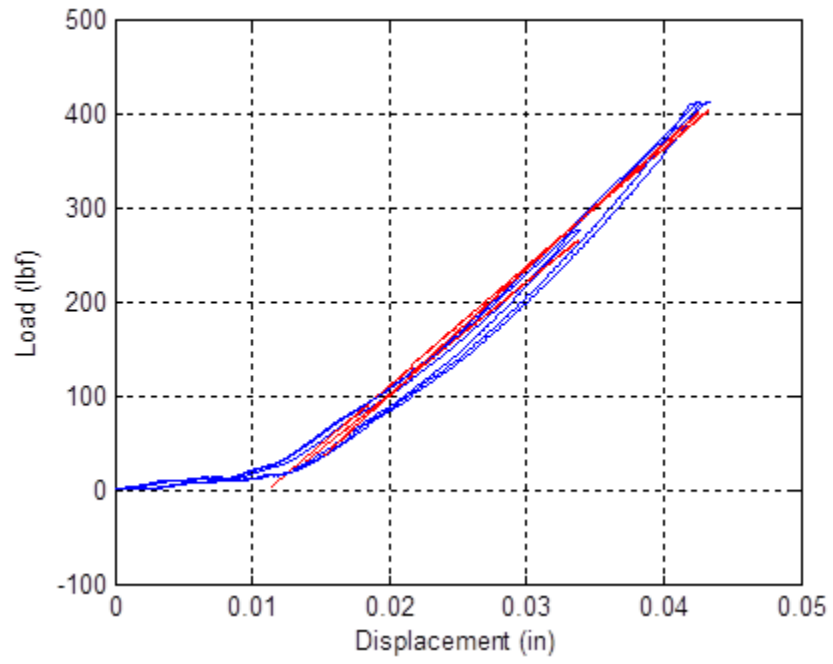
$$k_{eff} = 894 \, \text{lbf/in}$$

46

Figure 7.11: Valve 2 Stiffness of Standard Shim Setup

and

$$k_{fix} = 16900 \text{ lbf/in.}$$

This results in a stiffness of
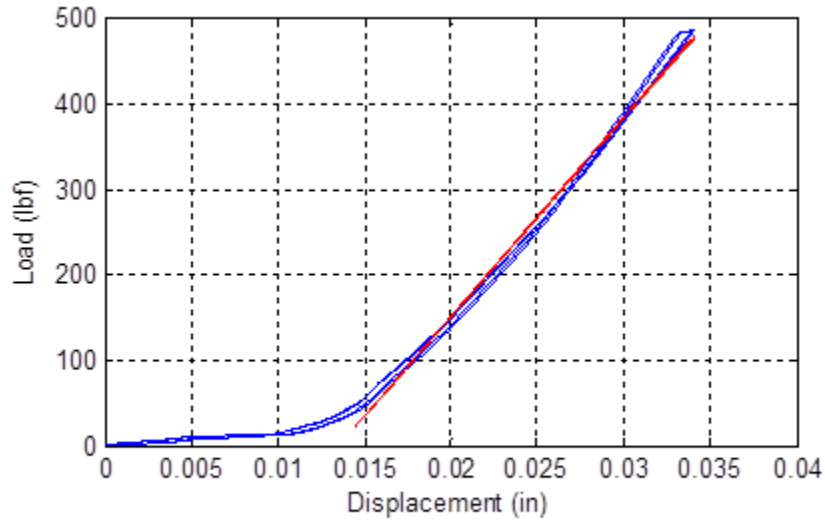
$$k_2 = 27400 \, lbf/in.$$

Figure 7.12: Valve 2 Fixture Stiffness

7.4   Valve 3 Results

Unlike the other valves tested in this study, valve 3 does not have a rigid backing to restrict the deflection of the shim. Thus the valve 3 shims do not exhibit the same three regions as the other valves. The results of the stiffness tests for this valve do show three different regions of the stiffness curve. However, these regions are a result of nonlinearities in the fixture stiffness curve. This was concluded because the nonlinearities of the fixture stiffness curve occurred at the same loads as the nonlinearities of the shim stiffness curve. These curves are plotted together in Figure 7.13. Region one is similar to region one of the stiffness curves for the other valves in this study. It occurs because the fixtures are not perfectly aligned and therefore

48

the initial contact between the loading fork and the shim is not instantaneous. The cause of the other regions of this curve is unknown.

The stiffness test was performed three times. The results of these tests can be seen in Figure 7.14. The average stiffness values for regions 2, 3, and 4 are shown in Table 7.1. These stiffness values must be substituted into Equation (7.1) to determine the stiffness of the valve isolated from the test fixtures. The results of the fixture stiffness tests are shown in Figure 7.15. The average fixture stiffness values obtained for regions 2, 3, and 4 are shown in Table 7.2.

Region	Stiffness (lb/in)
2	7760
3	7100
4	9490

Table 7.1: Valve 3 Average Total Stiffness Values

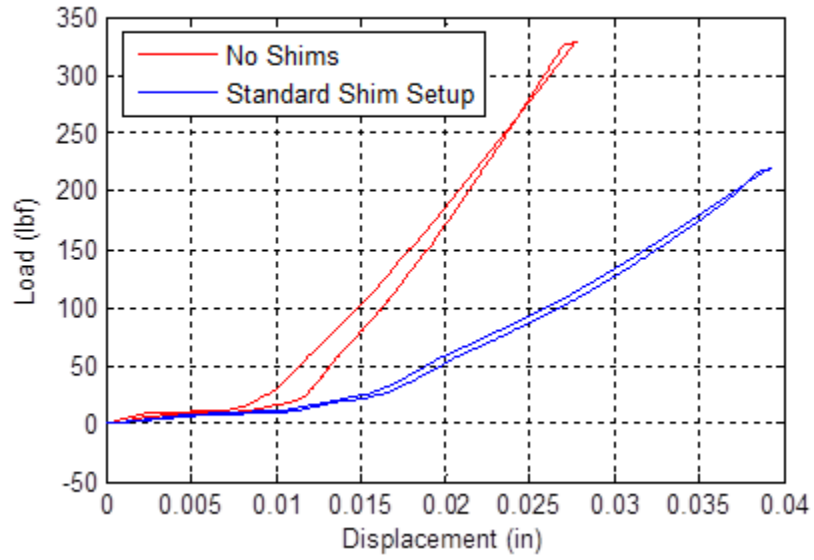| Region	Stiffness (lb/in)
2	15200
3	14600
4	18200

Table 7.2: Valve 3 Average Fixture Stiffness Values

Figure 7.13: Valve 3 Stiffness of Various Shim Setups

The stiffness of region two can be calculated using Equation (7.1) where

$$k_{eff} = 7760 \, \text{lbf/in}$$

and

$$k_{fix} = 15200 \, \text{lbf/in}.$$

Likewise, the stiffness of region three can be calculated using (7.1) where

$$k_{eff} = 7100 \, \text{lbf/in}$$

and

$$k_{fix} = 14600 \, \text{lbf/in}.$$

The stiffness of region four can also be calculated using (7.1) where

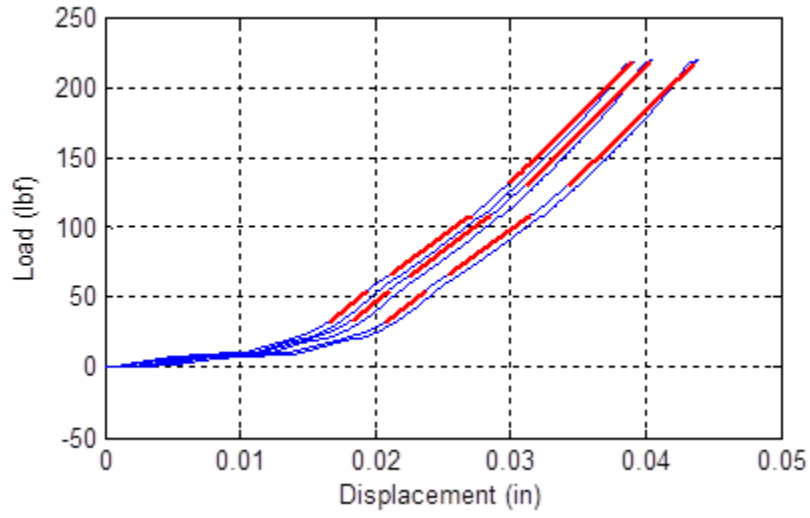$$k_{eff} = 9490 \, \text{lbf/in}$$

Figure 7.14: Valve 3 Standard Shim Setup Stiffness

and

$$k_{fix} = 18200 \, \text{lbf/in}.$$

The stiffness of the valve 3 shim stack can be expressed by the piecewise function

$$k_3 = \left\{ \begin{array}{ll} 15800 \, \text{lbf/in} & F < 65.0 \, \text{lbf} \\ 13800 \, \text{lbf/in} & 65.0 \, \text{lbf} \leq F < 130 \, \text{lbf} \\ 19900 \, \text{lbf/in} & F < 130 \, \text{lbf} \end{array} \right\}.$$
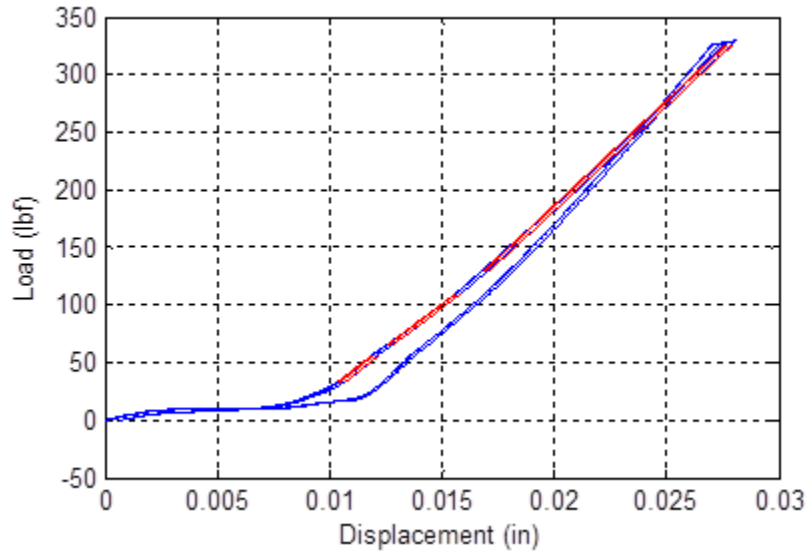
Figure 7.15: Valve 3 Fixture Stiffness

7.5 Valve 4 Results

Valve 4 is subjected to significantly smaller pressure differentials than the other valves. Thus its shims are subjected to smaller loads. For this reason the stiffness of the valve 4 shims is much smaller than that of the other valves. This made stiffness testing difficult because the perimeter of the cantilevered shims would come into contact with the base at very small loads. Because of this region 2 is difficult to distinguish from region 3 using the stiffness curve of the standard shim setup in Figure 7.16.

The stiffness curve of the shims with one spacer can be used to determine the stiffness of region 2. The region 2 stiffness of the shims with one spacer is approximately equal to the region 2 stiffness of the standard shim setup in series with the spacer.

The spacer that was used was a steel washer with a thickness of 0.012 in. The stiffness of this washer is assumed to be infinite. By using this assumption, the stiffness of region 2 of the standard shim setup can be found by determining the stiffness of region 2 of the shim setup with the spacer. This stiffness is shown in Figure 7.17.
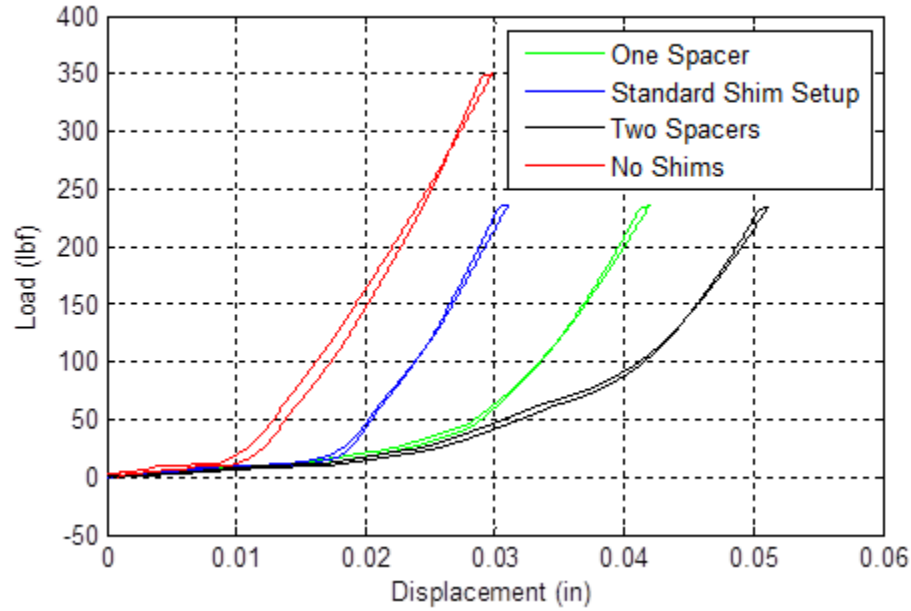

Figure 7.16: Valve 4 Stiffness of Various Shim Setups

The stiffness of region two can be calculated using (7.1) where

$$k_{eff} = 2490 \text{ lbf/in}$$

and

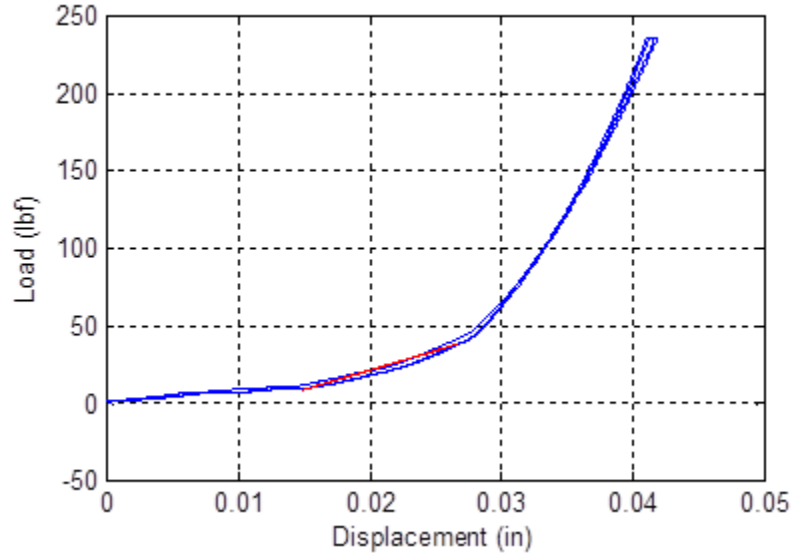$$k_{fix} = 18500 \text{ lbf/in}.$$

Figure 7.17: Valve 4 Stiffness of Shim Setup with One Spacer

Likewise, the stiffness of region three can be calculated using (7.1) where

$$k_{eff} = 18500 \, \text{lbf/in}$$

and

$$k_{fix} = 18500 \, \text{lbf/in}.$$

Because k_{eff} is approximately equal to k_{fix} the stiffness of the shims can be assumed to be infinite in region 3.

The stiffness of shim stack four can be expressed by the piecewise function

$$k_4 = \left\{ \begin{array}{ll} 2870 \, \text{lbf/in} & F < 20.5 \, \text{lbf} \\ \infty & F \geq 20.5 \, \text{lbf} \end{array} \right\}.$$
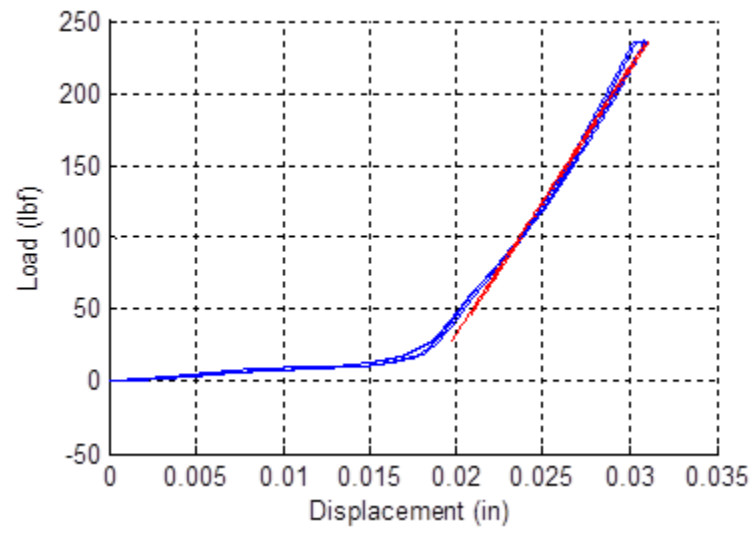
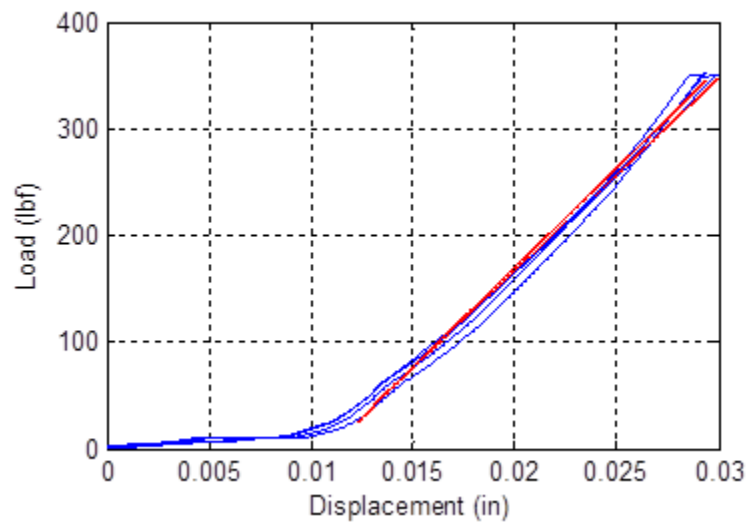Figure 7.18: Valve 4 Stiffness of Standard Shim Setup

Figure 7.19: Valve 4 Fixture Stiffness

Chapter 8: VALVE RESISTANCE - EXPERIMENTAL SHIM CHARACTERIZATION USING FLUID TESTING

The initial shim stiffness measurement provided a good approximation of the actual shim stiffness. However, there were several drawbacks to this experiment. The main drawback was that the loading of the shims was simplified in order to apply this load in a mechanical test. Another weakness of the mechanical stiffness tests is that the dynamics of the shims were not studied. This type of static test is compatible with the model developed in Chapter 3 which does not include shim dynamics. Nevertheless, it is important to study the dynamics of the shims in order to determine sources of error in this model and plan for improvements to future models.

The purpose of the experiment discussed in this section is to obtain a relationship between pressure drop across the piston head and deflection of the the piston shims when the shims are loaded as they are in the damper. From this relationship the shim stiffness can be derived if the relationship between pressure and shim force is known or assumed. This test was performed several times with modifications done each time to improve the results. This section describes the original experimental setup, the modifications done between each test, and the results of each test.

8.1 Experimental Setup

The most challenging part of this experiment was making the shims accessible for measurement. In order for the shims to be measured by the laser displacement transducer a special apparatus was built. The apparatus includes an acrylic lens through which the laser could be shone onto the shims. Hydraulic fluid can be pumped through this apparatus to create fluid pressure that would deform the shims. A pressure transducer is located on each side of the piston to measure the pressure drop across the valve. A diagram of the setup is shown in Figure 8.1.
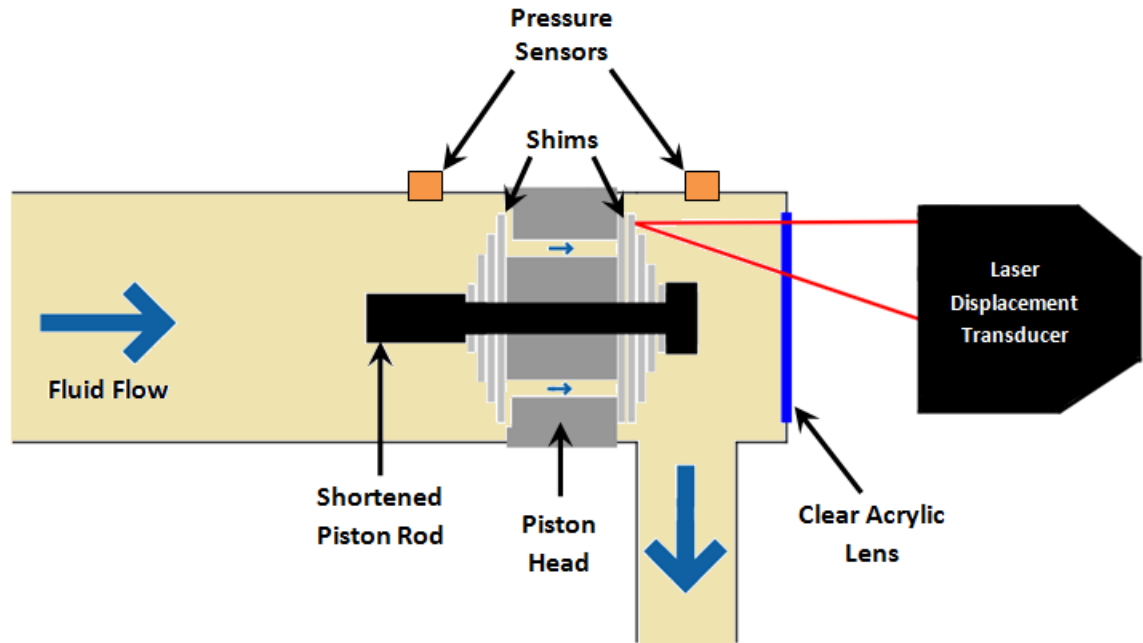
Figure 8.1: Diagram of Experimental Setup for Fluid Shim Stiffness Testing

The apparatus was machined in two pieces that could be fastened down around the piston head. The orignial apparatus is shown in Figure 8.2 and an exploded view is shown in Figure 8.3. The fluid flow was controlled by a hydraulic cylinder with a 1.5" bore shown on the right in Figure 8.4. A damper dynomometer was used to cycle the hydraulic cylinder at various frequencies. The dynomometer applied a sine wave displacement to the hydraulic piston. To vary the peak speed of the piston the frequency was varied while the stroke length remained constant at 50 mm. (In this document test speeds will be referred to by the peak speed of the piston in mm/s with speeds ranging from 10 mm/s to 1000 mm/s.) This setup alternates the direction of the flow. However, the shim displacement can only be measured on one side of the piston at a time. Therefore, only the data for flow causing the deflection of the shims being measured is important.
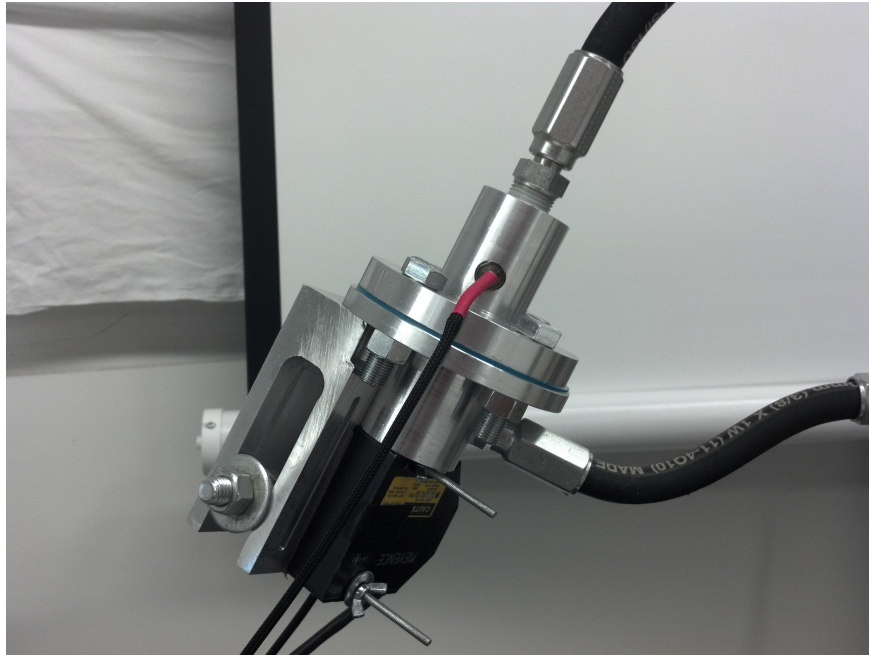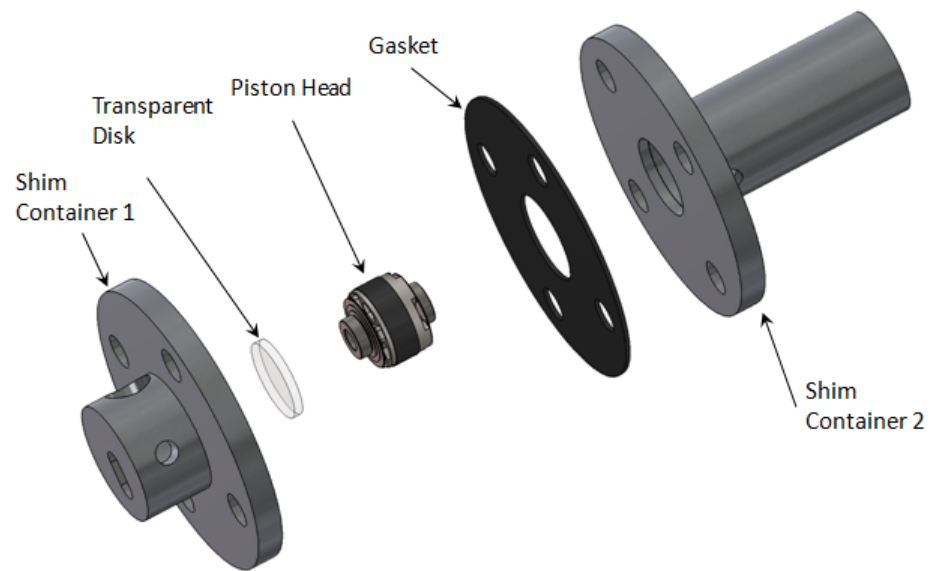
Figure 8.2: Container for Shims

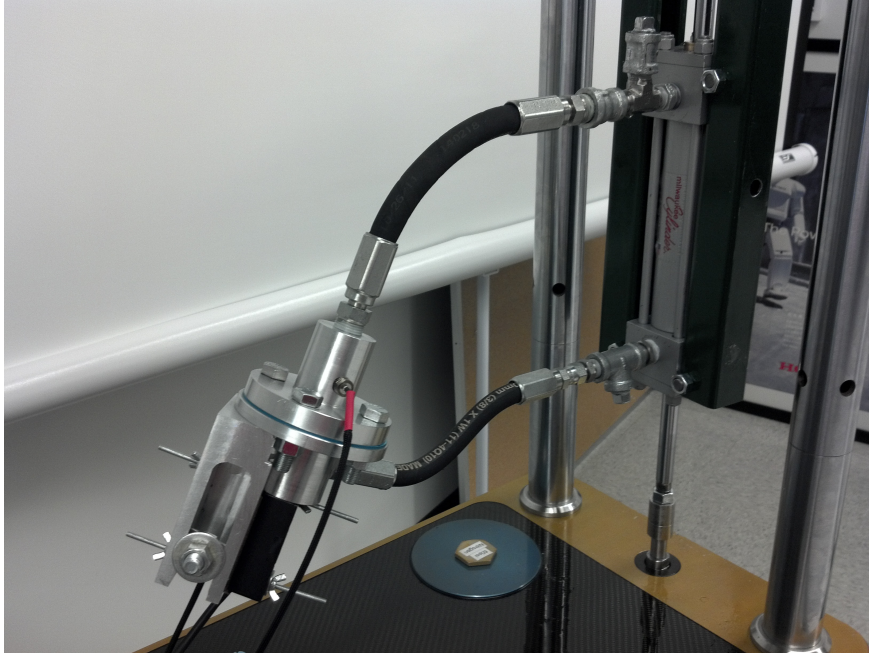Figure 8.3: Exploded View of Shim Container

Figure 8.4: Shim Container Attached to Hydraulic Cylinder

8.2 Test 1

Test 1 was run at several peak piston speeds ranging from 10 mm/s to 100 mm/s. Higher speeds were not able to be run because the hydraulic oil became cloudy blocking the laser from obtaining readings. The speeds below 70 mm/s are not shown because the displacements were too small to be detected by the laser.

8.2.1 Results

Figures 8.5 through 8.8 show the pressure drop across the piston and the shim deflection for several dyno speeds. The results show that the displacement of the shims is not the only displacement that is being measured. When no force is applied, the shim is flush with piston head. When a positive pressure drop is present, the shim

60

should deflect away from the piston head which is measured by the displacement sensor as a positive deflection. However, when a negative pressure drop is present the shim should have zero deflection since the piston head prevents it from deflecting in the negative direction. The results do not reflect this hypothesis. As can be seen in Figures 8.5 through 8.8, displacement is detected in both directions.
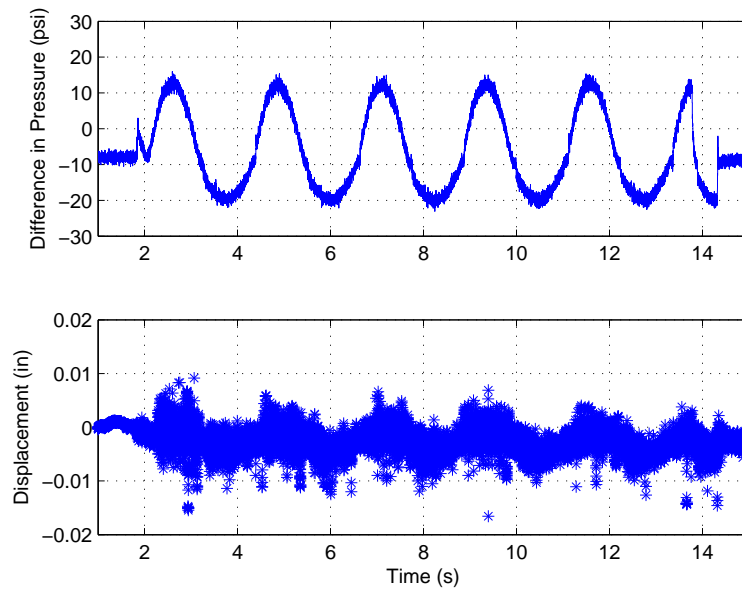

Figure 8.5: Pressure Drop Across Piston and Shim Deflection for a Peak Dyno Speed of 70 mm/s

It is likely that the cause of this negative deflection is compliance between the shim container and the piston head. As seen in Figure 8.9, the piston head has a compliant seal around its circumference. This seal protrudes out of the piston head creating a lip. This lip was mated with the lip in the shim container shown in Figure 8.10. This was done to hold the piston head in place inside the shim container. Since
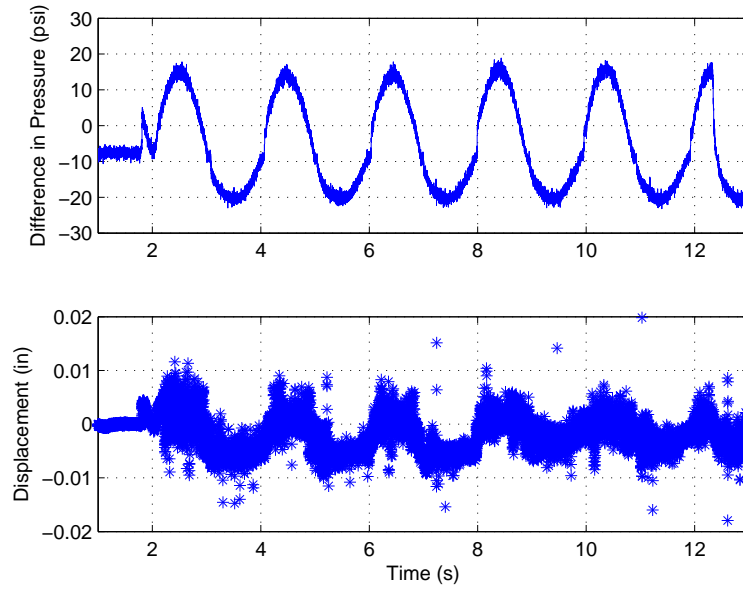
Figure 8.6: Pressure Drop Across Piston and Shim Deflection for a Peak Dyno Speed of 80 mm/s

this lip is compliant it deforms when fluid pressure is applied. This causes a slight displacement of the entire piston head. This displacement can take place in both directions. Since the the magnitude of the displacement is similar in the positive and negative directions it can be assumed that the actual shim deflection is negligible and that the measured displacement is due purely to displacement of the entire piston head (even in the positive direction).
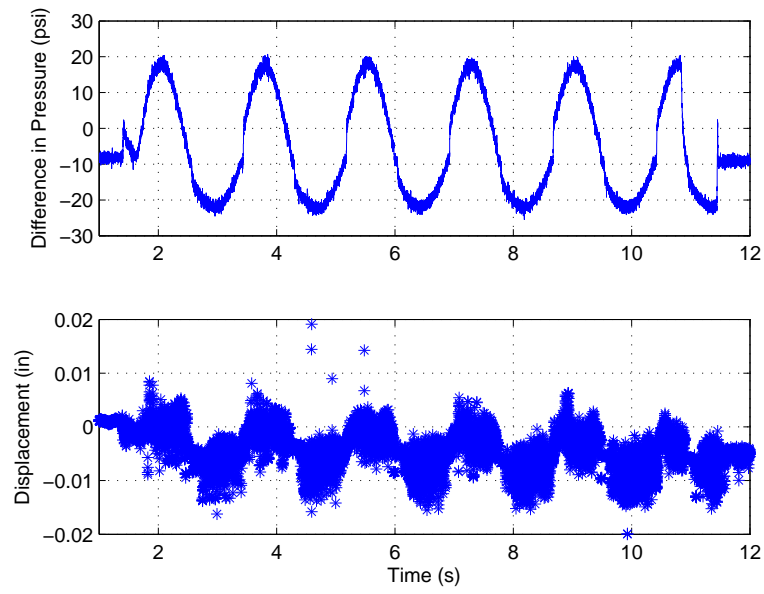
Figure 8.7: Pressure Drop Across Piston and Shim Deflection for a Peak Dyno Speed of 90 mm/s
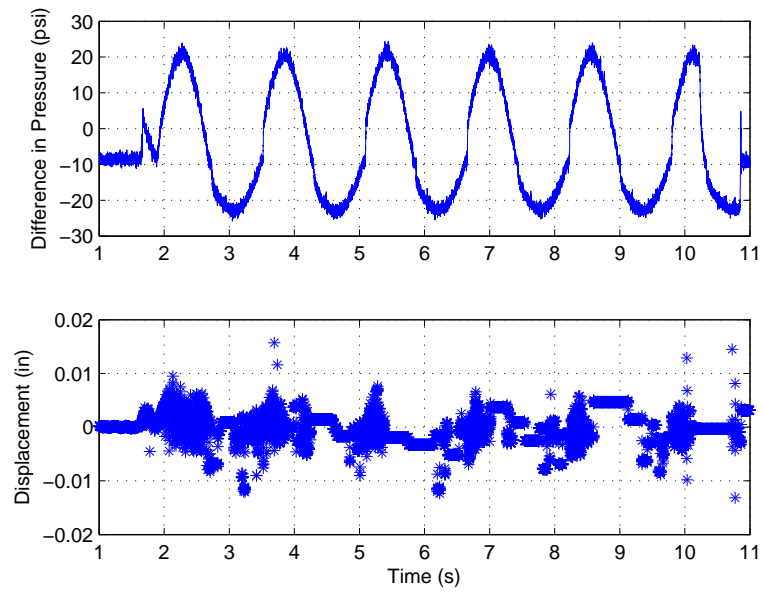
Figure 8.8: Pressure Drop Across Piston and Shim Deflection for a Peak Dyno Speed of 100 mm/s
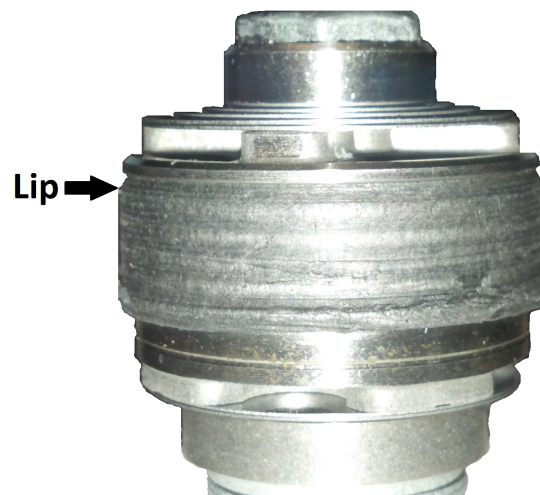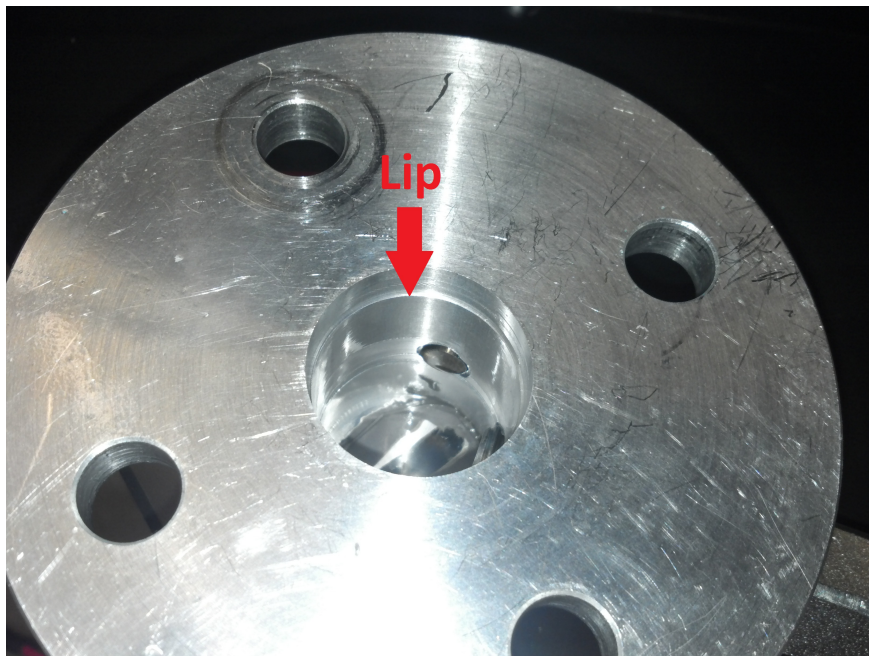
Figure 8.9: Piston Head

Figure 8.10: Shim Container Lip

8.2.2 Modifications following Test 1

In order to obtain accurate shim displacement data, the compliance between the piston head and the container needed to be minimized. One way to do this was to attach a collar to the piston head using set screws as shown in Figure 8.11. This collar could then be fastened to the container using screws. Material was machined from the the container to make space for this collar. Figure 8.12 shows an exploded view of this setup. This was the final modification to the shim container although modifications were made to other parts of the system after test 2. Drawings of the parts fabricated for the shim container are shown in Appendix F
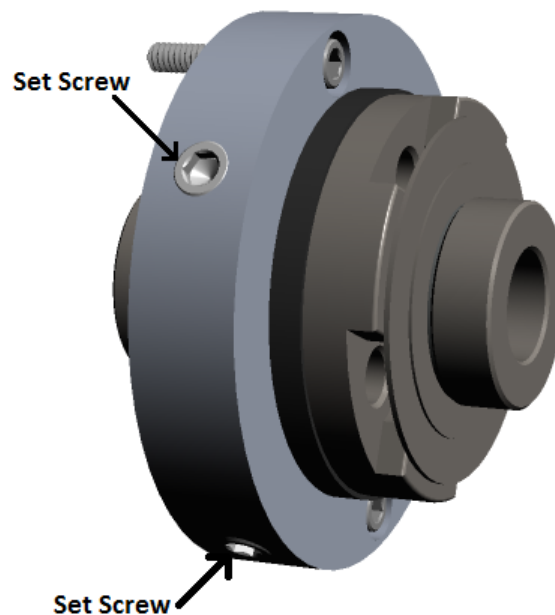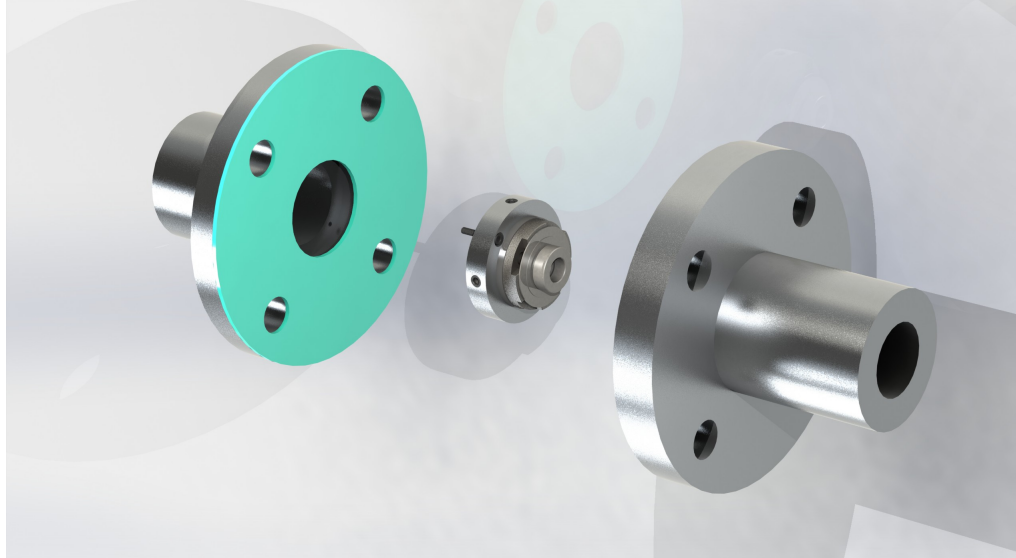

Figure 8.11: Piston Collar

Figure 8.12: Exploded View of New Shim Container Setup

8.3 Test 2

The modifications made after the first fluid shim test were able to improve the results gathered in the second test. However, new issues arose in the second test. These issues were a change in the resting location of the shims and a loss of transparency of the hydraulic fluid preventing the laser displacement transducer from taking measurements. The results are discussed below followed by a discussion of these issues.

Resting Location of the Shims

The shim setup allows for shim displacement in only one direction as shown in Figure 8.13. In this study the direction in which the shims can travel is taken as the positive direction and the resting location of the shims is taken as zero. This means that the measured displacement of the shims should never be negative even when a
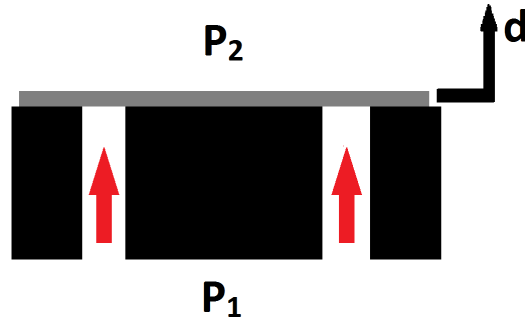
Figure 8.13: Diagram of piston head and shims

negative pressure differential is applied. A negative pressure differential should result in zero displacement.

The data shows that the displacement signal flattens out at negative pressure differentials as expected. However, the displacement value of this flat spot at negative pressures is not consistent. This can be seen in Figure 8.14. In this test the displacement of the shims at negative pressure differentials is approximately zero for the last two cycles. However, for the first three cycles the displacement drops down to about -0.005" when a negative pressure differential is applied. A similar phenomenon takes place in the 120 mm/s and 200 mm/s tests. This is what causes the displacement-pressure plot to split at low pressures as seen in Figure 8.15.

It should also be noted that the initial position of the shims changes with each test. Figure 8.16 shows this change.

When the oil was removed from the system it contained bits of teflon tape that had come from various threaded components in the system. It is likely that the change in resting shim location was caused by pieces of teflon that get caught between the bottom shim and the piston face.
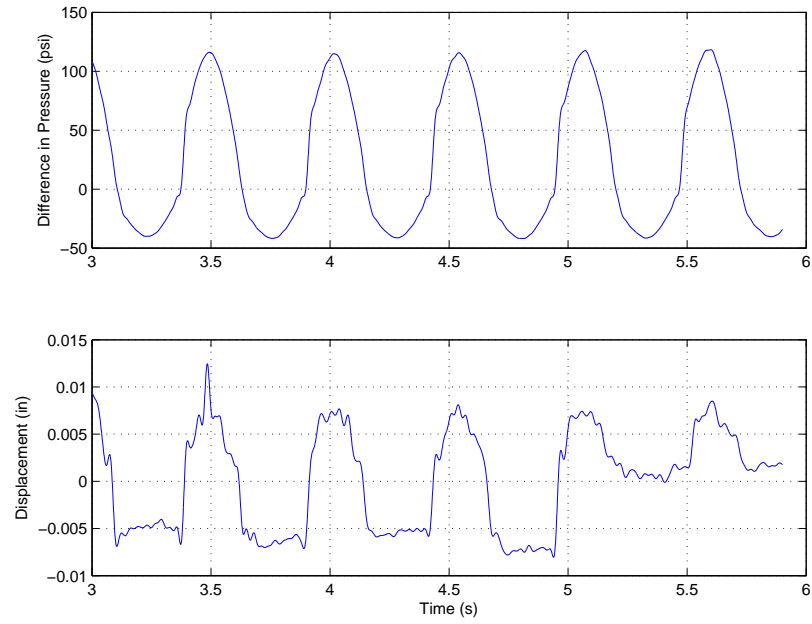
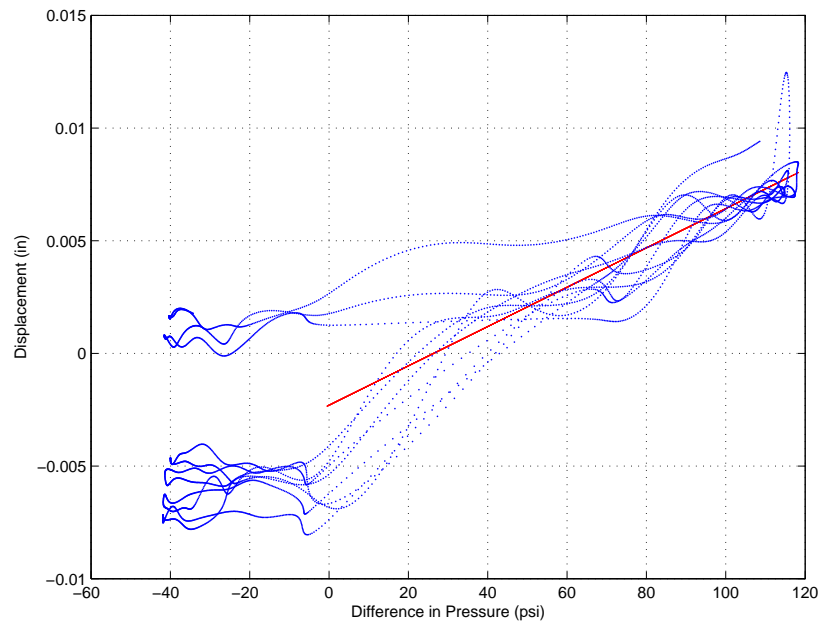Figure 8.14: Displacement and pressure over time for 300 mm/s peak piston speed

Figure 8.15: Displacement versus pressure for 300 mm/s peak piston speed using shifted filtered displacement signal
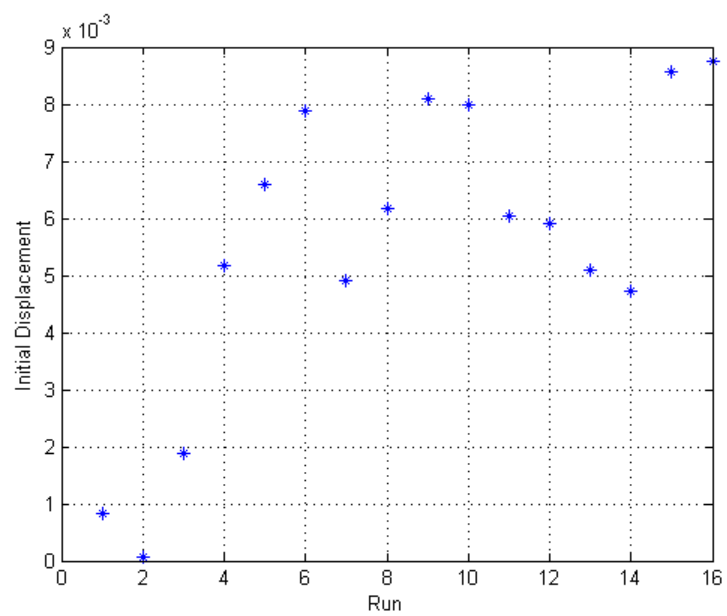
Figure 8.16: Change in initial shim displacement between tests

Loss of Oil Transparency

Another issue that occurred during this test was loss of oil transparency. This posed a problem because the laser displacement transducer will only work through a transparent medium. The oil was initially transparent and the laser was able to take measurements. The oil remained transparent at low speed tests. However, when the hydraulic piston was cycled at higher speeds, the signal from the laser became unstable and was eventually lost completely. It was determined that this was due to two separate phenomena. When the damper was cycled, localized pockets of low pressure would form in the fluid. When the pressure in these pockets dropped below the vapor pressure of the oil, cavitation would occur; this would create gas bubbles in the fluid. These gas bubbles would then travel across the path of the laser scattering its light and temporarily disrupting the acquired displacement signal. In addition to this, the oil became less transparent due to contamination. When the oil was removed from the system, in addition to the bits of teflon tape, it had a slight dark tint to it. It seems that the oil was getting contaminated by the black Buna-N rubber hose. The effect was minor but was enough to prevent the laser from taking measurements.

8.3.1   Results

The individual test results are shown in Appendix B. A relationship between shim displacement and pressure difference was obtained by plotting maximum displacement against maximum pressure difference for each test. A trend line for this plot would represent the linear relationship between pressure and shim displacement. Figure 8.17 shows this plot with the linear trend line. The variance of the the resting location of the shims does not appear to have an effect on the location of the shims at maximum
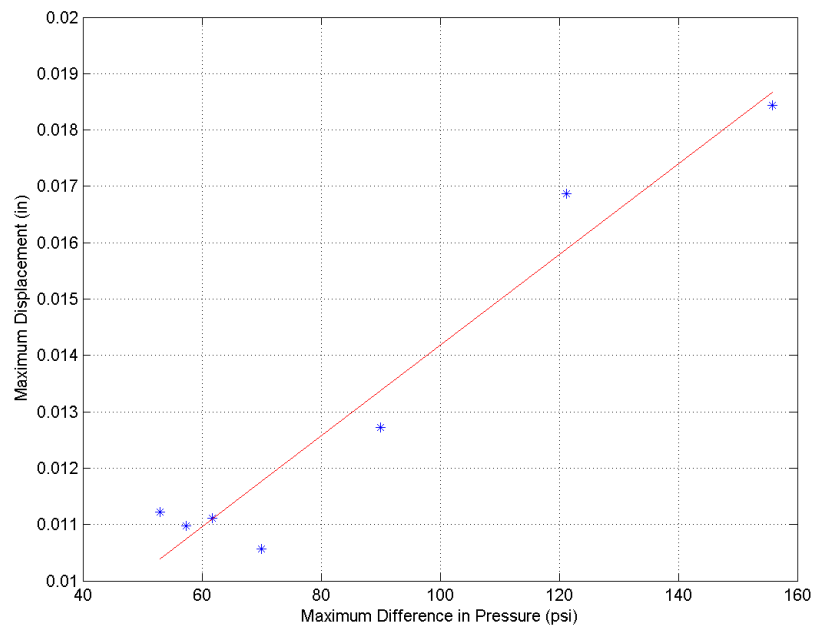
Figure 8.17: Maximum displacement versus maximum pressure differential for various peak piston speeds

pressure. Figure 8.17 shows the maximum displacement plotted against the maximum pressure difference.

8.3.2 Modifications Following Test 2

The issues described above were addressed through hardware modifications. One of the two rubber hoses was removed completely and the other was shortened in order to minimize oil contamination from the rubber. The teflon tape used to seal the pipe threads was also removed and replaced by a liquid thread sealant. Another modification that was made was the addition of a hydraulic accumulator. This accumulator could be charged with gas to bias the system pressure. This is beneficial because it can prevent bubbles caused by cavitation and possibly aeration from blocking the path of the laser displacement transducer. The modified system is shown in Figure 8.18.
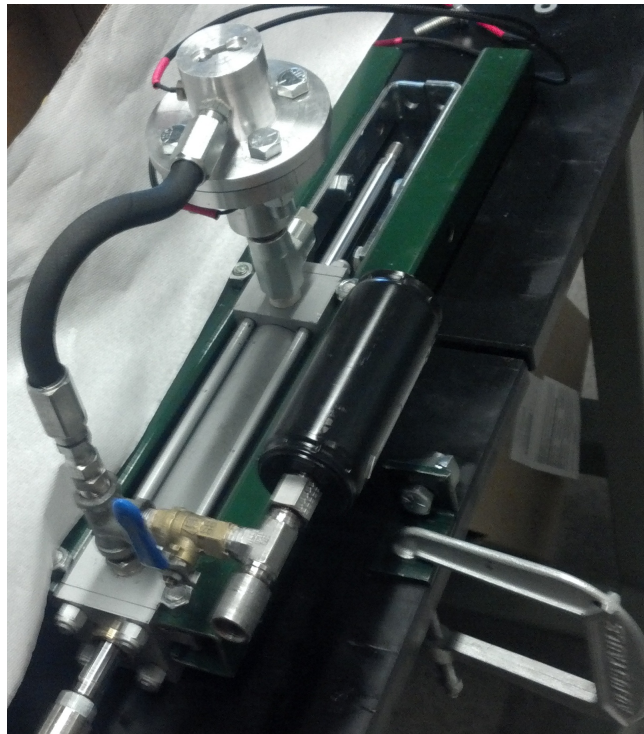
Figure 8.18: Modified System

8.4 Test 3

The modifications done after test 2 had excellent effects on the performance of the system. The fluid pressure was biased to approximately 100 psi. This bias pressure prevented cavitation from disrupting the laser signal and the reduction in hose lenght allowed all of the desired tests to be completed before the oil became contaminated enough to block the laser. The testing was done at Honda R&D in Raymond, Ohio. Data was taken for peak speeds ranging from 100 mm/s to 1000 mm/s.

Data from each test is shown in Appendix C. However, only data from four tests will be analyzed in this section. These are the tests with peak speeds of 200 mm/s, 300 mm/s, 400 mm/s, and 500 mm/s. The data from these tests is shown in Figures 8.20 through 8.23. It should be noted that this data was acquired using a low pass filter. See Appendix C for the raw data.

8.4.1 Overview of Results

The data from the 200 mm/s and 300 mm/s peak speed was as expected. There was zero shim displacement for negative pressure differentials and there was a relatively linear relationship between shim displacement and pressure differential for positive pressure differentials. Figures 8.24 and 8.25 show this relationship and a line representing a linear regression of the data. The tests with peak speeds over 300 mm/s produced surprising results. There are two unexpected phenomena that are apparent in this data. One is that at high frequencies the shims displace in the positive direction for positive pressure differentials and for negative pressure differentials. The second is that the shims displacement is limited. At high pressure differentials the displacement stops increasing at around 0.007" and even begins to decrease slightly.
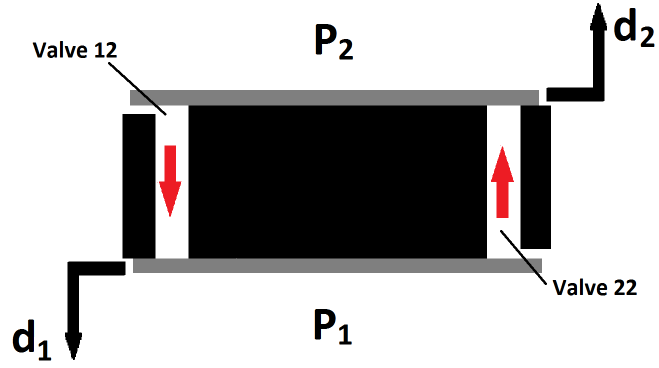
73

Figure 8.19: Diagram of piston head and shims

This can be seen clearly in Figures 8.26 and 8.27. These two phenomena, although difficult to explain, are compatible with each other. Figure 8.19 shows a diagram of valves 12 and 22. If valve 22 opens at negative pressure differentials, then it is possible that valve 12 opens at positive pressure differentials. This would decrease the flow through valve 22 thus decreasing the measured displacement, d_2.
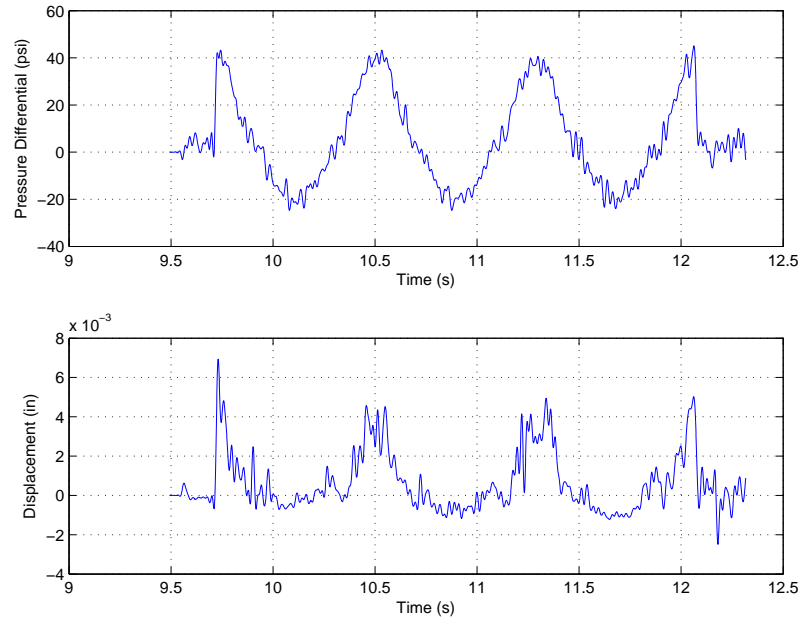
Figure 8.20: Filtered displacement and pressure over time for 200 mm/s peak piston speed
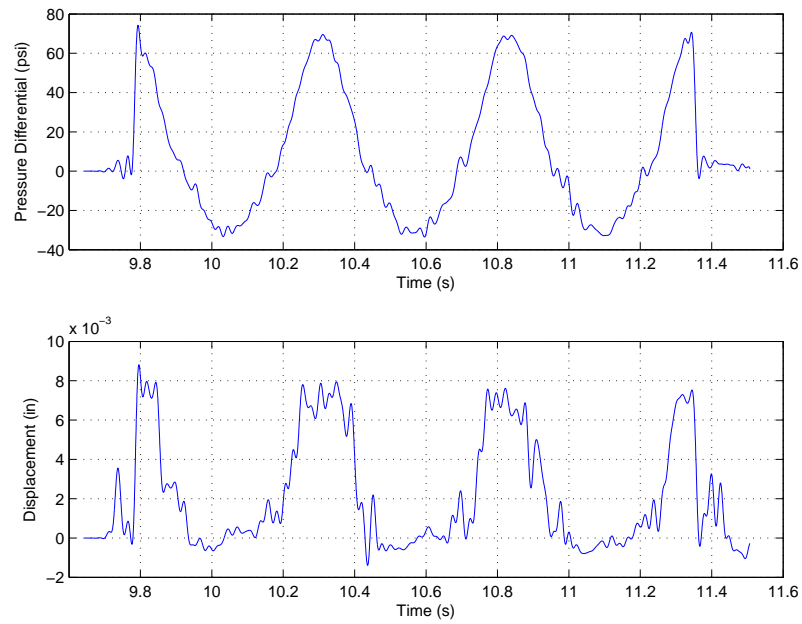
Figure 8.21: Filtered displacement and pressure over time for 300 mm/s peak piston speed
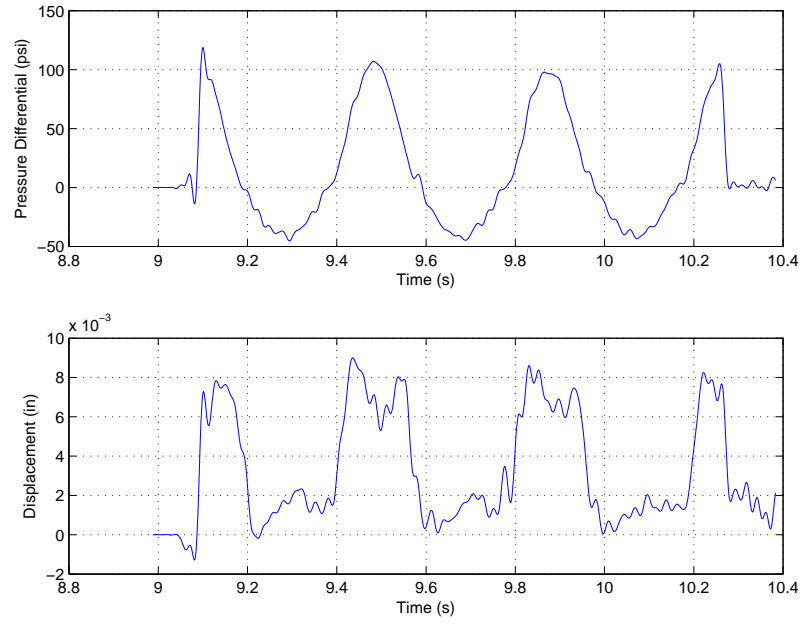
Figure 8.22: Filtered displacement and pressure over time for 400 mm/s peak piston speed
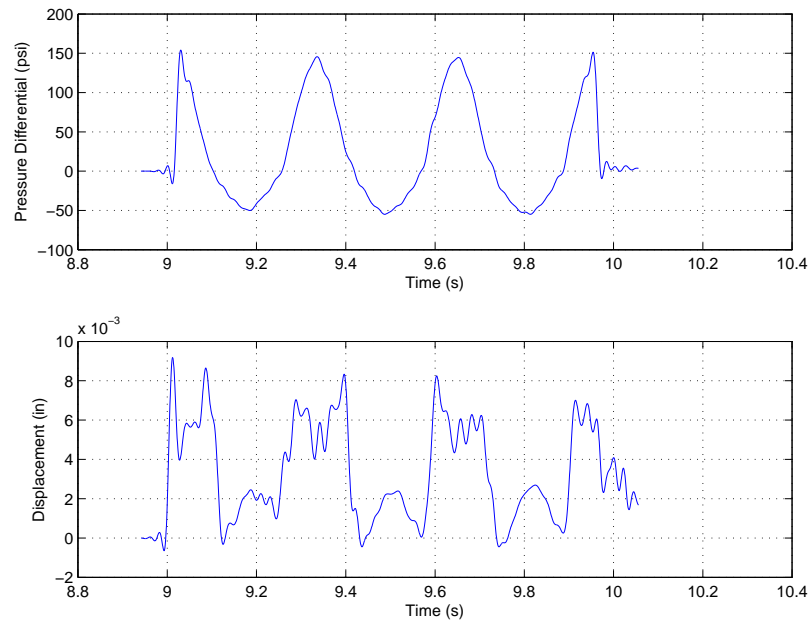
Figure 8.23: Filtered displacement and pressure over time for 500 mm/s peak piston speed
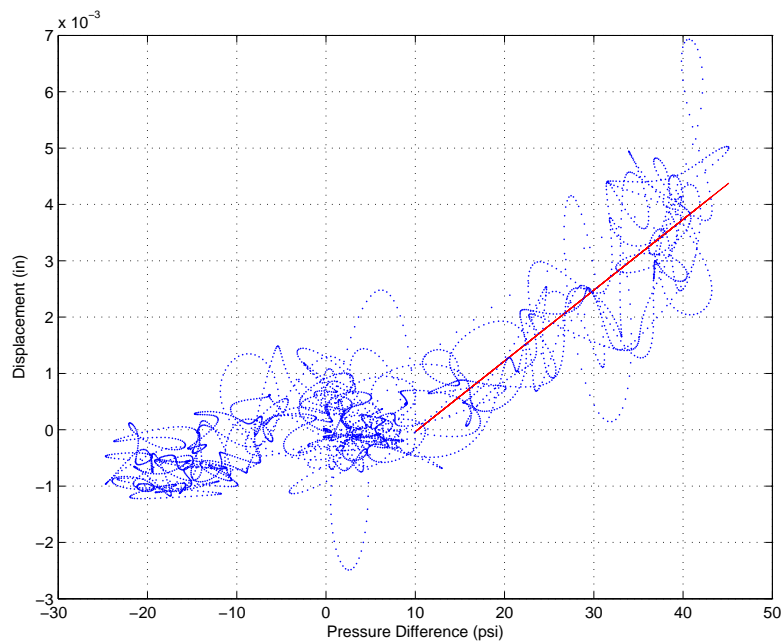
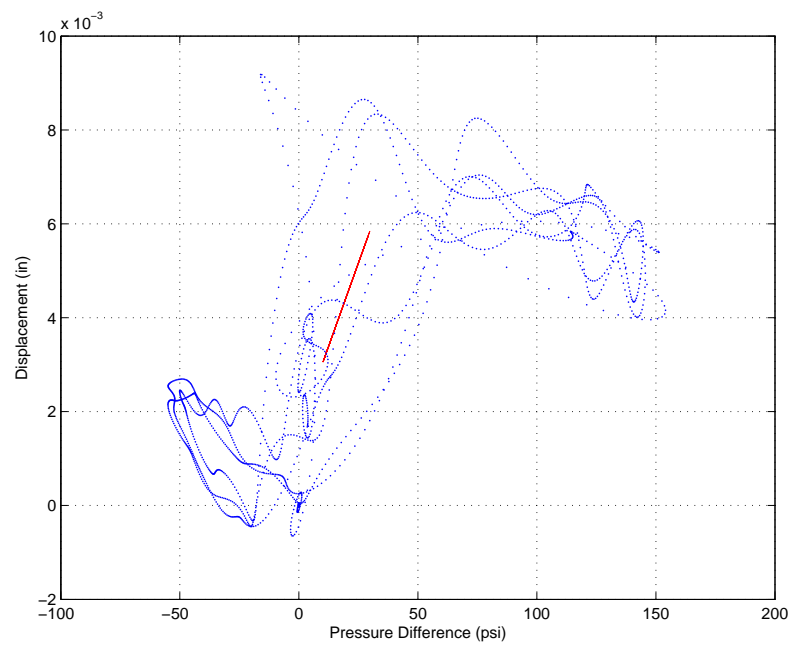Figure 8.24: Displacement versus pressure for 200 mm/s peak piston speed
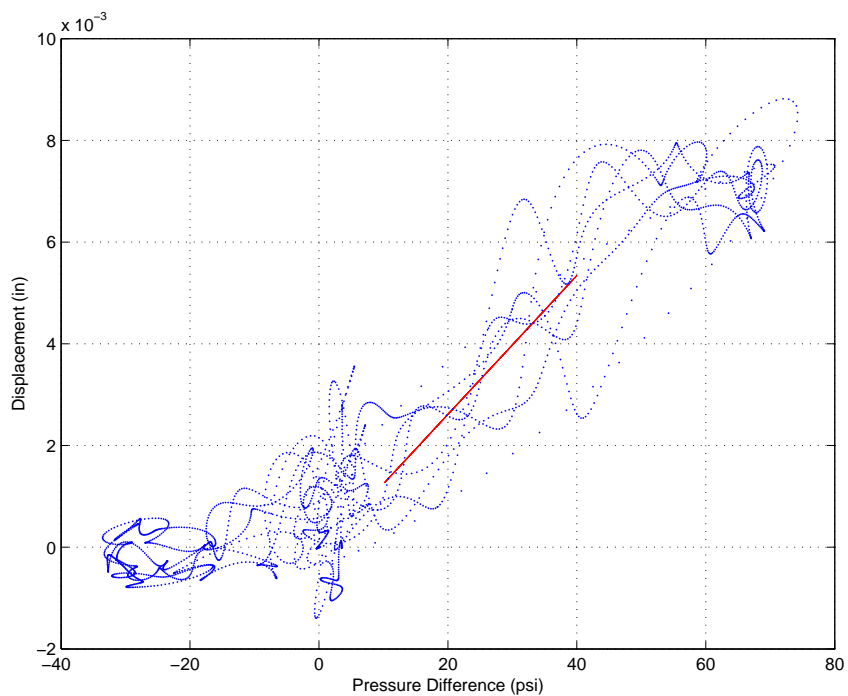
Figure 8.25: Displacement versus pressure for 300 mm/s peak piston speed
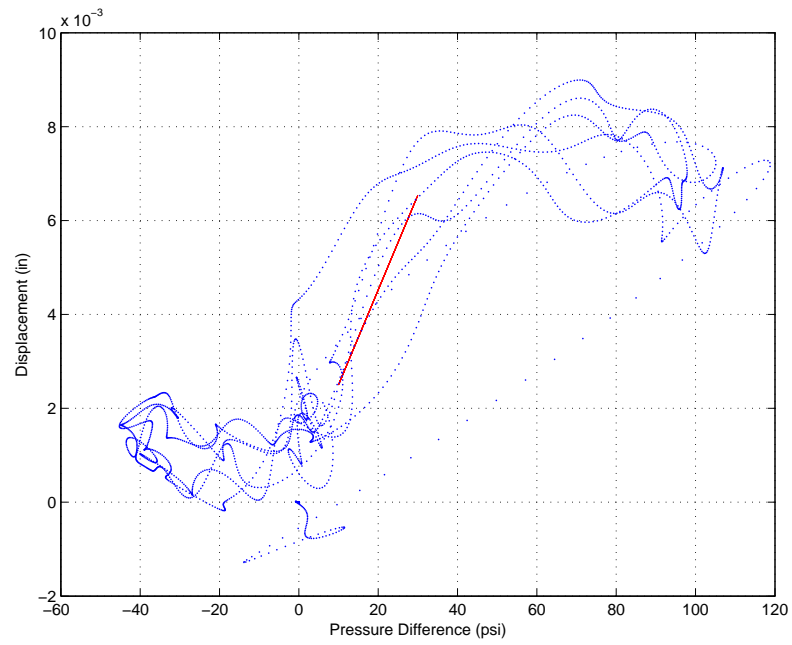
Figure 8.26: Displacement versus pressure for 400 mm/s peak piston speed

Figure 8.27: Displacement versus pressure for 500 mm/s peak piston speed

8.4.2 Investigation of Positive Shim Displacement at Negative Pressure Differentials

Several simulations were run to determine if it is possible for the shims to displace positively at negative pressure differentials. The first simulation was run to determine if it is possible for a positive resultant force to occur. This was a computational fluid dynamics simulation that was run using the multiphysics package COMSOL. Figure 8.28 shows the model geometry and the velocity profile of the fluid. Figure 8.29 shows a zoomed image of the pressure profile. It can be seen from this image that the resultant force on the shim is negative and would not cause positive displacement.
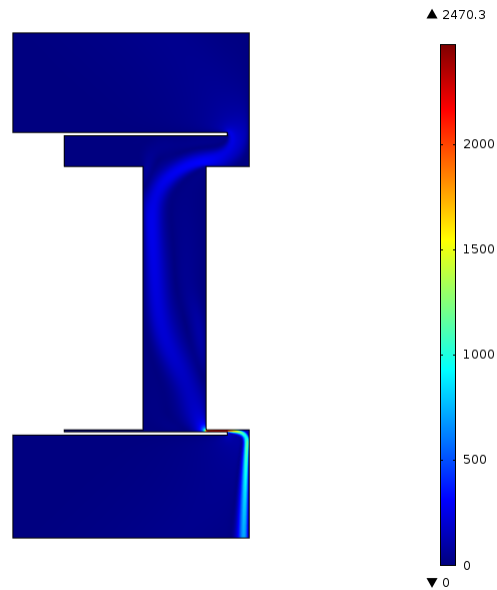
Figure 8.28: Velocity profile of back pressure simulation

A second simulation was run to determine if the shim could be deflecting negatively at some locations but positively at others. This simulation was a solid mechanics
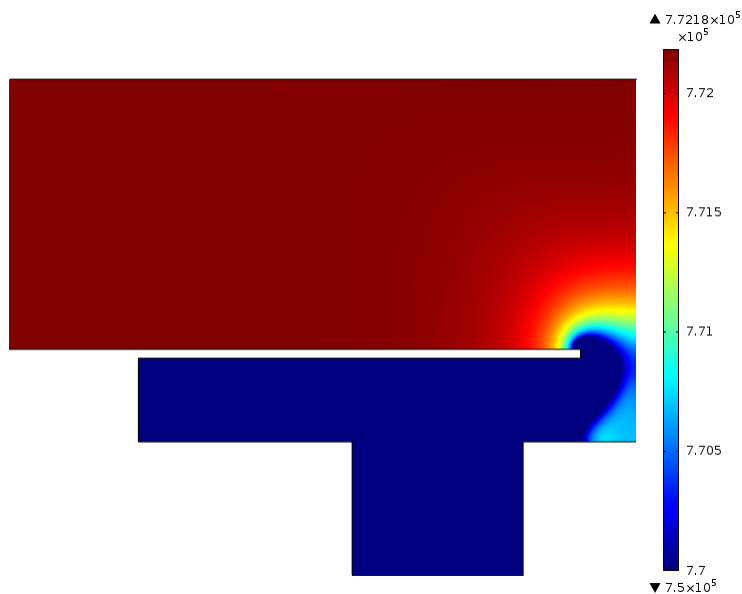
Figure 8.29: Pressure profile of back pressure simulation

finite element model also run using COMSOL. The model, shown in Figure 8.30, was built as a quarter model with two symmetrical boundary conditions. The roller boundary conditions were placed on the model to immidate the contact between the valve and the shim. The model was probed at the boundaries of symmetry for positive displacement. Figure 8.31 shows the resulting displacement profile. It is clear from this image and from the probed displacement values that there is no significant positive displacement.

The positive shim displacement that has been observed at negative pressure differentials is a phenomenon that cannot be explained at this time. It is likely that this is an effect of the dynamic loading. This would explain why it is not present in the static simulations that were considered. It is also possible that the data is not correctly representing the actual movement of the shims. However, there is no

80
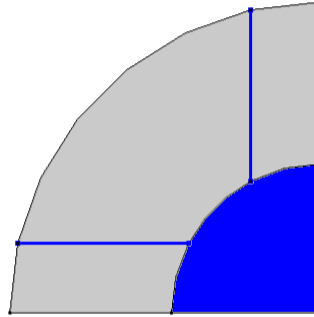
Figure 8.30: Boundary conditions of back displacement simulation

p1(10)=1000   Surface: Total displacement (in)
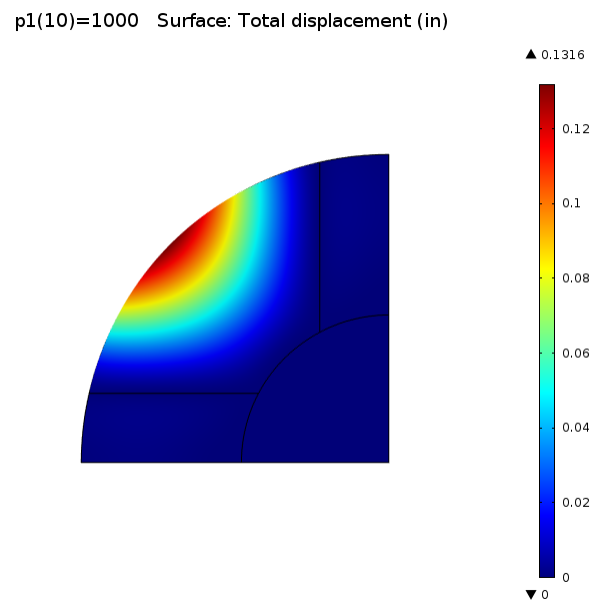
Figure 8.31: Displacement profile of back pressure simulation

other evidence of this. Additional testing will need to take place if this issue is to be investigated further. Recommdations for this type of testing are discussed in Chapter 12.

8.4.3 Force Analysis

The 200 mm/s test is the slowest test in which shim displacement is detected. This test will be used to obtain a quasi-static shim stiffness to use in the analytical damper model. However, the stiffness was also calculated from the 300 mm/s test for comparison. The total force on the shim must be determined in order to derive the shim stiffness. The shim force can be derived as

$$F_{total} = \rho \frac{q^2}{A_f n} + (p_1 - p_2) A_f n. \tag{8.1}$$

NOTE: See Chapter 3 for descriptions of each parameter.

The stiffness can then be determined as

$$k = \frac{\partial F_{total}}{\partial d} \tag{8.2}$$

where d is the experimentally determined shim displacement. Figures 8.32 and 8.33 show the relationship between total shim force and shim displacement for each test. The shim stiffness is equal to the slope of the linear regression line. Table 8.1 shows the stiffness obtained and compares it to the stiffness obtained in the mechanical loading tests. There is a 97% difference between these two stiffness values.

The discrepancy between the two stiffness values is not as surprising as it might seem. There are three factors that should be noted would have contributed to this disagreement. The first is the load range. Due to the nature of the mechanical stiffness test, the shims had to be loaded to at least 50 pounds before any displacement was

observed. During the fluid stiffness test the force only reached 3 pounds during the 200 mm/s peak speed test. Another factor is that the loading pattern is much different for the two tests. The loading in the mechanical test was concentrated to a point while the loading in the fluid test was likely distributed over a greater area. Lastly, the mechanical stiffness test was a static test while the fluid stiffness test was dynamic. It is very clear from the fluid stiffness testing that the valve and shims are a time dependent system. Results from this test would certainly be affected by the time dependency of the system and would therefore not match the results from a static test.
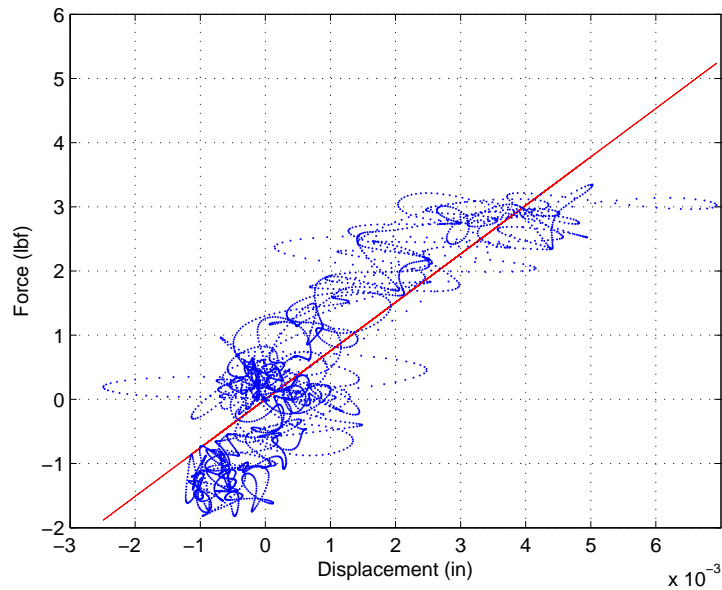
Figure 8.32: Total force on shim vs. shim displacement for 200 mm/s peak speed test.
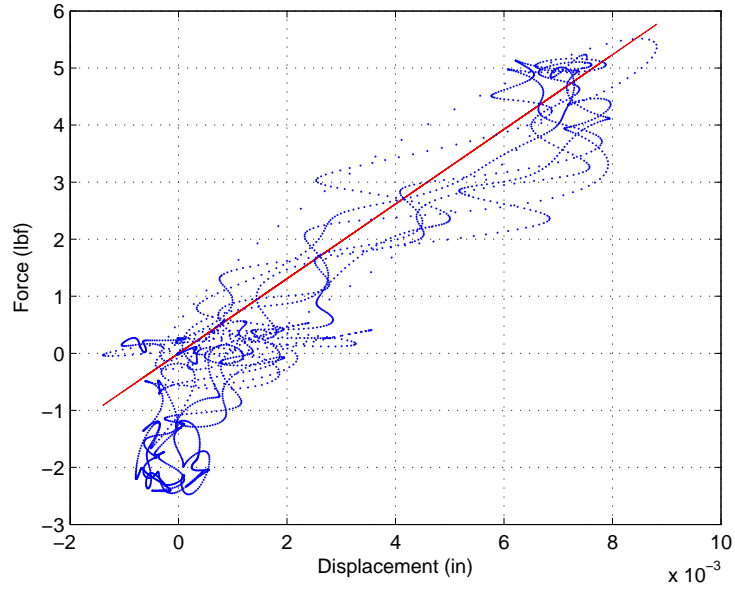
Figure 8.33: Total force on shim vs. shim displacement for 300 mm/s peak speed test.

Method	Stiffness (lbf/in)	Percent Difference (%)
Mechanical Loading	27355.6	–
Fluid Loading (200 mm/s)	778.63	97.24
Fluid Loading (300 mm/s)	696.97	97.45

Table 8.1: Shim stiffness values obtained by mechanical and fluid loading

Chapter 9: VALVE RESISTANCE - COMPUTATIONAL VALVE CHARACTERIZATION

A computational fluid dynamics model was developed in COMSOL for the purpose of studying the dynamics of the piston valve. Rather than simulating the fluid structure interaction this model used a static geometry. A parameter sweep was used to study the dynamics of the fluid for various shim deflections. This study was used to check the validity of Equations (3.11) through (3.14) which define the force applied to the shim from static pressure and from the change in fluid inertia. This study was also used to determine the relationship between pressure and flow through the valve for a given shim displacement. This relationship was then compared to the relationship defined by Equations (3.6) and (3.7) and the assumed dynamic discharge coefficients.

9.1 Simulation Setup

This study was done using a three dimensional geometry. The geometry was symmetrical about two axes. For this reason only one quarter of the geometry was modeled with symmetry boundary conditions applied. The geometry is shown in Figure 9.1 with the boudaries of symmetry highlighted. It should be noted that only the dynamics of the fluid are simulated in the study meaning that the geometry is

static. Therefore only the geometry of the fluid domain is modeled and the geometry of the solid domain is represented by empty space.
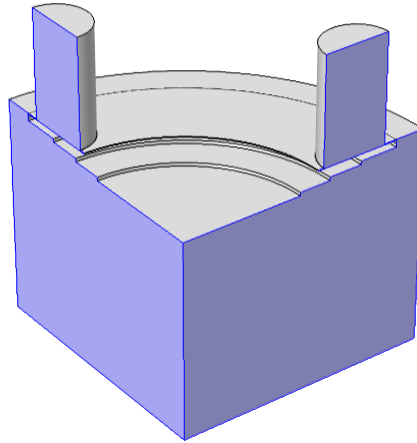
Figure 9.1: CFD Model Geometry

The top and bottom boundaries were designated as inlets and outlets respectively. The inlet boundaries are highligted in Figure 9.2 and the outlet boundaries are highlighted in Figure 9.3. The outlet pressure was set to 0 and the inlet pressure was swept from 10 psi to 150 psi in increments of 10 psi. The displacement of the shims was swept from .001" to .009" in increments of .001".

The model was probed at several points to acquire the desired data. The flow rate could be determined by probing the outlet boundary for flow. In order to determine shim force a circular boundary was created directly below the valve body orifice with a diameter equal to that of the valve body orifice. This boundary is highlighted in
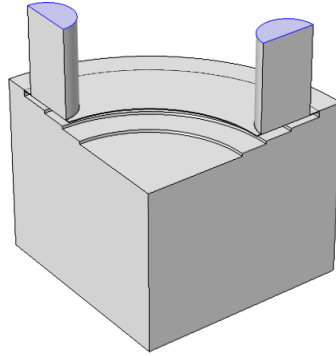
Figure 9.2: CFD Model Inlet Boundaries

Figures 9.4 and 9.5. The pressure on this boundary was integrated to determine the force on this region of the shim's surface. Force on other regions of the shim surface was assumed to be negligible. See Appendix D for additional screen shots of the model.
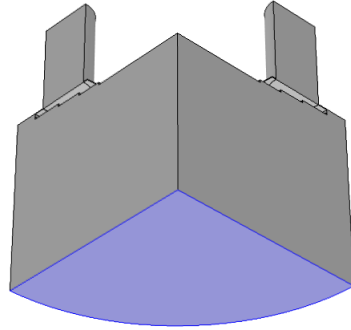
Figure 9.3: CFD Model Out Boundaries
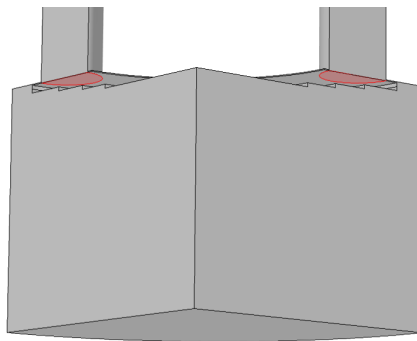
Figure 9.4: Force Probe Area
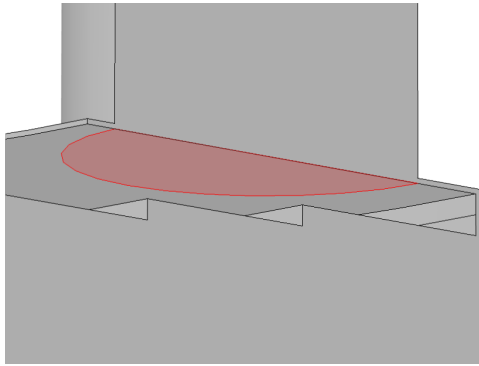
Figure 9.5: Force Probe Area Zoomed

9.2   Mesh Convergence

The model used tetrahedral elements to mesh the majority of the geometry. Triangular prism elements were used to mesh the boundary layers. A mesh convergence study was conducted to determine an appropriate mesh size. A coarse mesh was generated and the model was probed at the outlet for volumetric flow rate. The model was then refined several times. Figure 9.6 shows the effect of mesh size on the probed flow rate value. No significant change in the probed flow occurred after the mesh had
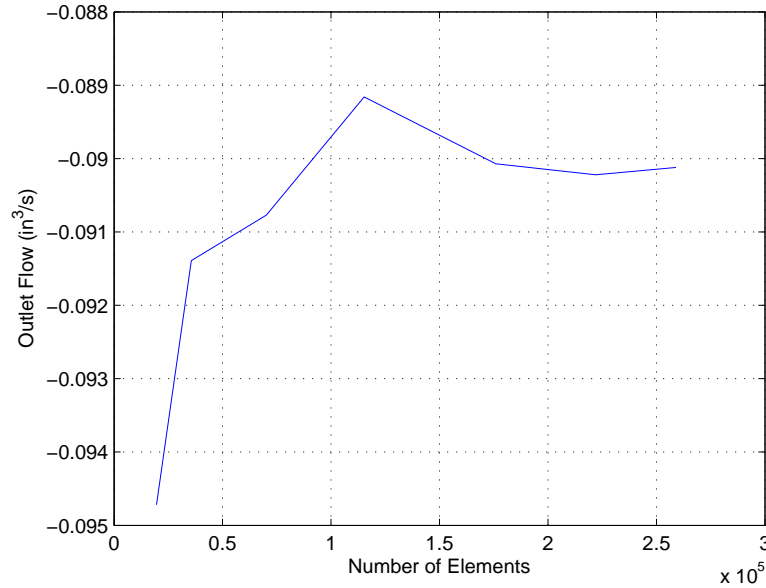
Figure 9.6: CFD Model Mesh Convergence

approximately 175,000 elements therefore a mesh with 179,306 elements was used. A screen shot of the meshed model is shown in Figure 9.7.
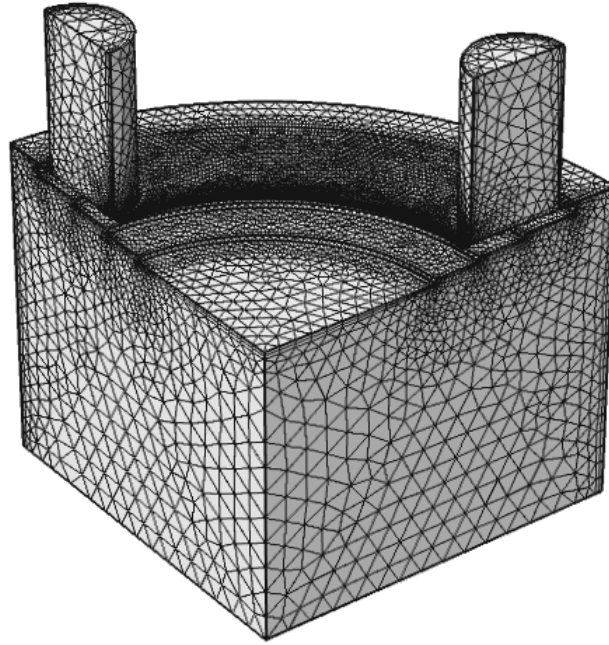
Figure 9.7: Meshed CFD Model

9.3 Results

The results of this simulation were used to study the force on the shim as well as the flow through the valve. Both studies are described in this section.

9.3.1 Force Analysis

The results show that the force on the shim, which originally was obtained by integrating the pressure just below the orifice, was slightly less than the theoretical prediction from (3.13) and (3.14). This can be seen in Figure 9.8. However, the

simulation results also show that the loading pattern on the shim is not as simple as was assumed when developing the damper model equations. Figure 9.9 shows that the high pressure area on the shim's surface extends well beyond the area beneath the orifice. This means that integrating only the pressure beneath the orifice will not give an accurate value for the force on the shim. The simulation was run again with the pressure integrated over a larger surface of the shim. This surface is highlighted in Figure 9.10. The resulting force is much larger than the theoretical force. This is shown in Figure 9.11. It should be noted that this does not necessarily implicate that the theoretical relationship between force and pressure should be changed in the model. The model attempts to calculate displacement by dividing an effective load by an effective stiffness. The effective load can be measured in any way as long as the relationship

$$F_{eq} = k_{eq}d \qquad (9.1)$$

holds true. These results do challenge the validity of the assumed loading pattern used to obtain this effective stiffness in Chapter 9. However, changing the force (F_{eq}) would necessitate a new stiffness (k_{eq}). This would require a new mechanical stiffness test to be conducted, one which would more accurately imitate the actual loading pattern of the shim. This is discussed more in Chapter 12.

9.3.2 Flow Analysis

The results of the flow analysis were not as expected. It can be seen in Figure 9.12 that the simulation flow rates do not match well with the theoretical flow rates given by Equation 3.7. Not only are the magnitudes different, but the shape of the curves is also very differnt. The results of this model were used to define a new relationship
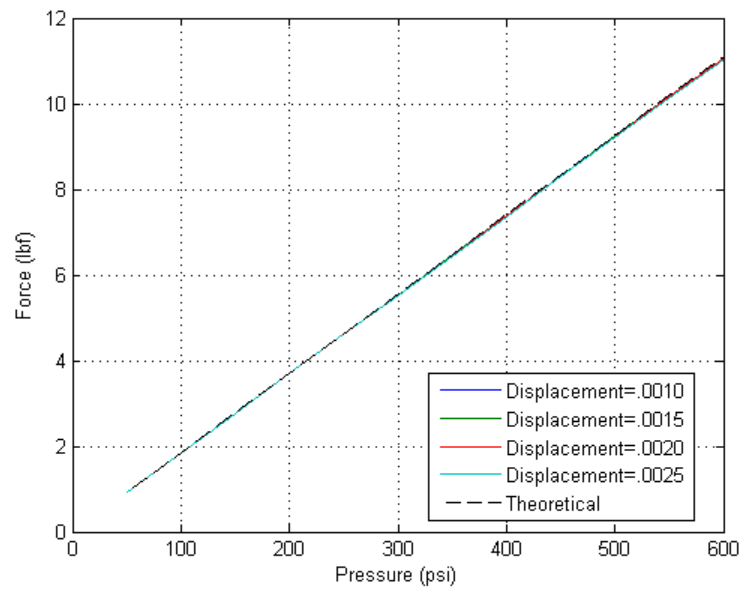
Figure 9.8: Relationship between shim force and pressure for various shim displacements.
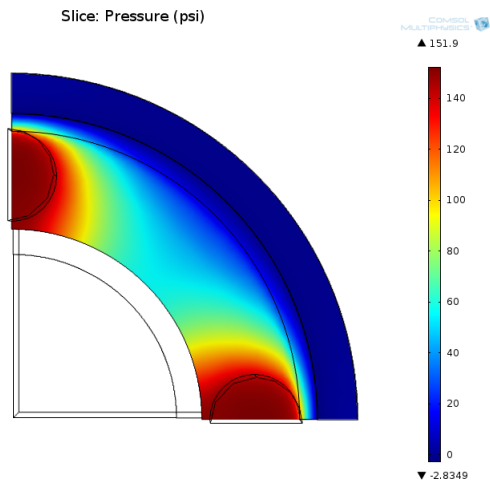
Figure 9.9: Shim pressure profile

93
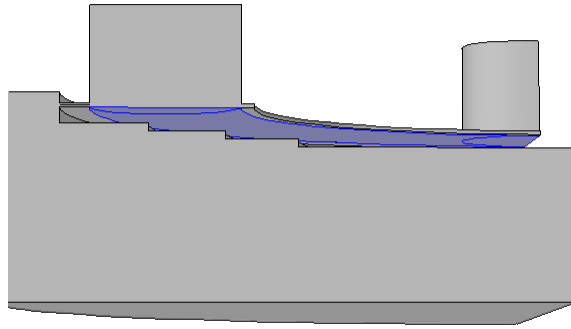
Figure 9.10: Modified force probe area
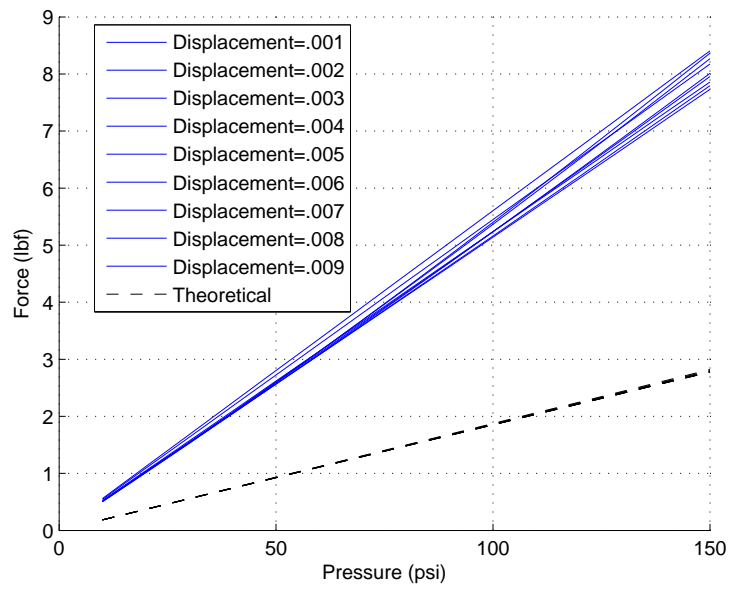
Figure 9.11: Relationship between shim force and pressure for various shim displacements using modified force probe area.

94

between flow and pressure for a given shim displacement. This was done by fitting an equation to the simulation data. The resulting equation assumes a second order relationship between flow and pressure that varies with shim displacement. This relationship is given by

$$Q = (a_1 d^4 + a_2 d^3 + a_3 d^2) * p^2 + (b_1 d^4 + b_2 d^3 + b_3 d^2) * p \qquad (9.2)$$

where

$$\begin{bmatrix} a_1 \\ a_2 \\ a_3 \end{bmatrix} = \begin{bmatrix} 6.7 \times 10^3 \\ -1.5 \times 10^2 \\ 7.9 \times 10^{-2} \end{bmatrix}$$

and

$$\begin{bmatrix} b_1 \\ b_2 \\ b_3 \end{bmatrix} = \begin{bmatrix} -1.4 \times 10^6 \\ 2.8 \times 10^4 \\ 1.7 \times 10^2 \end{bmatrix}.$$

This equation was used in the model to relate flow and pressure.
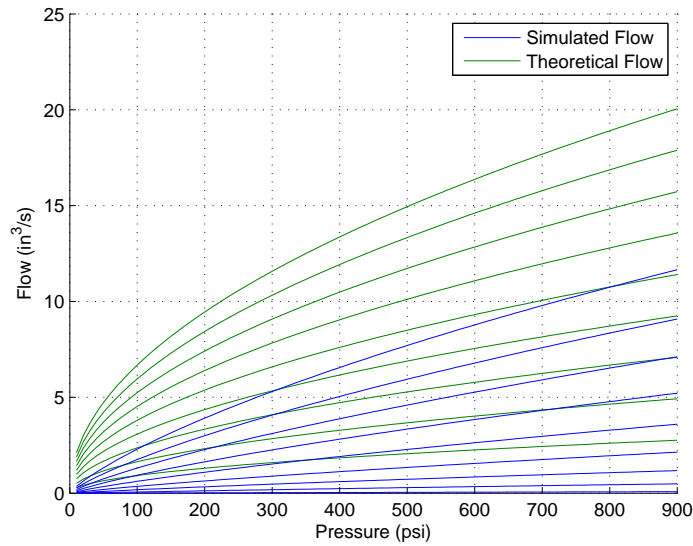
Figure 9.12: Theoretical and simulated relationship between flow and pressure for various gap sizes

9.4 Summary of Valve Studies

The damper valves were studied in much greater detail than any of the other parts of the damper. This is because the valves are the most complicated part of the damper, but also because the valves have the greatest effect on the overall force output of the damper. The shim stiffness, the most important parameter of the valves, was studied in a mechanical and a fluid test. The mechanical test involved application of a static force to the shims using a fork designed to apply a loading pattern similar to the actual loading pattern felt by the shim inside the damper. The fluid test involved measuring the displacement of the shims whlie fluid was flowing through the valve at dynamic rates. These two tests produced extremely different results. The displacements measured in the fluid test were much higher than would have been predicted by the stiffness values obtained from the mechanical stiffness test. To investigate this discrepancy a computational model was developed to study the flow and force applied to the shims. The results of this showed that the loading pattern was much different than was assumed when designing the loading forks for the mechanical shim test. Furthermore, the simulated relationship between flow and pressure contradicted the theoretical orifice flow prediction. This new pressure-flow relationship as well as the pressure-displacement relationship from the fluid shim test were quantified for use in the damper model.

The discrepancies seen in the results of the various valve studies are not as inordinate as they might seem. The conditions to which the shims are subjected in the mechanical tests are highly dissimilar from that of the fluid tests. The shims would not be effected by dynamics in the mechanical tests as they would in the fluid tests. Also, the loading patterns are much different between the two tests. In addition to

these, there are several assumptions that are made in order to compare the results of the two studies. These include the magnitude of the force, the static pressure across the shim and the degree to which the momentum of the fluid changes when flowing through the valve. It should be assumed that the results of the fluid test better characterize the actual valve. However, this does not necessarily mean that the stiffness value obtained in this test will yield higher model accuracy than the value obtained from the mechanical stiffness tests. This is discussed in greater detail in Chapter 12.

Chapter 10: PARAMETERS DEFINED OR SCALED FOR MODEL ACCURACY

Several Parameters were determined experimentally with low reliability or were not clearly defined by theoretical or experimental methods. These values allowed for adjustment of the final model. They were defined or scaled to yield the lowest error between the model output and the experimental data. The parameters defined to fit the model were the dynamic discharge coefficients of the constant area bleed valves and the variable area shim valves. These values should be approximately 0.7 [4]. For this reason values near 0.7 that best fit the model to the experimental data were selected. These values are shown in Table 10.1.

The parameters that were scaled to fit the model are the initial pressure in the damper and the Coulomb friction force. The initial pressure of the damper was measured before each experimental damper test was run. However, the accuracy of the

Parameter	Value
Bleed Valve Dynamic Discharge Coefficient	0.6
Variable Area Valve Dynamic Discharge Coefficient	0.7

Table 10.1: Parameters Defined to Fit Model

Parameter	Scalar
Initial Pressure	0.87
Coulomb Friction	1.05

Table 10.2: Parameters Scaled to Fit Model

sensors leaves an error of $\pm$ 20 psi allowing room for adjustment of this parameter. As described in Chapter 5, the Coulomb friction force value may contain some significant error. Thus the Coulomb friction value was adjusted slightly. The scalars applied to these two parameters are shown in Table 10.2.

Chapter 11: EXPERIMENTAL VALIDATION

The model was validated using the experimental stiffness values from the mechanical stiffness test and from the fluid stiffness test. When the stiffness values from the mechanical stiffness test were used, the orifice flow equations were used to govern flow through the valve. When the stiffness values from the fluid stiffness test were used, the empirical relationship defined by Equation (9.2) developed in Chapter 9 is used to govern the flow through the valve.

11.1 Mechanical Stiffness and Orifice Flow Equations

The figures in this section show the experimental force velocity relationship compared to the force-velocity relationship calculated by the model using the orifice flow equations and mechanical stiffness values. The force-displacement relationships are shown in Appendix E.
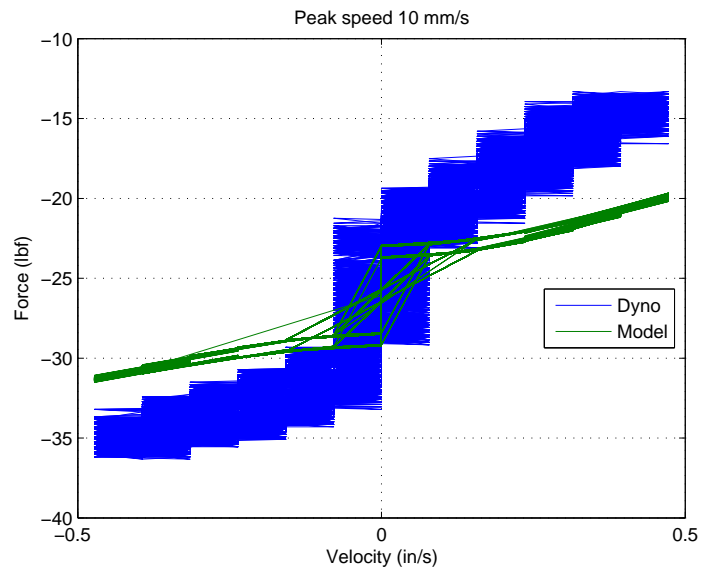
Figure 11.1: Experimental validation of 10 mm/s peak speed test using traditional orifice flow equations and mechanical stiffenss values
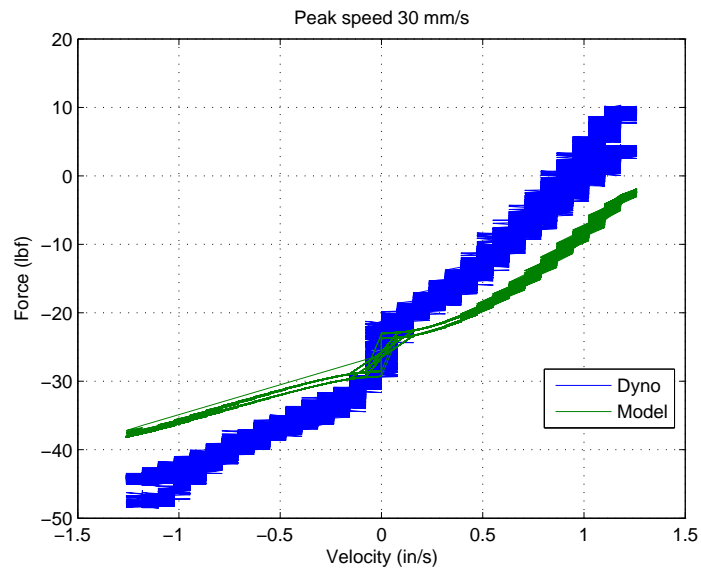
Figure 11.2: Experimental validation of 30 mm/s peak speed test using traditional orifice flow equations and mechanical stiffenss values
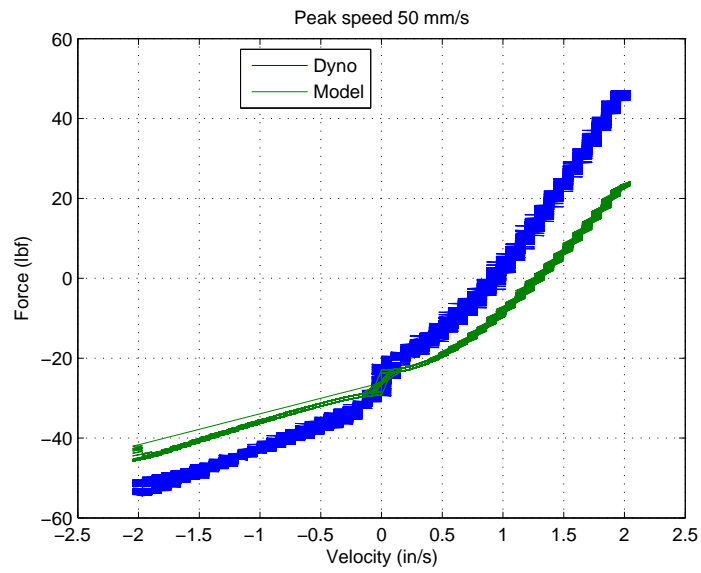
Figure 11.3: Experimental validation of 50 mm/s peak speed test using traditional orifice flow equations and mechanical stiffenss values
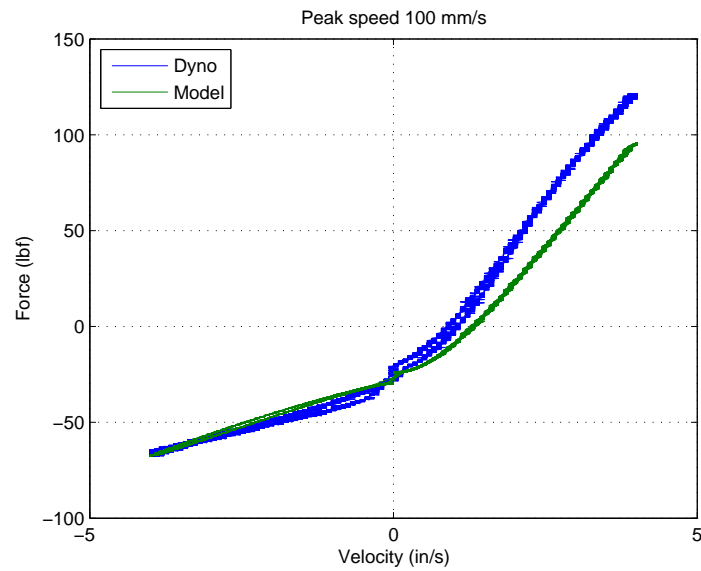
Figure 11.4: Experimental validation of 100 mm/s peak speed test using traditional orifice flow equations and mechanical stiffenss values
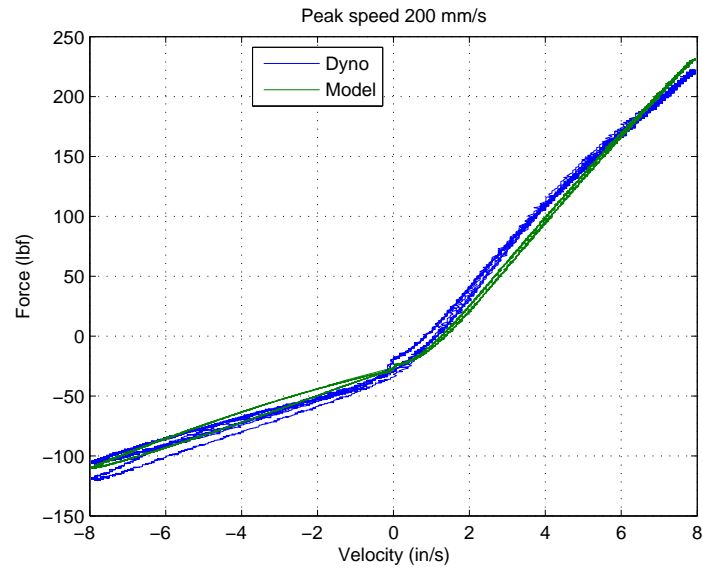
Figure 11.5: Experimental validation of 200 mm/s peak speed test using traditional orifice flow equations and mechanical stiffenss values
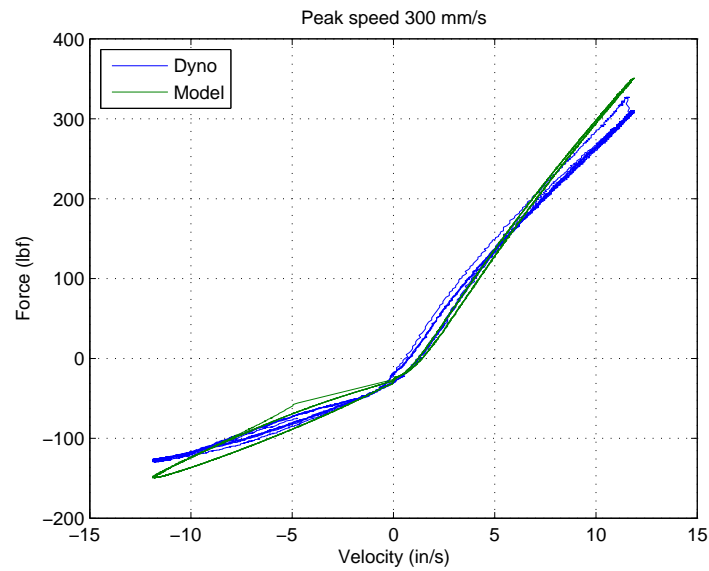
Figure 11.6: Experimental validation of 300 mm/s peak speed test using traditional orifice flow equations and mechanical stiffenss values
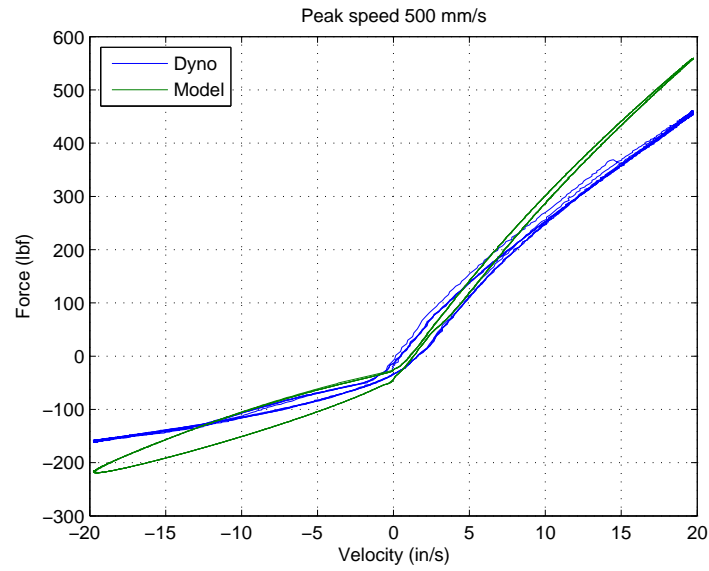
Figure 11.7: Experimental validation of 500 mm/s peak speed test using traditional orifice flow equations and mechanical stiffenss values
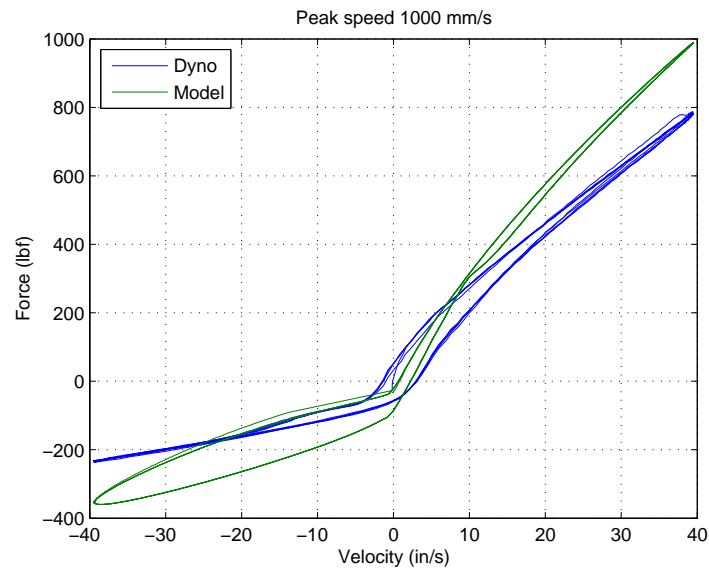
Figure 11.8: Experimental validation of 1000 mm/s peak speed test using traditional orifice flow equations and mechanical stiffenss values

11.2 Fluid Stiffness Values

The figures in this section show the experimental force velocity relationship compared to the force-velocity relationship calculated by the model using the mechanical stiffness values and the orifice flow equations. The force-displacement relationships are shown in Appendix E.
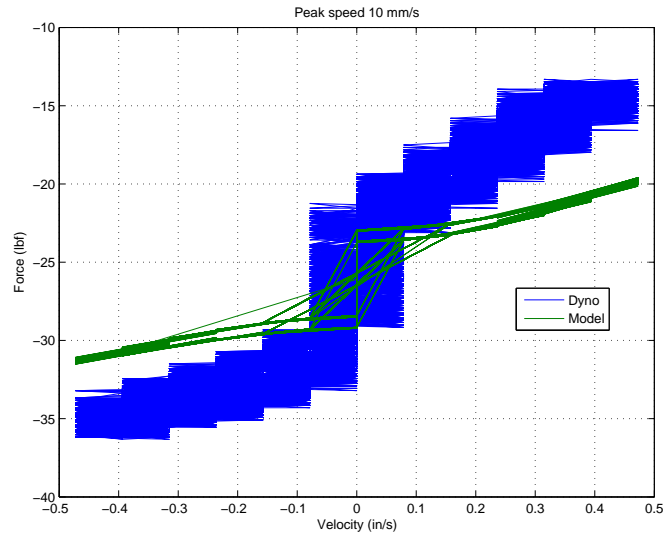
Figure 11.9: Experimental validation of 10 mm/s peak speed test using empirical flow equations and fluid stiffenss values
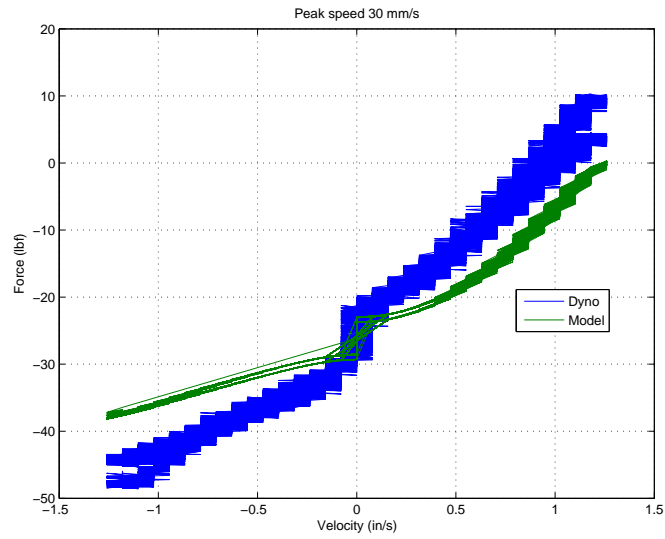
Figure 11.10: Experimental validation of 30 mm/ peak speed test using empirical flow equations and fluid stiffenss values
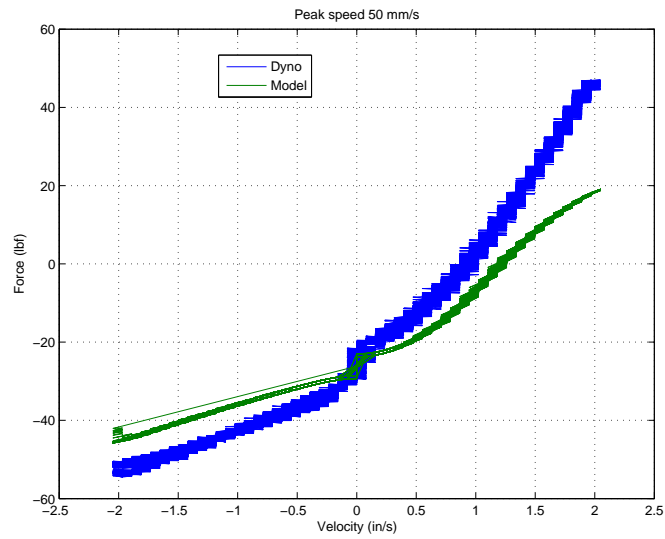
Figure 11.11: Experimental validation of 50 mm/s peak speed test using empirical flow equations and fluid stiffenss values
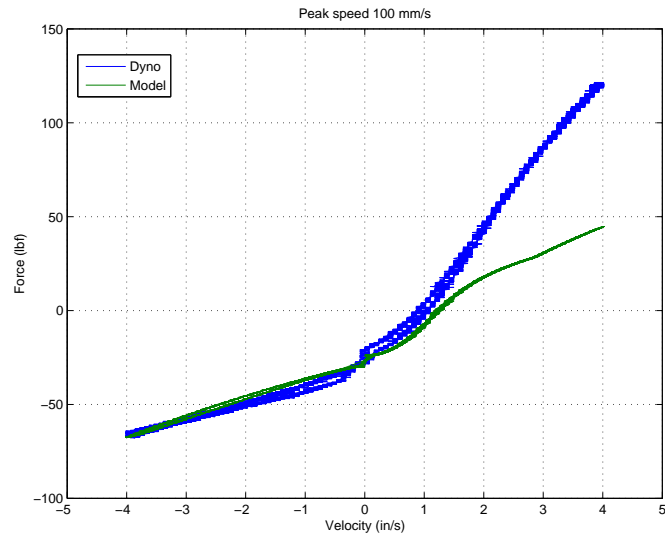
Figure 11.12: Experimental validation of 100 mm/s peak speed test using empirical flow equations and fluid stiffenss values
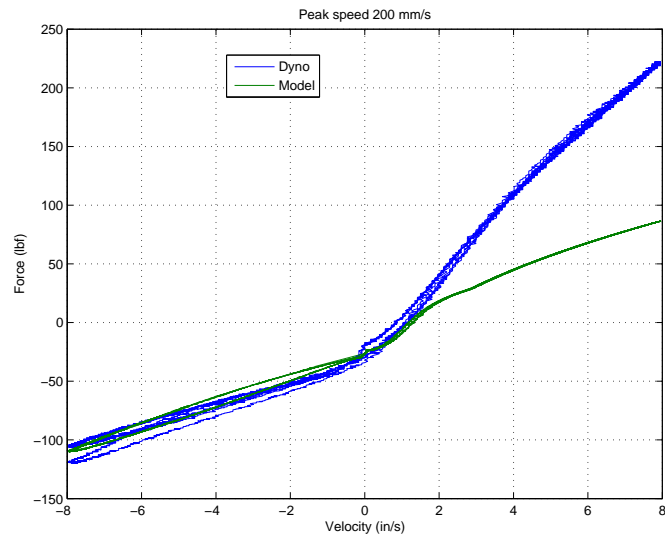
Figure 11.13: Experimental validation of 200 mm/s peak speed test using empirical flow equations and fluid stiffenss values
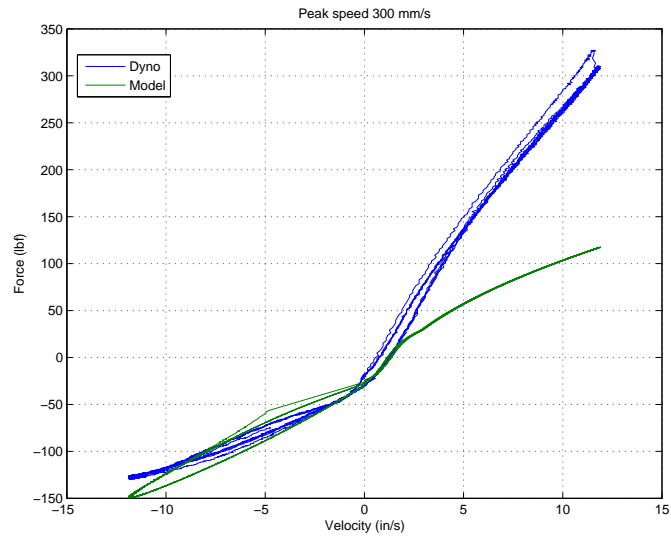
Figure 11.14: Experimental validation of 300 mm/s peak speed test using empirical flow equations and fluid stiffenss values
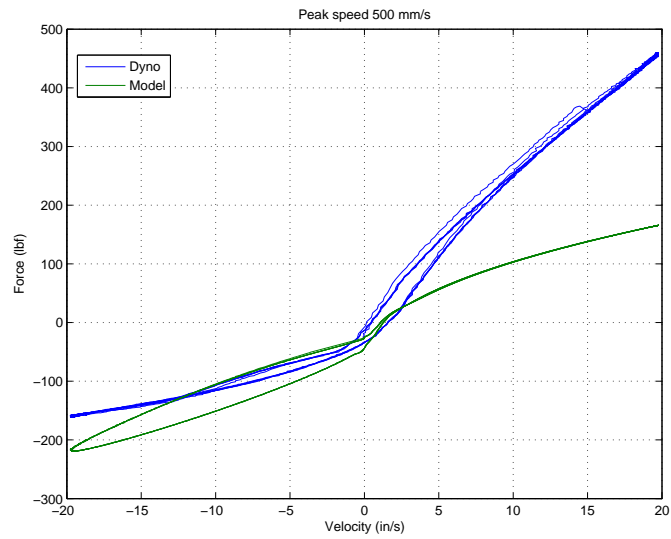
Figure 11.15: Experimental validation of 500 mm/s peak speed test using empirical flow equations and fluid stiffenss values
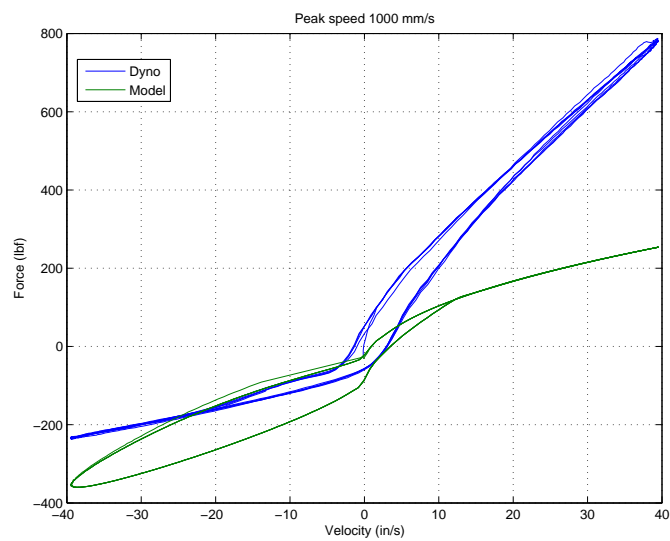
Figure 11.16: Experimental validation of 1000 mm/s peak speed test using empirical flow equations and fluid stiffenss values

Speed	Error Mech.	Error Fluid
(mm/s)	%	%
10	11.9	12.1
30	14.9	14.0
50	22.1	24.1
100	13.1	30.0
200	3.5	29.9
300	6.2	29.6
500	12.3	32.3
1000	15.9	35.0

Table 11.1: Model error by peak speed when mechanical stiffness values are used and when fluid stiffness values are used

11.3 Conclusions

It is clear from the results given in this chapter that the model produces a more accurate output when the mechanical stiffness values and the orifice flow equations are used. This result is somewhat surprising considering the methods used for obtaining the fluid stiffness values and the empirical flow equations involved much fewer assumptions. In order to understand how mechanical stiffness values and orifice flow equations could make this model more accurate it is important to consider the process through which this type of model has been developed.

This type of damper model has been developing for decades. An early appearance in the literature is in Harold Lang's 1977 dissertation [4]. Many assumptions were made when this model was developed and more have been made to refine it. Most of these assumptions were made with no validation other than an apparent increase in the accuracy of the damping force output by the model. Researchers could not

have considered the accuracy of subsystem outputs, such as the displacement of the shims, because they did not have experimental data on such outputs. It is possible that several invalid assumptions worked together to produce a relatively accurate damping force output. Since no subsystem outputs were considered in the validation, there would be no reason to discard these invalid assumptions. Finally, since many of the assumptions involving shim stiffness made in previous research are consistent with the assumptions made when determining the shim stiffness values mechanically, it is not surprising that these values perform better than the fluid stiffness values.

The results shown in this chapter challenge the validity of this model. There are several equations whose accuracy should be evaluated in order to determine if they are appropriate for this model. These are

- Orifice flow equations

- Orifice area equations

- Equations for force applied to the shims

These equations involve many unproven assumptions. If these equations are to be used in this model they should each undergo an individual validation process. This is discussed more in the Chapter 12.

Chapter 12: SUMMARY AND CONCLUSIONS

The objectives of this project were to create an analytical damper model and evaluate the parameters of the model such that the damping force output could be experimentally validated with at least 80% accuracy. In order to do this five parameters had to be evaluated. These included gas bulk modulus, oil bulk modulus, Coulomb friction, effective mass and valve resistance. The shim stiffness parameter was to be evaluated using two different experiments. One in which a load is applied to the shims with steel forks that mimic actual loading pattern of the shims and one in which the displacement of the shims is measured as fluid is flowing through the valve.

The bulk modulus, Coulomb friction and effective mass were all determined experimentally using a damper dynamometer to apply dynamic or static displacements to the damper body while various measurements were taken. These measurements included pressure in each chamber, force at the top and bottom of the damper, and displacement, velocity and acceleration of the damper body. For the bulk modulus and the Coulomb friction tests the damper was reconfigured to allow for evaluation of these values.

The mechanical shim stiffness test was the first test done to characterize the stiffness of the valve shims. In this test a mechanical load was applied to the shims

with a steel fork designed to mimic the actual fluid loading on the shims. A unique fork was designed for each of the four check valves. During these tests, the compliance of the test fixtures was a significant part of the measurement. For this reason a similar test was run to determine the stiffness of the fixtures so that this could be accounted for when determining the shim stiffness.

A fluid shim stiffness test was also conducted in which the displacement of the shims was measured while fluid was flowing through the valve. These results did not match well with the results of the mechanical shim stiffness test. Much higher displacements were measured in the fluid test than would have been predicted by the stiffness obtained in the mechanical testing. When the model was validated experimentally, it achieved much higher accuracy when the mechanical stiffness was used. This discrepancy is evidence that, although the model produces a relatively accurate output, it is not accurately characterizing the valve subsystem.

12.1 Major Contributions

This project contributed several innovations that were not prevalent in scholarly literature before. These are

- A two degree of freedom analytical damper model

- An analytical damper model with minimal empirically determined parameters

- A study of the dynamics of damper check valves under fluid loading

In addition to these well defined contributions, this project has raised several questions that lead to new research that could be done to further investigate damper

dynamics. These questions and the work that should be done to address them are discussed in the future work section of this chapter.

12.2 Valve Characterization Discrepancies

It is clear from Chapter 11 that the model was much more accurate when stiffness values obtained in the mechanical stiffness test were used. This is not a surprising observation. Lumped parameter models similar to the one in this study have been researched for decades and have seen many developments and refinements; most of which are based on assumptions that fit the model to experimental data. In previous studies involving this type of model, static shim stiffnesses have been assumed. It is likely that these models have been developed in a way that accommodates these static stiffnesses. To put this simply: if an invalid assumption was made about the shim stiffness, then other parameters would have been inadvertently fine tuned to negate the effects of the original invalid assumption. In this model the equations governing flow through the valve are physically intuitive equations that are multiplied by a discharge coefficient. This discharge coefficient tunes the inaccurate physically intuitive equation to better match experimental data. These types of equations provide the mechanism by which a damper model can be tuned to output accurate results in spite of invalid assumptions. An attempt was made to eliminate these equations by determining a new flow equation from computational data. Even when used with these equations the stiffness values from the fluid shim stiffness test made the model inaccurate. However, the accuracy of the computational data used to determine this new flow equation is questionable because of several simplifying assumptions and a lack of any sort of validation.

It appears that the results of a dynamic shim stiffness test are not valuable to this type of model. This is not to say that the results of the fluid stiffness test have no value. This experiment has opened up several topics for further investigation which are discussed in the following section. The fluid stiffness test has also provided a basis for future similar experiments to build from. This document details the development of the fluid stiffness test including the issues that arose and the actions that were taken to troubleshoot these issues. This knowledge is valuable for continued research in this area.

12.3   Future Work

The fluid shim stiffness testing raised questions about the nature of the piston shim dynamics. It is clear that more information is needed about the shim dynamics if a more accurate damper model is to be developed. There are several studies that should be done to continue research on damper valve dynamics. One study that should be done is to experimentally determine the displacement profile of the entire surface of the shim while it is undergoing deformation from dynamic fluid loading. This would provide insight to two issues. One is the issue of positive shim deflection observed at negative pressure differentials discussed in Chapter 8. A measurement of the topography of the shim would be useful in determining why this phenomenon has been observed and how it effects the flow through the valve. Information on the topography of the shim would also help in determining a theoretical relationship between flow and pressure that is more accurate than the traditional orifice flow equations. An attempt to determine this relationship computationally was discussed in Chapter 9. However, this study was based on a simplified shim geometry that did

not account for the sloped profile of the valve shim. Knowledge of this profile could increase the accuracy of this computational model.

This leads to the next study recommended for future research: a more accurate computational model. The computational model used in this study could see improvements other than an accurate representation of the shim profile. A computational model that can simulate the fluid structure interaction would be extremely valuable. A fluid structure interaction model was attempted for this project. Unfortunately, several obstacles prevented the successful development of an accurate fluid structure interaction model of the damper valve. Mainly, the finite element method was not able to be used to compute the force at the boundaries between shims. These boundaries have shear forces due to friction in addition to normal forces. It is difficult to model this friction with finite element analysis and because of this, a computational model that calculates the response of the shims could not be developed.

Bibliography

[1] K. Balasubramanian. Smart bulk modulus sensor. Master's thesis, University of Florida, 2003.

[2] E.O. Doebelin. *System Dynamics: Modeling, Analysis, Simulation, Design.* Dekker, New York, 1998.

[3] S.W. Duym. System dynamics: Modeling, analysis, simulation, design. *Steering and Suspensions Technology*, pages 1223–1237, 1998.

[4] H.H. Lang. *A Study of the Characteristics of Automotive Hydraulic Dampers at High Stroking Frequencies.* PhD thesis, The University of Michigan, Ann Arbor, 1977.

[5] I. Lee and D. Sun. Evaluations of effective bulk modulus of oil in automotive hydraulic dampers-effects of cylinder shell elastic deformation. *SICE Annual Conference*, pages 2431–2436, 2004.

[6] M.R. Munson, D.F. Young, T.H. Okiishi, and W.W. Huebsch. *Fundamentals of Fluid Mechanics.* Don Fowley, sixth edition, 2009.

[7] W.J. Palm. *System Dynamics.* McGraw-Hill, second edition, 2010.

[8] K.S. Rhoades. Development and experimental verification of a parametric model of an automotive damper. Master's thesis, Texas A&M University, 2006.

[9] M. Shams, R. Ebrahimi, A. Raoufi, and B.J. Jafari. Cfd-fea analysis of hydraulic shock absorber valve behavior. *International Journal of Automotive Technology*, 8:615–622, 2007.

[10] M.S. Talbott and J. Starkey. An experimentally validated physical model of a high-performance mono-tube damper. *SICE Annual Conference*, page 382, 2002.

[11] T.E. Walters. Development of a smart material electrohydrostatic actuator considering rectification valve dynamics and in situ valve characterization. Master's thesis, The Ohio State University, 2008.

[12] W.C. Young and R.G. Budynas. *Roark's Formulas for Stress and Strain.* McGraw-Hill, seventh edition, 1989.

[13] J. Yu, Z. Chen, and Y. Lu. The variation of oil effective bulk modulus with pressure in hydraulic systems. *Journal of Dynamic Systems, Measurement, and Control*, 116:146–150, 1994.

Appendix A: CHAMBER 2 ANALYTICAL EQUATIONS
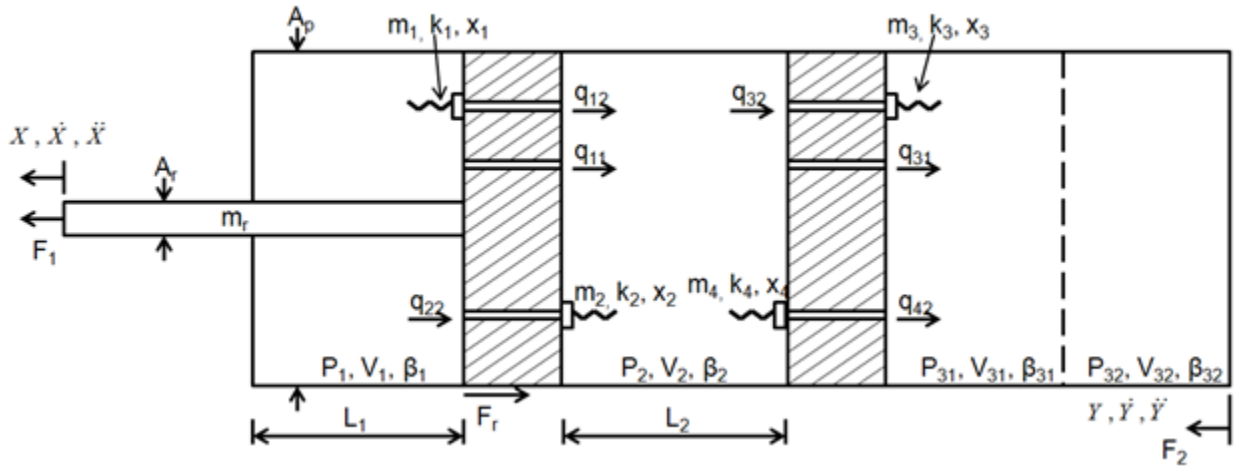
Figure A.1: Diagram of Analytical Damper Model

A.1   Chamber 2 Continuity Equation

$$q_{11} + q_{12} + q_{22} - q_{\beta 2} - q_{31} - q_{32} - q_{42} = \dot{Z}A_p \qquad \text{(A.1)}$$

A.2   Chamber 2 Orifice Flow Equations

$$q_{31} = n_{31} C_{d31} A_{A31} sgn(p_2 - p_3) \sqrt{\frac{2|p_2 - p_3|}{\rho}} \tag{A.2}$$

$$q_{32} = \begin{cases} 0 & p_3 \geq p_2 \\ C_{d32} A_{32} \sqrt{\frac{2|p_2-p_3|}{\rho}} & p_3 < p_2 \end{cases} \tag{A.3}$$

$$q_{42} = \begin{cases} 0 & p_3 \leq p_2 \\ -C_{d42} A_{42} \sqrt{\frac{2|p_2-p_3|}{\rho}} & p_3 > p_2 \end{cases} \tag{A.4}$$

A.3   Chamber 2 Fluid Compressibility Equations

$$q_{\beta 2} = \frac{(L_2 - Z)A_p}{\beta_2} \dot{p}_2 \tag{A.5}$$

where

$$\beta_2 = \beta_2(p_1)$$

A.4   Chamber 2 Orifice Area Equations

$$A_{32} = \pi D_{v32} x_3 \tag{A.6}$$

$$A_{42} = \pi D_{v42} x_4 \tag{A.7}$$

A.5   Chamber 2 Equations for Shim Displacement

$$F_{3\Delta p} = |p_2 - p_3| A_{f32} n_{32} \tag{A.8}$$

$$F_{3inertia} = \rho \frac{q_{32}^2}{A_{f32} n_{32}} \tag{A.9}$$

$$x_3 = \frac{F_{3\Delta p} + F_{3inertia}}{k_3} \tag{A.10}$$

$$F_{4\Delta p} = |p_3 - p_2| A_{f42} n_{42} \tag{A.11}$$

$$F_{4inertia} = \rho \frac{q_{42}^2}{A_{f42} n_{42}} \tag{A.12}$$

$$x_4 = \frac{F_{4\Delta p} + F_{4inertia}}{k_4} \tag{A.13}$$

Appendix B: RESULTS OF SECOND FLUID SHIM STIFFNESS TEST
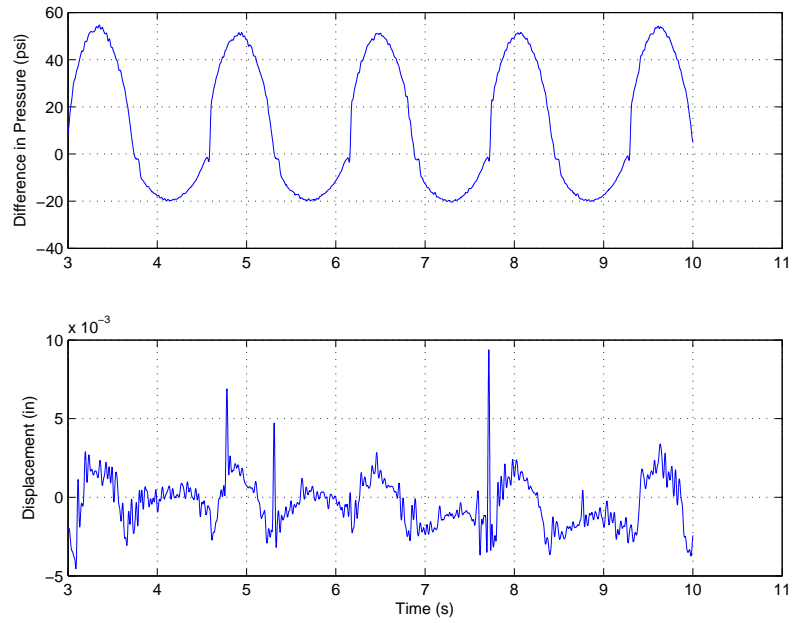
Figure B.1: Displacement and pressure over time for 100 mm/s peak piston speed
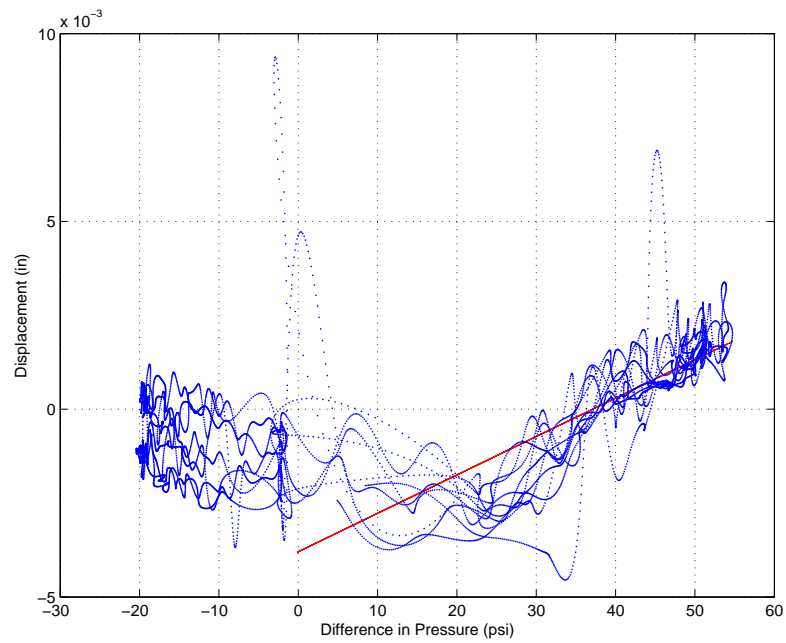
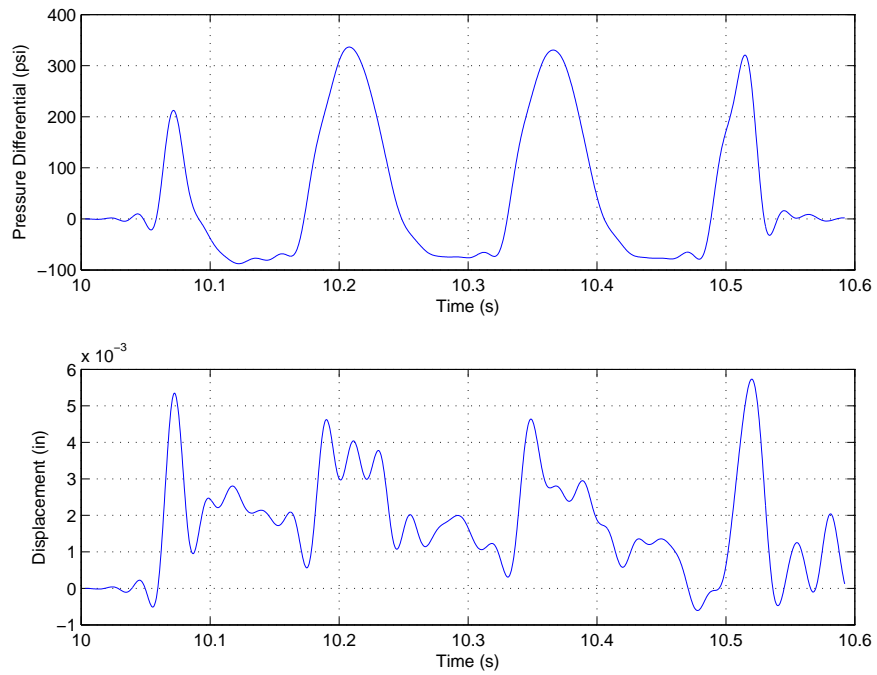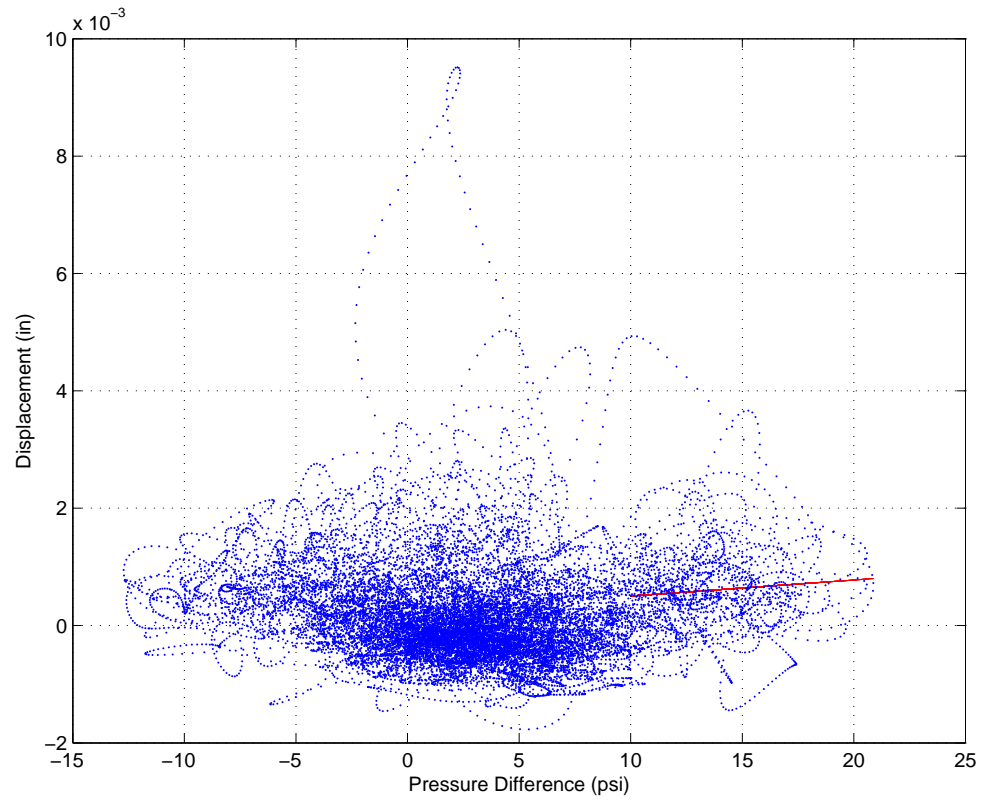Figure B.2: Displacement versus pressure for 100 mm/s peak piston speed

123
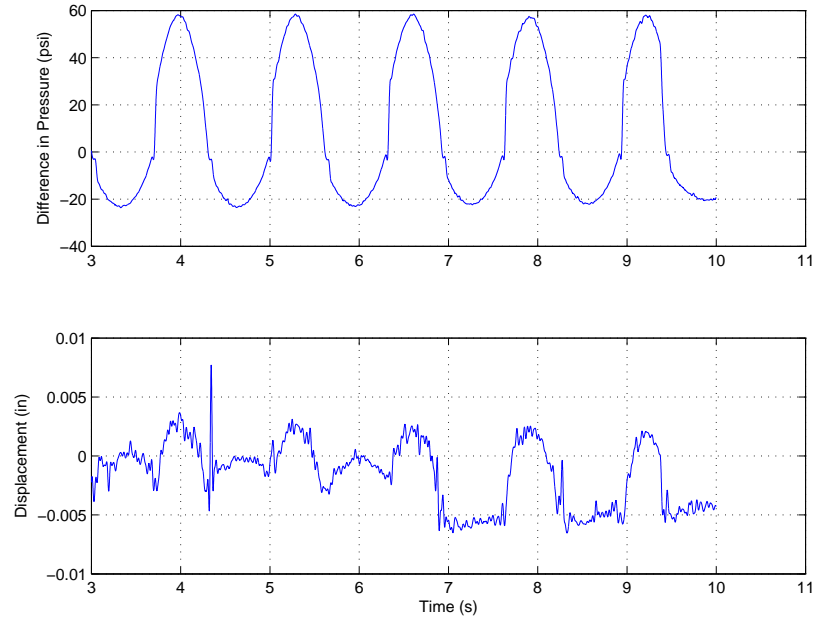
Figure B.3: Displacement and pressure over time for 120 mm/s peak piston speed
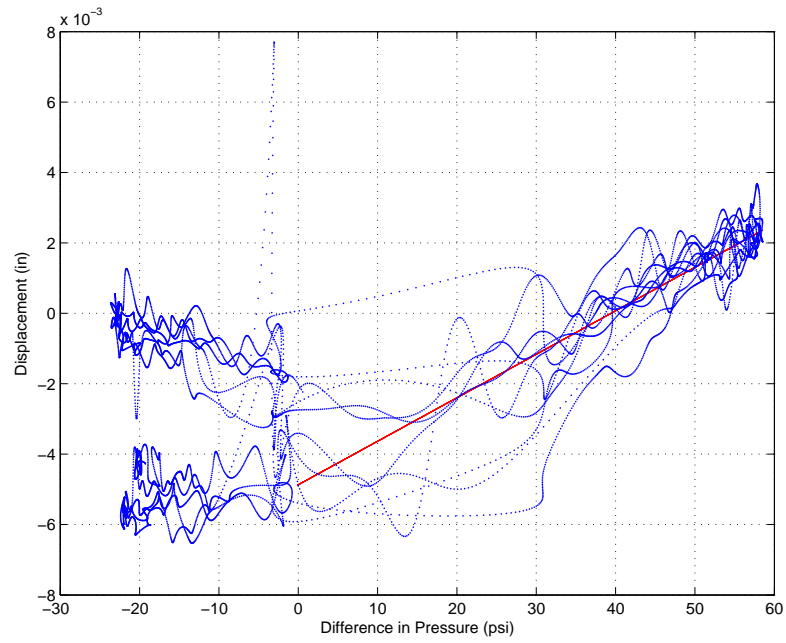
Figure B.4: Displacement versus pressure for 120 mm/s peak piston speed
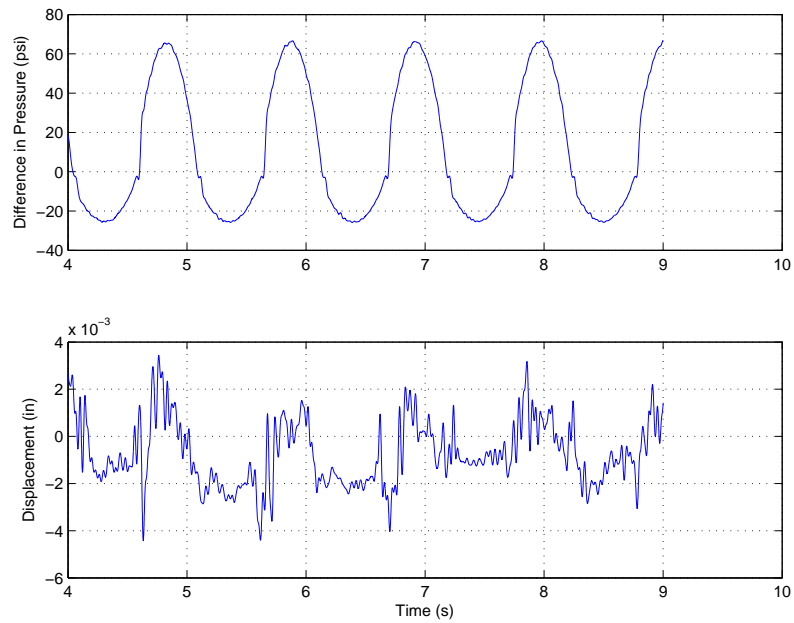
Figure B.5: Displacement and pressure over time for 150 mm/s peak piston speed
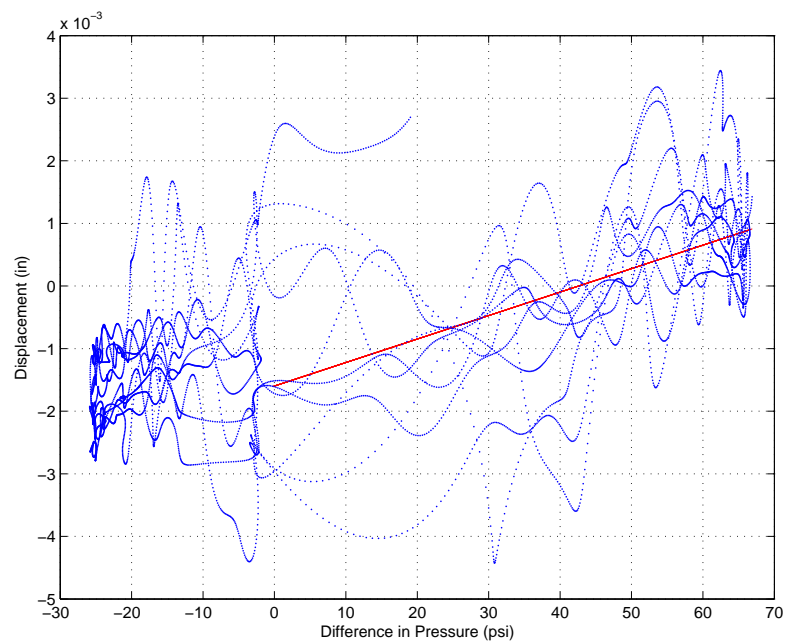
Figure B.6: Displacement versus pressure for 150 mm/s peak piston speed

125
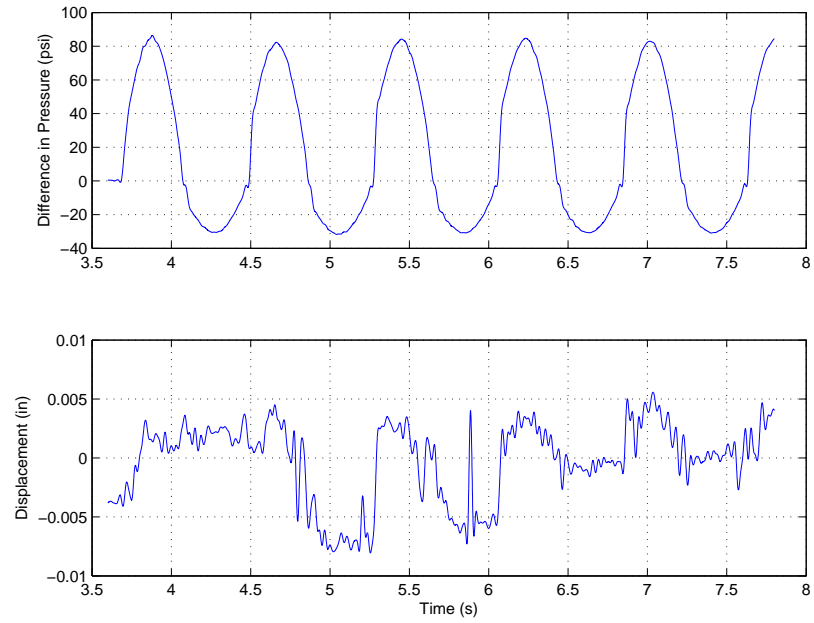
Figure B.7: Displacement and pressure over time for 200 mm/s peak piston speed
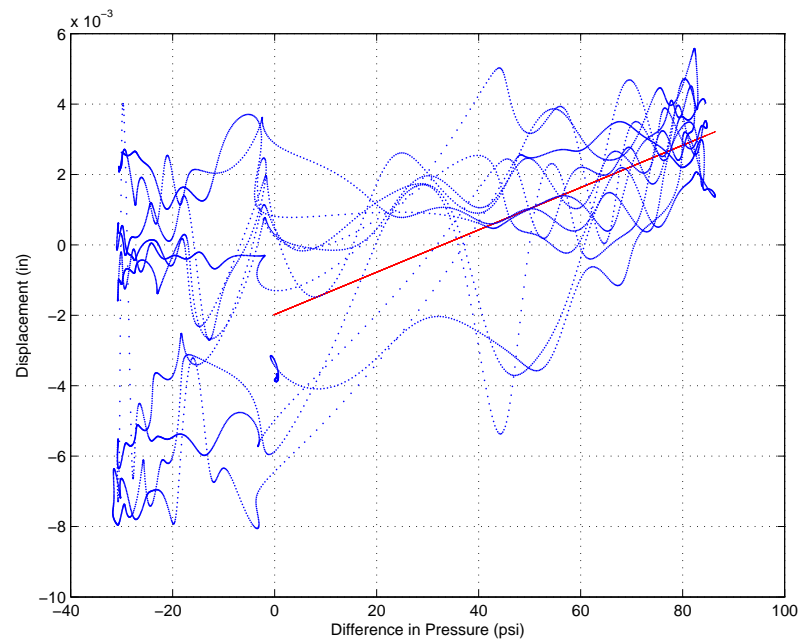
Figure B.8: Displacement versus pressure for 200 mm/s peak piston speed

126
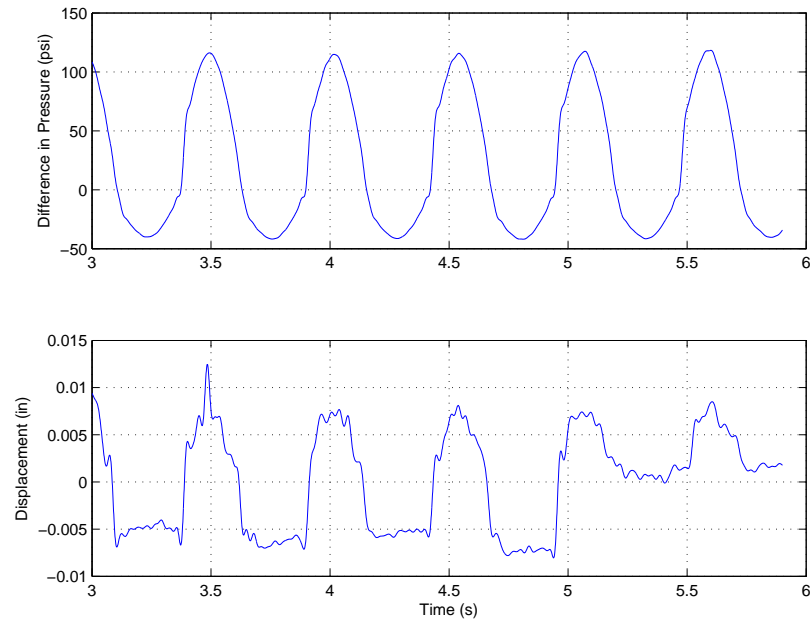
Figure B.9: Displacement and pressure over time for 300 mm/s peak piston speed
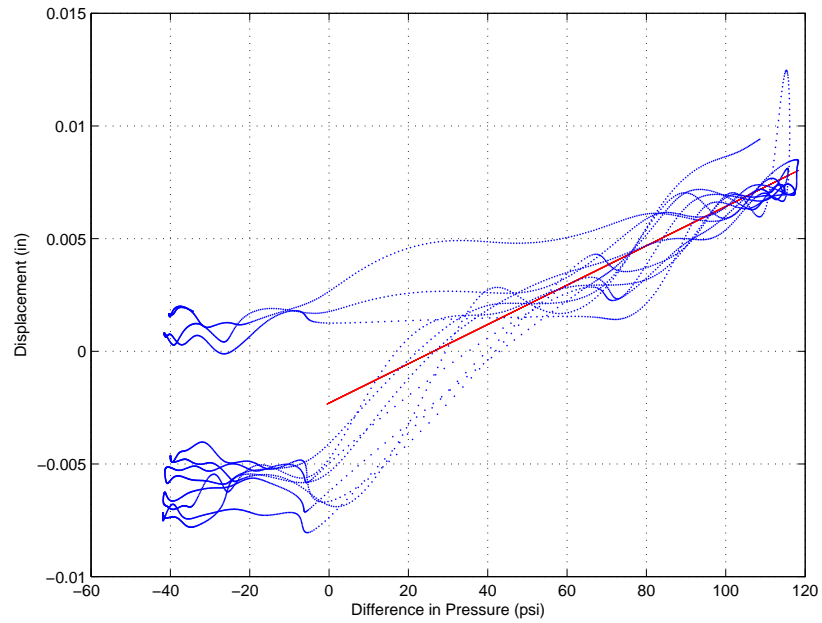
Figure B.10: Displacement versus pressure for 300 mm/s peak piston speed

127
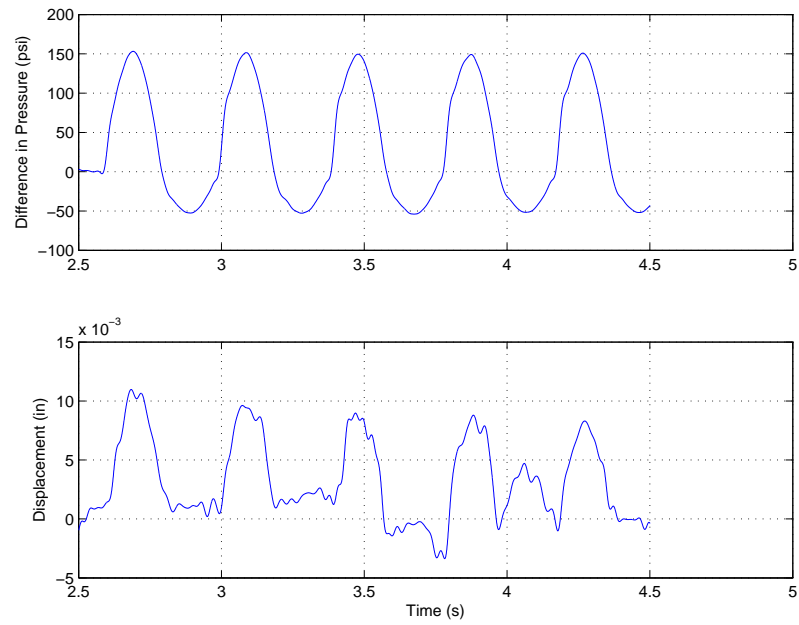
Figure B.11: Displacement and pressure over time for 400 mm/s peak piston speed
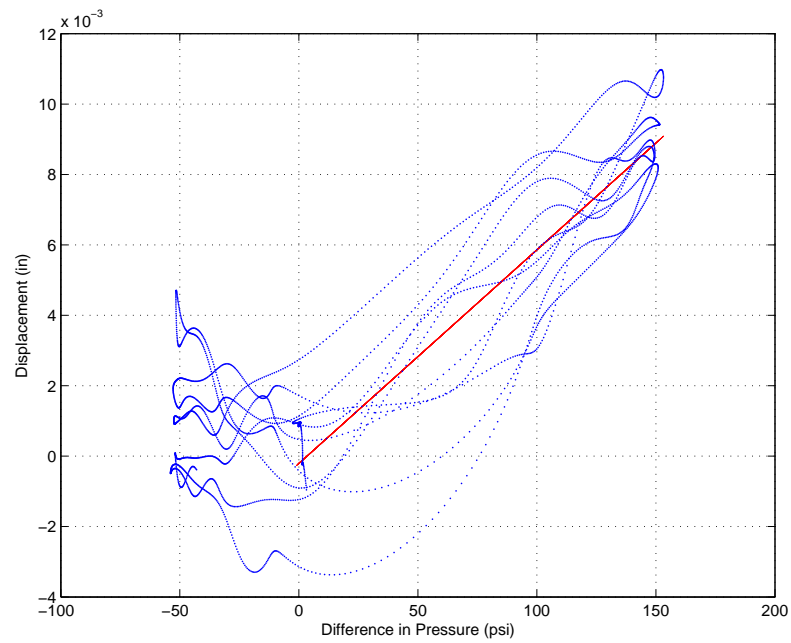
Figure B.12: Displacement versus pressure for 400 mm/s peak piston speed

Appendix C: RESULTS OF THIRD FLUID SHIM STIFFNESS TEST
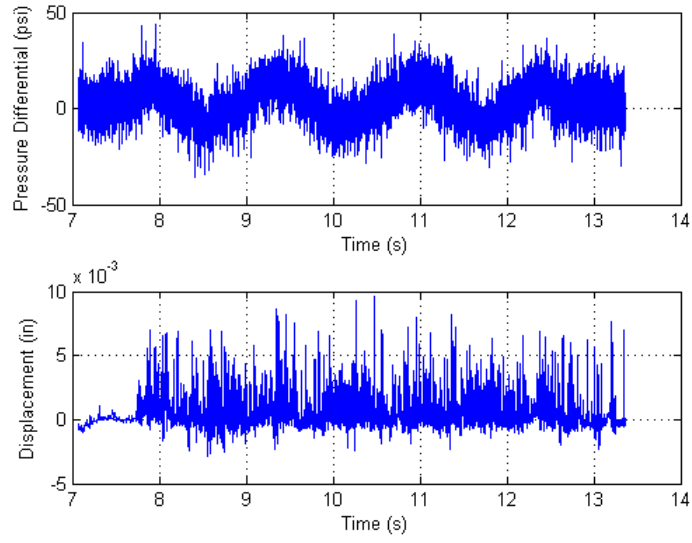
Figure C.1: Displacement and pressure over time for 100 mm/s peak piston speed
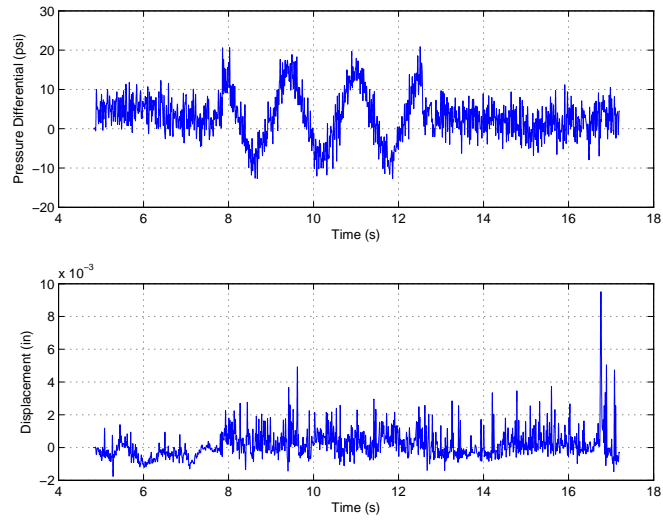
Figure C.2: Filtered displacement and pressure over time for 100 mm/s peak piston speed
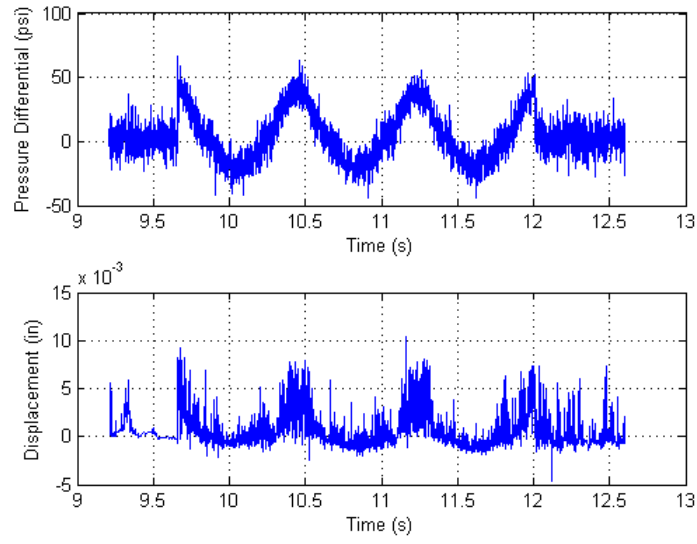
Figure C.3: Displacement and pressure over time for 200 mm/s peak piston speed
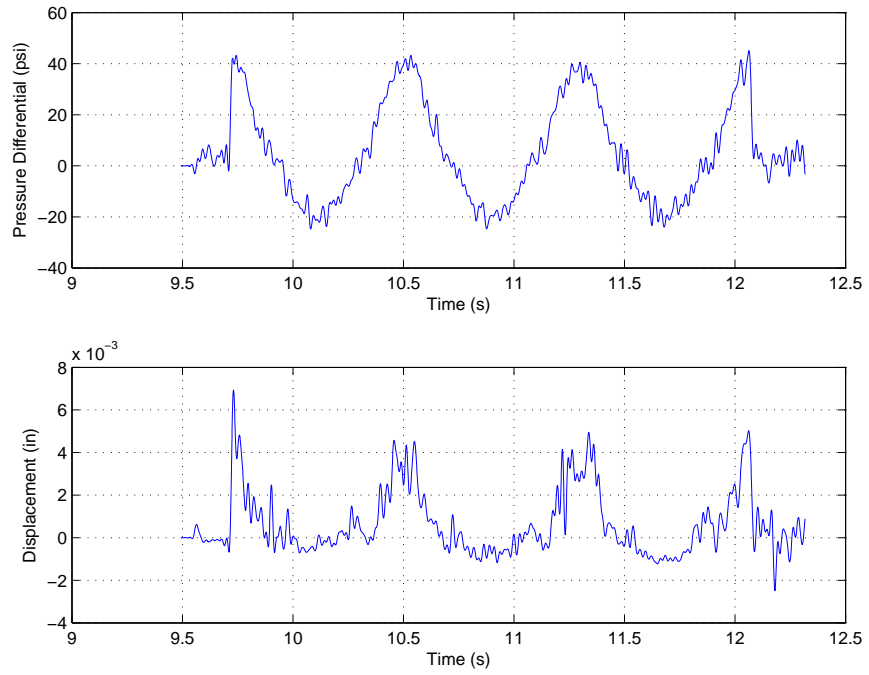
Figure C.4: Filtered displacement and pressure over time for 200 mm/s peak piston speed
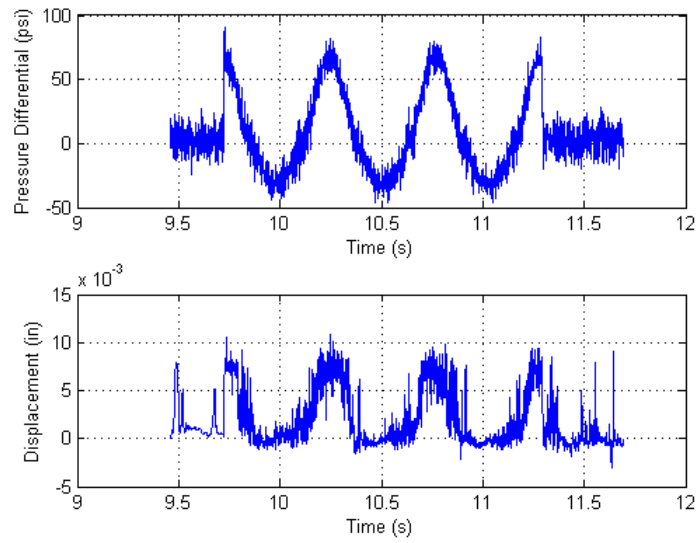
Figure C.5: Displacement and pressure over time for 300 mm/s peak piston speed
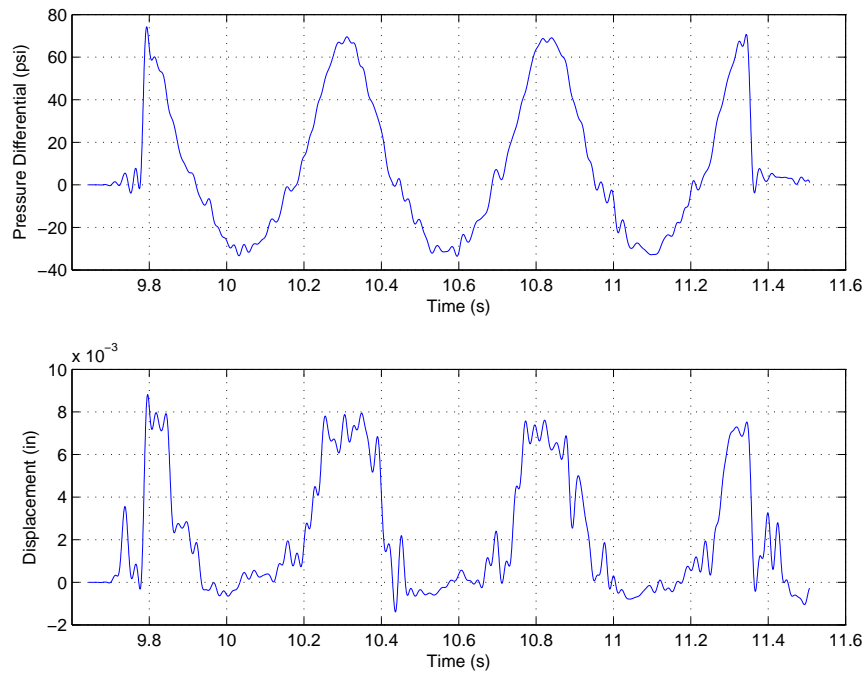
Figure C.6: Filtered displacement and pressure over time for 300 mm/s peak piston speed
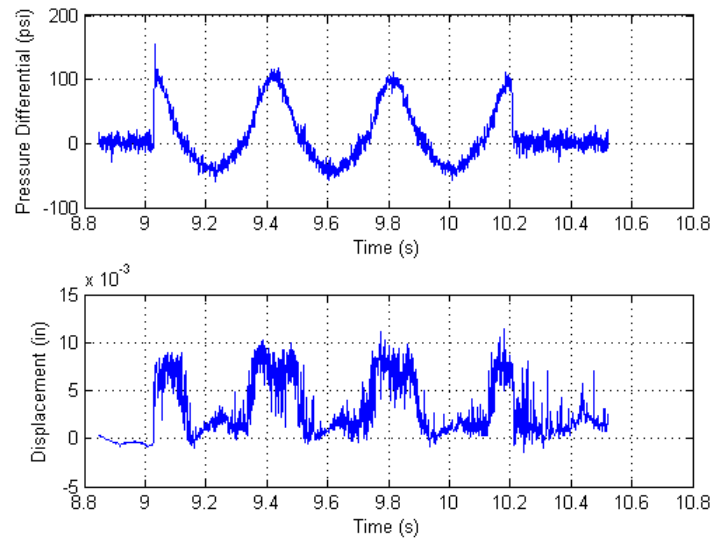
Figure C.7: Displacement and pressure over time for 400 mm/s peak piston speed
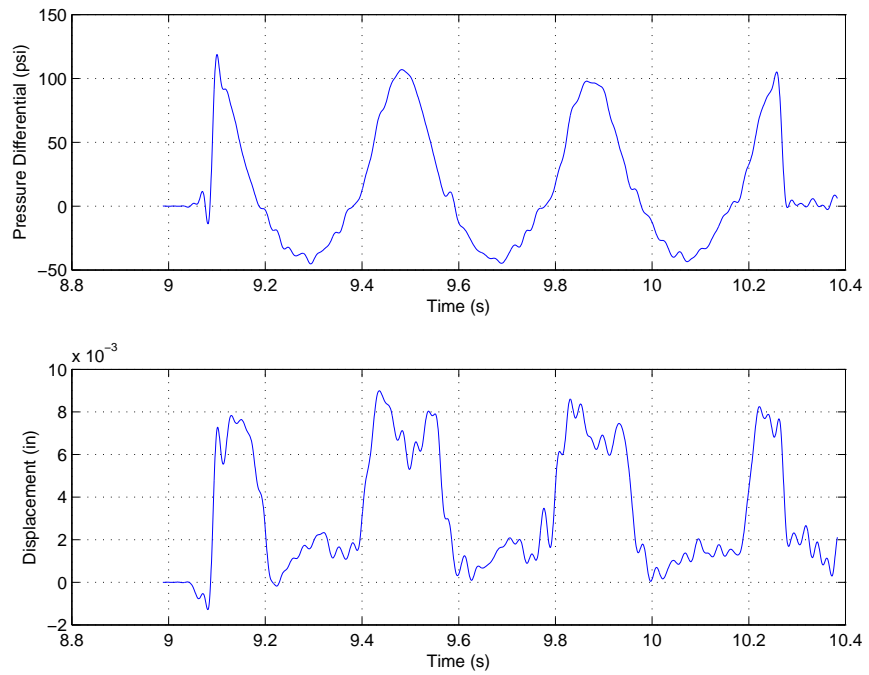
Figure C.8: Filtered displacement and pressure over time for 400 mm/s peak piston speed
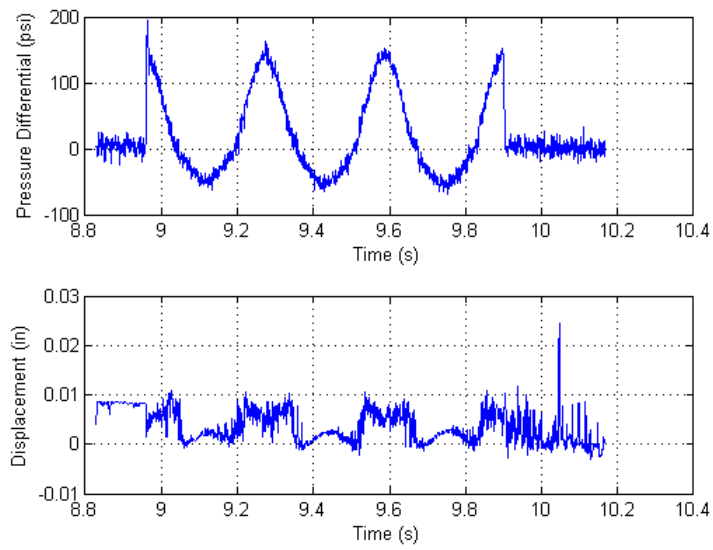
Figure C.9: Displacement and pressure over time for 500 mm/s peak piston speed
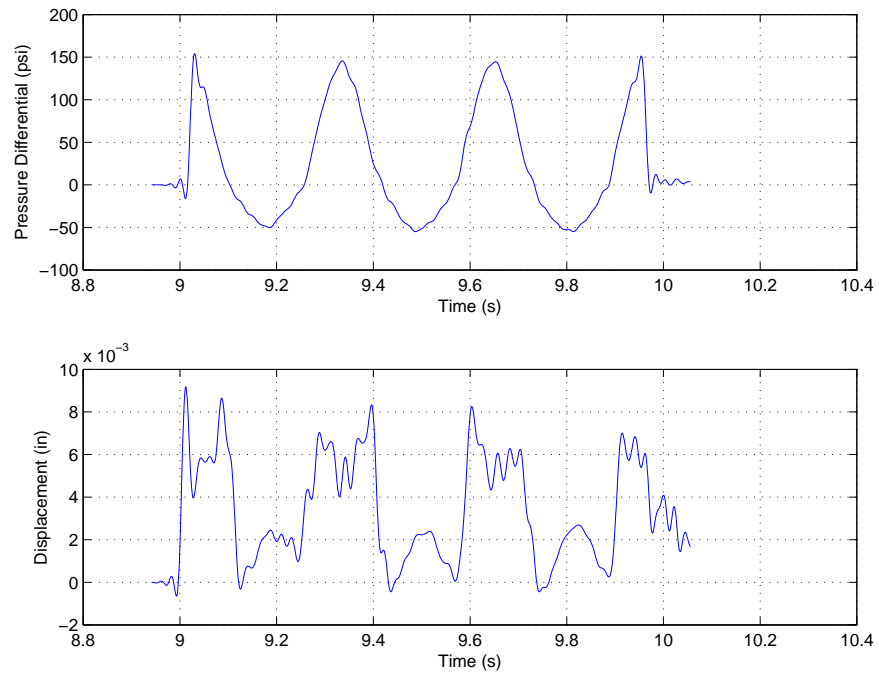
Figure C.10: Filtered displacement and pressure over time for 500 mm/s peak piston speed

134
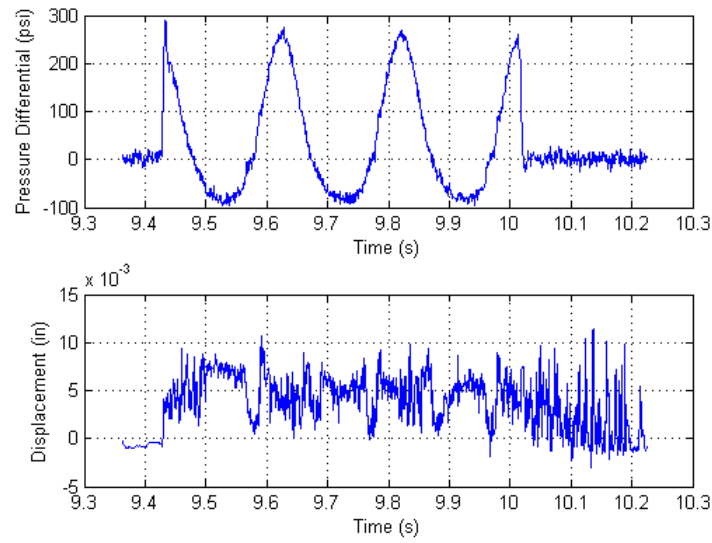
Figure C.11: Displacement and pressure over time for 600 mm/s peak piston speed
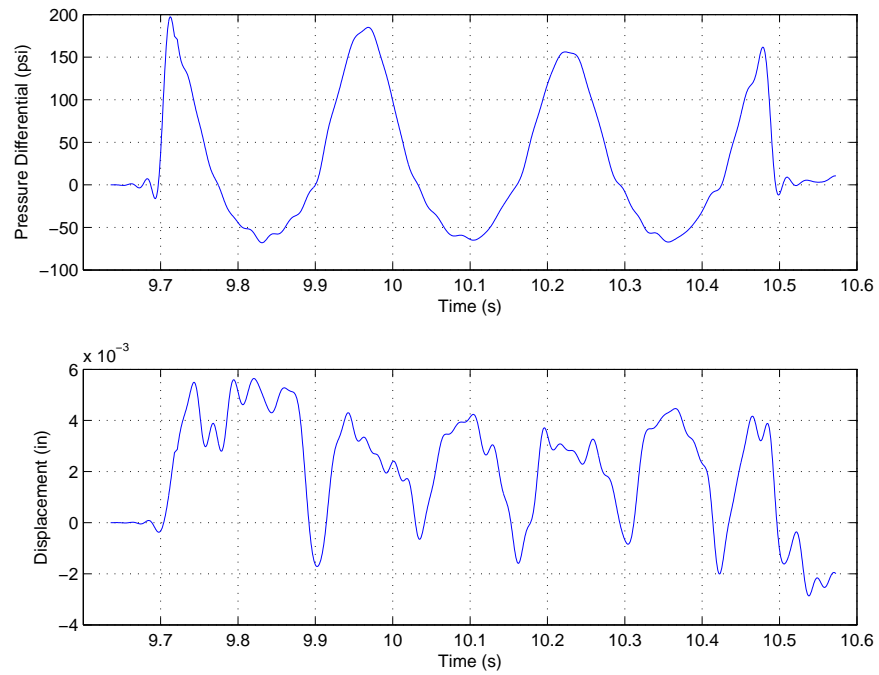
Figure C.12: Filtered displacement and pressure over time for 600 mm/s peak piston speed
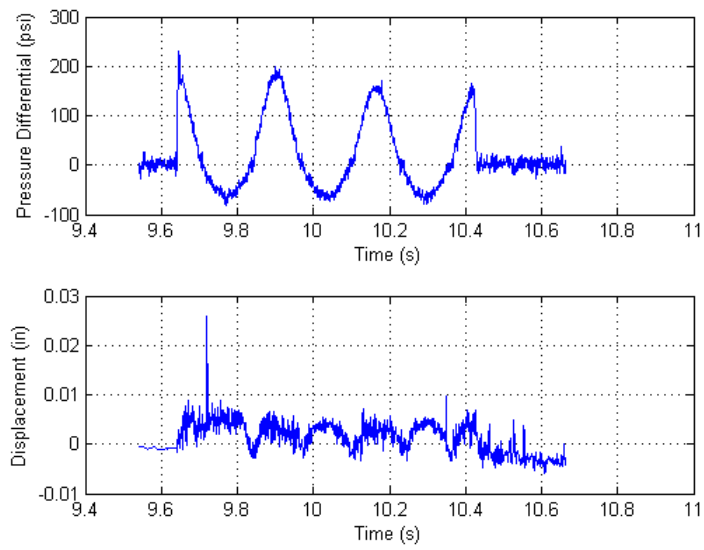
Figure C.13: Displacement and pressure over time for 800 mm/s peak piston speed
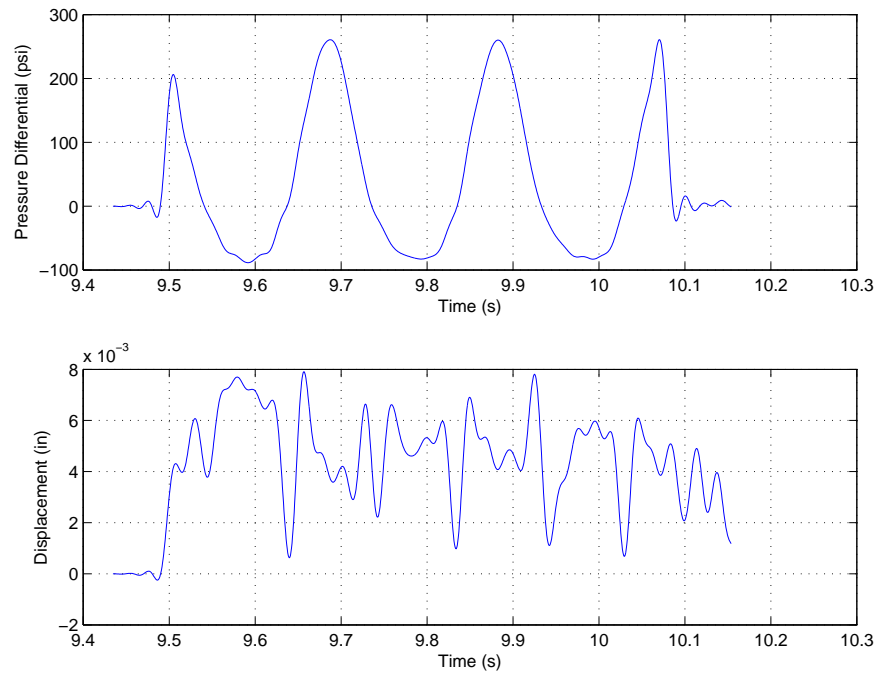
Figure C.14: Filtered displacement and pressure over time for 800 mm/s peak piston speed
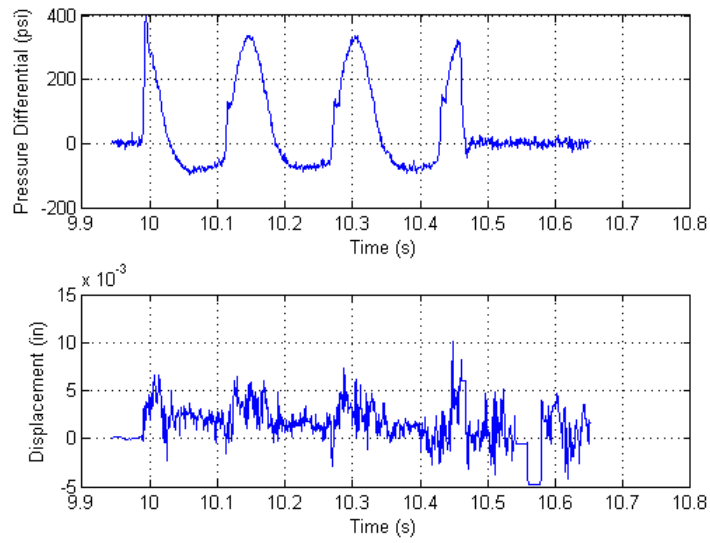
Figure C.15: Displacement and pressure over time for 1000 mm/s peak piston speed

Figure C.16: Filtered displacement and pressure over time for 1000 mm/s peak piston speed

Figure C.17: Displacement Vs Pressure Difference for 100 mm/s peak piston speed
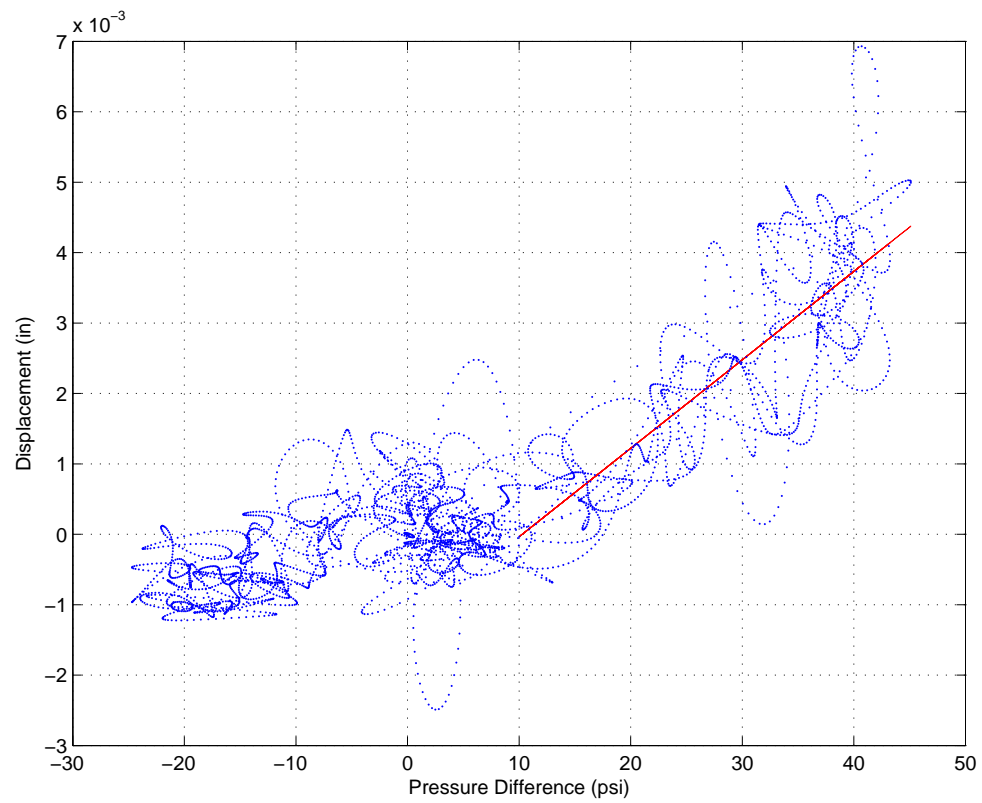
Figure C.18: Displacement Vs Pressure Difference for 200 mm/s peak piston speed
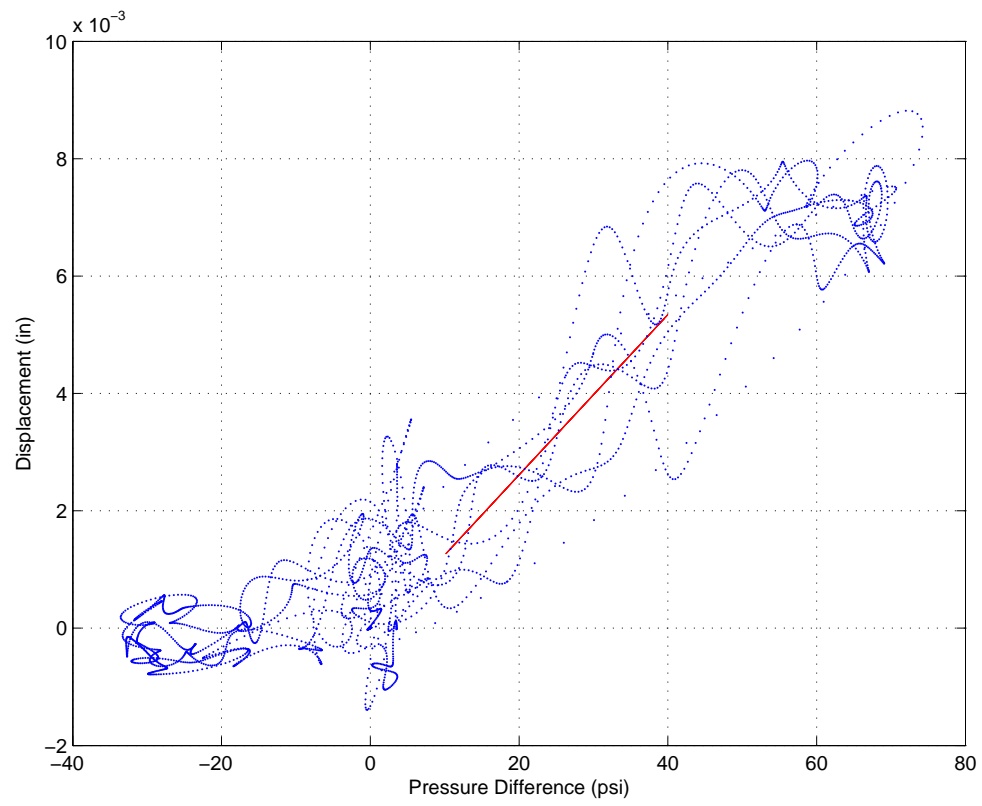
Figure C.19: Displacement Vs Pressure Difference for 300 mm/s peak piston speed
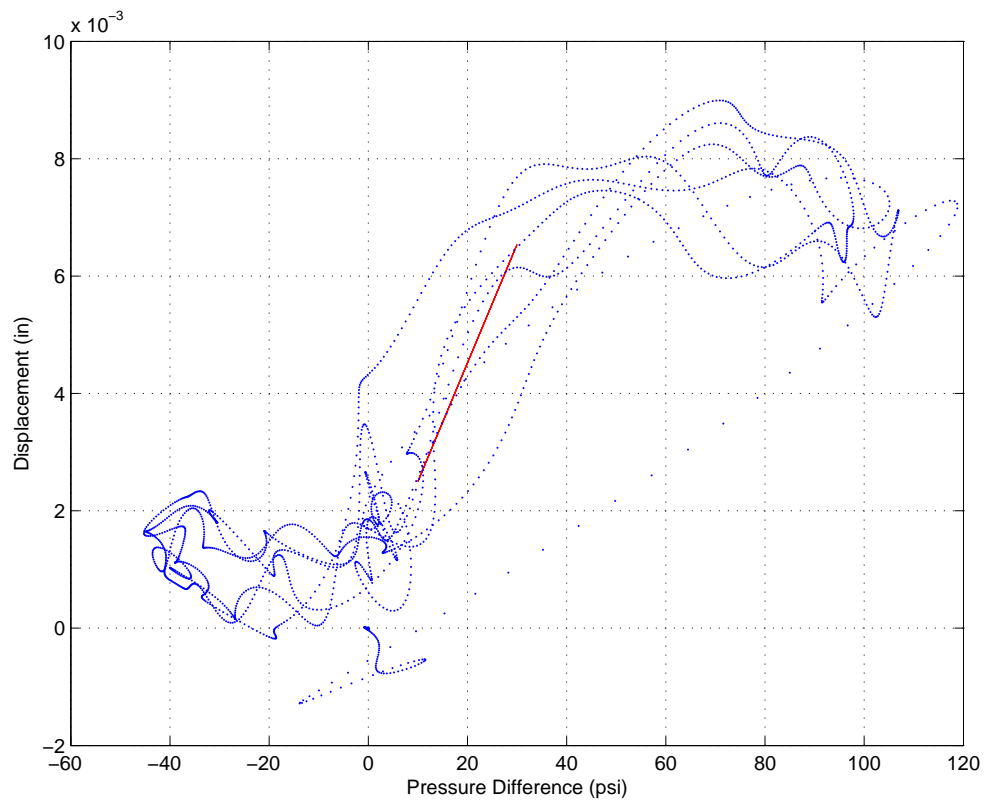
Figure C.20: Displacement Vs Pressure Difference for 400 mm/s peak piston speed
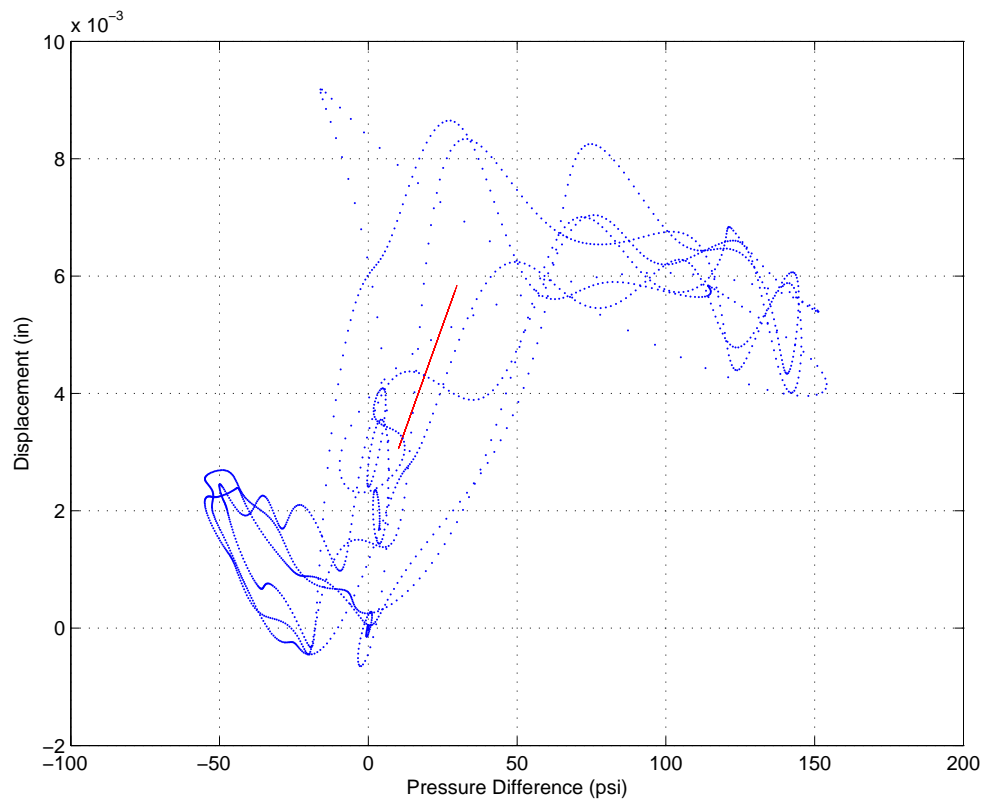
Figure C.21: Displacement Vs Pressure Difference for 500 mm/s peak piston speed
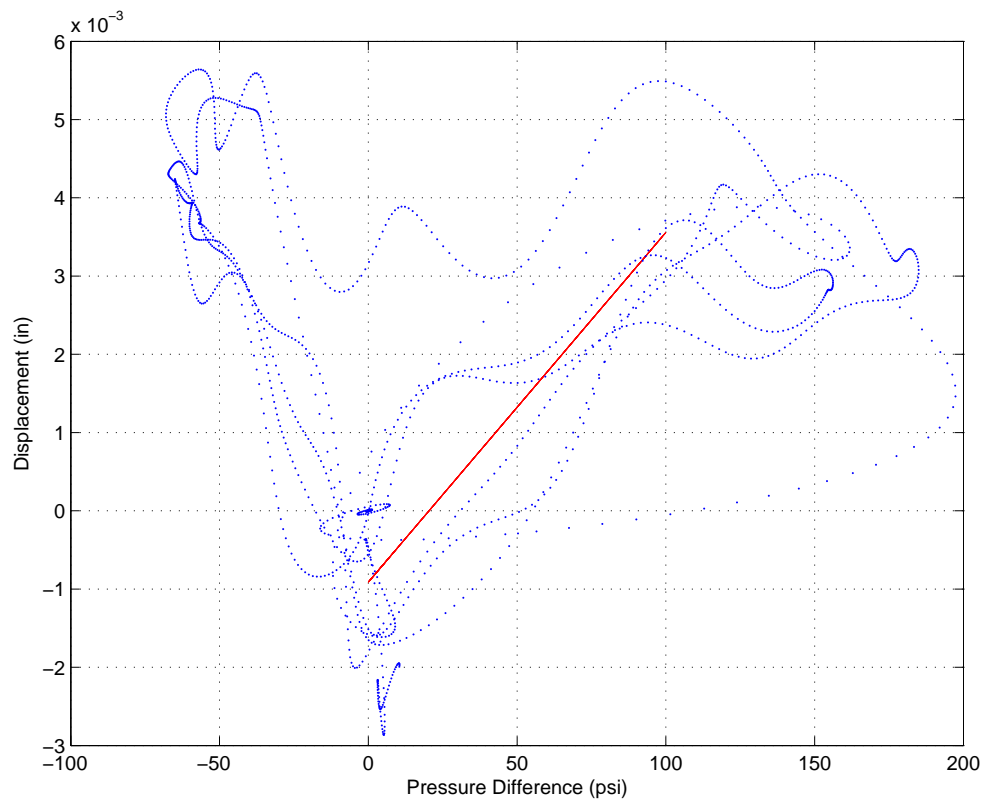
Figure C.22: Displacement Vs Pressure Difference for 600 mm/s peak piston speed
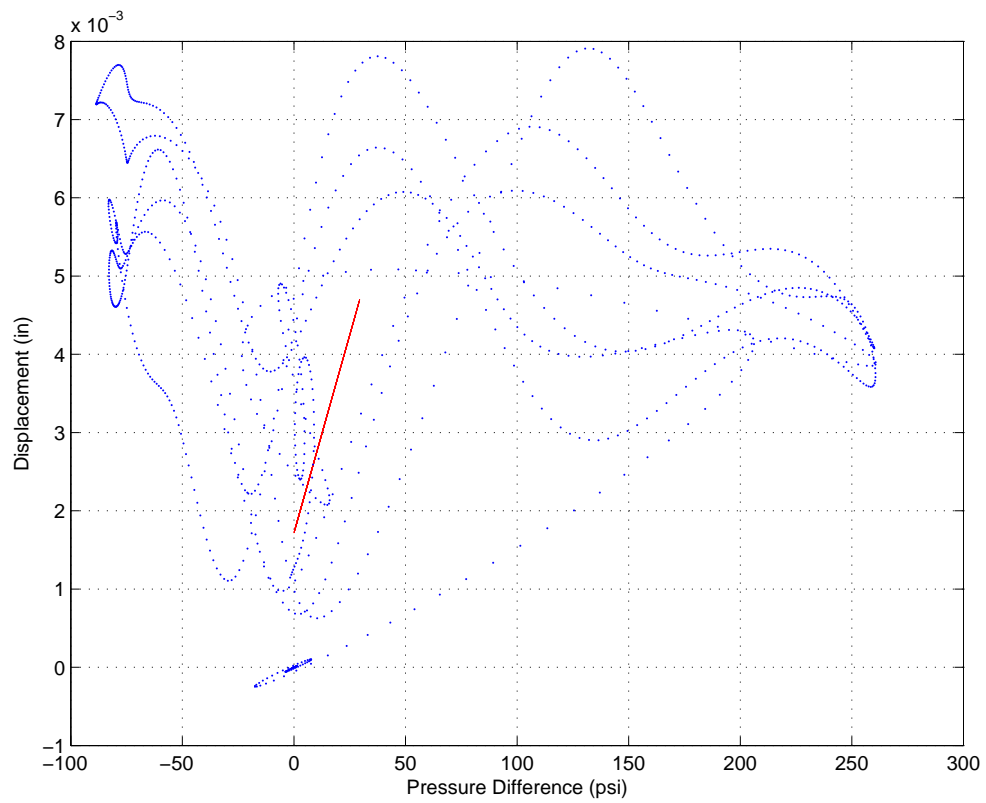
Figure C.23: Displacement Vs Pressure Difference for 800 mm/s peak piston speed
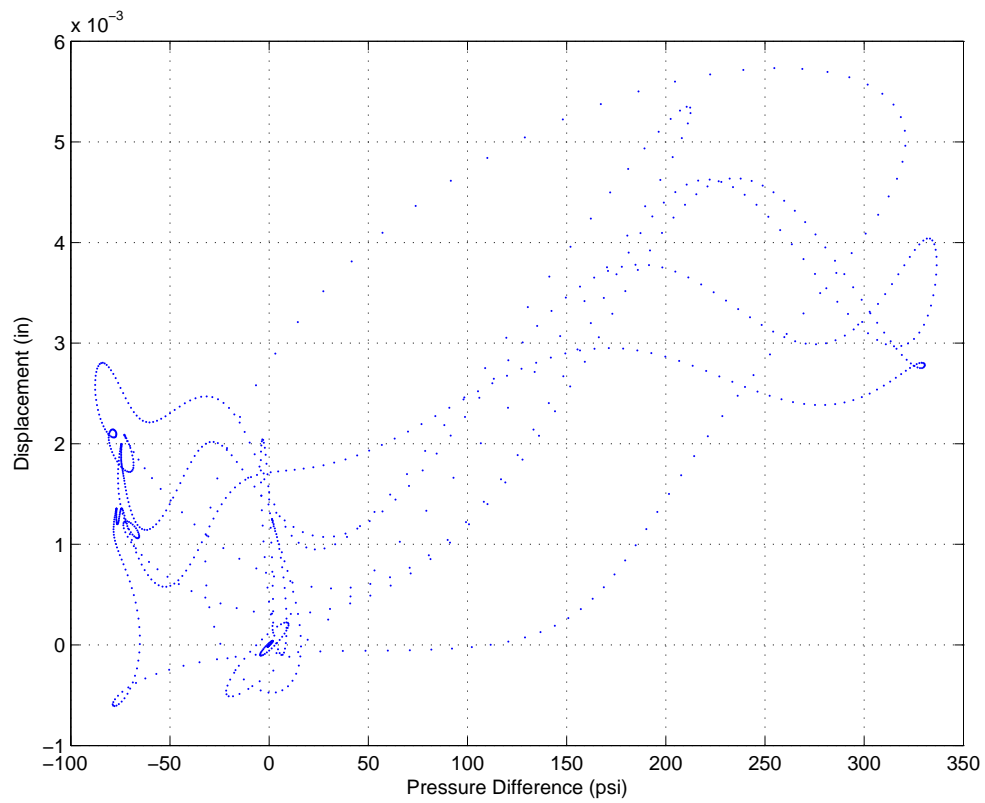
Figure C.24: Displacement Vs Pressure Difference for 1000 mm/s peak piston speed

Appendix D: SCREENSHOTS OF COMPUTATIONAL FLUID DYNAMICS MODEL
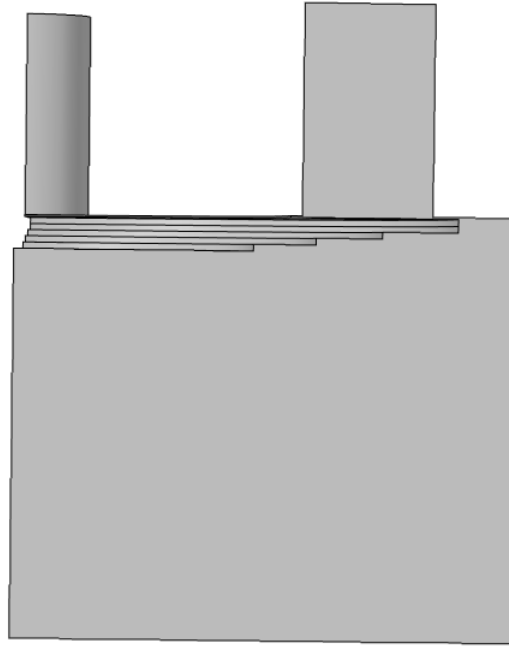
Figure D.1: CFD Model Screen Shot 1
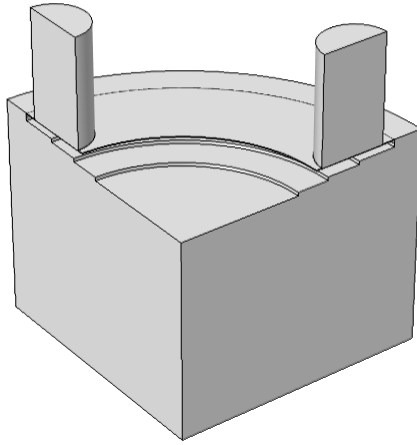
Figure D.2: CFD Model Screen Shot 2
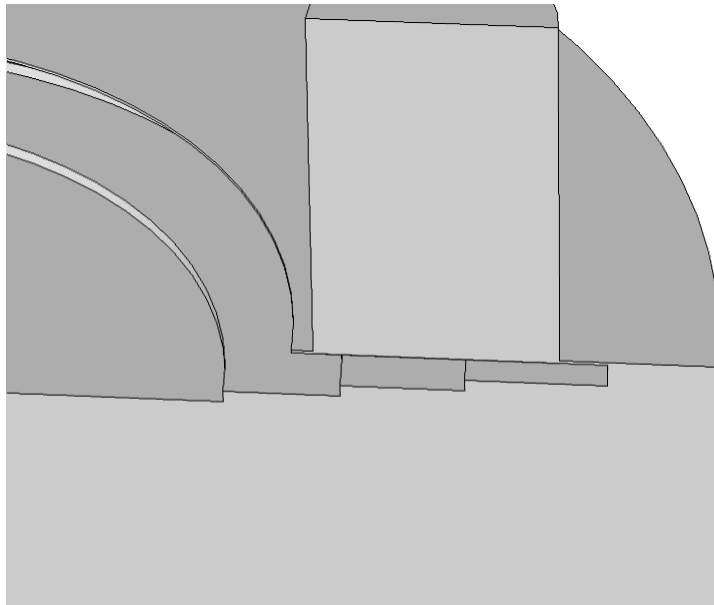
Figure D.3: CFD Model Screen Shot 3
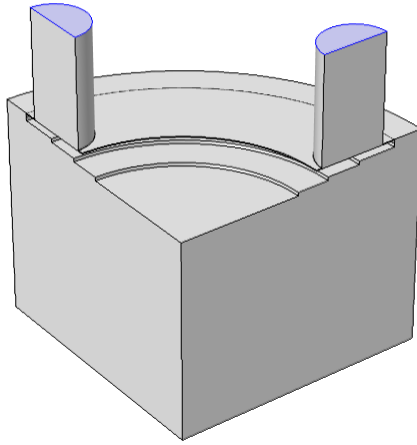
Figure D.4: CFD Model Screen Shot 4
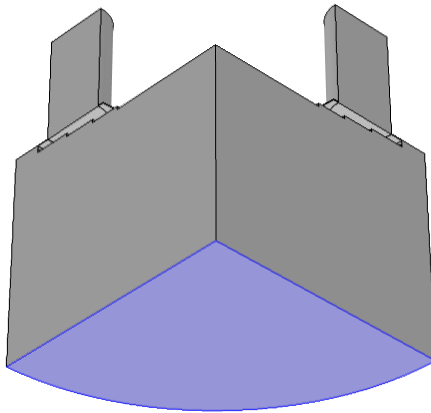
Figure D.5: CFD Model Screen Shot 5
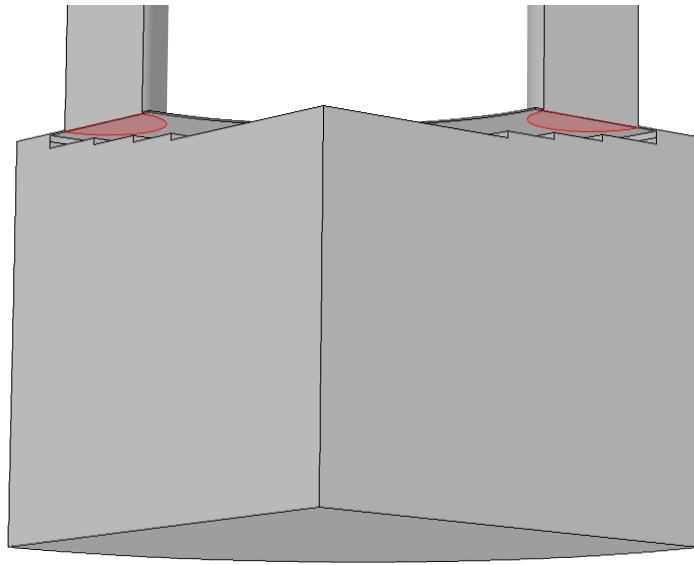
Figure D.6: CFD Model Screen Shot 6
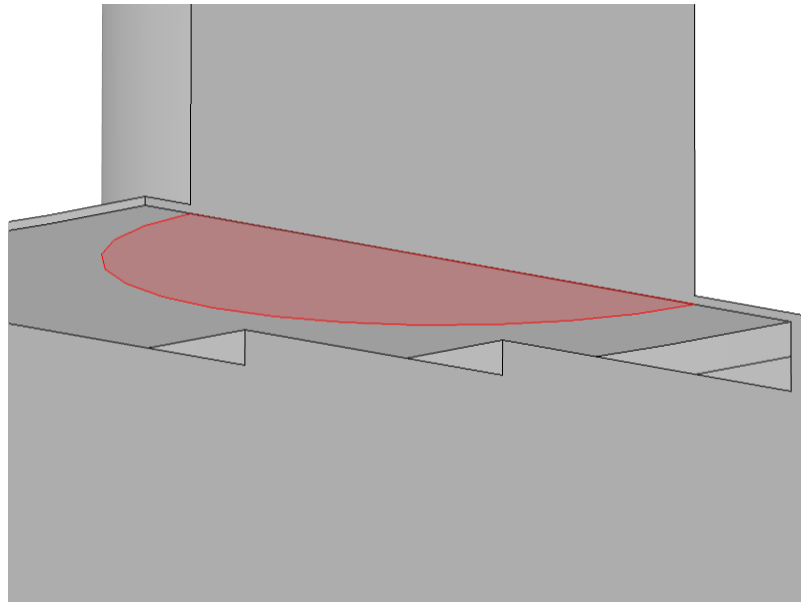
Figure D.7: CFD Model Screen Shot 7
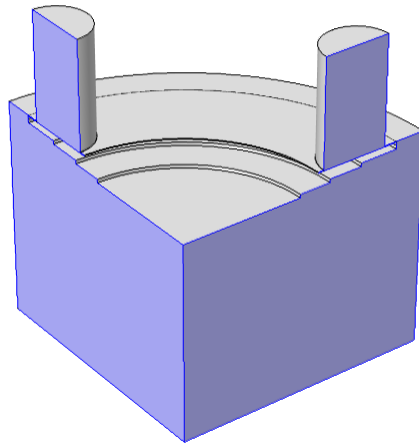
Figure D.8: CFD Model Screen Shot 8

Appendix E: EXPERIMENTAL VALIDATION - FORCE VS. DISPLACEMENT PLOTS
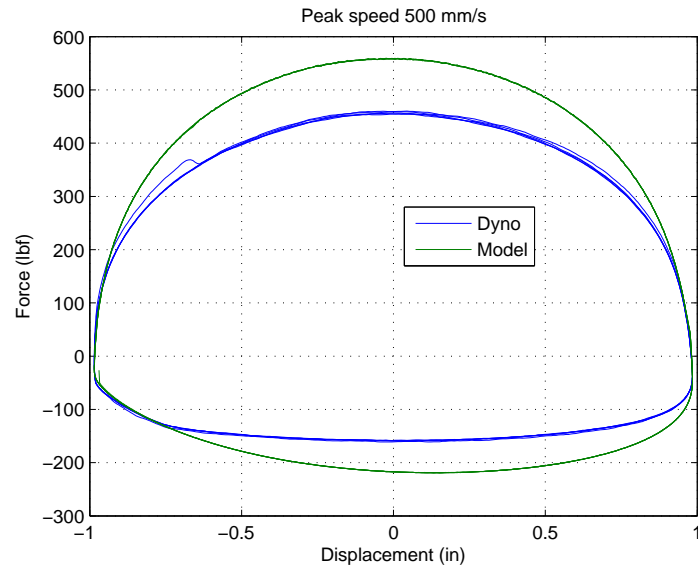
E.1   Mechanical Stiffness
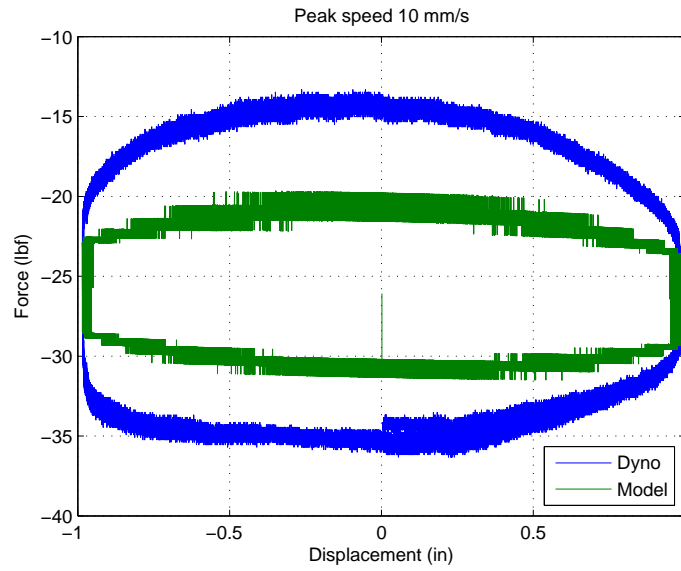
Figure E.1: Experimental validation of 10 mm/s peak speed test using traditional orifice flow equations and mechanical stiffenss values
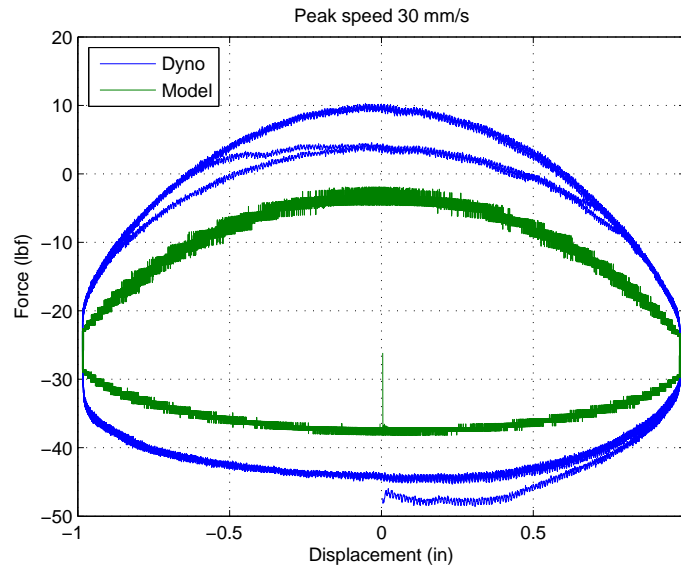
Figure E.2: Experimental validation of 30 mm/s peak speed test using traditional orifice flow equations and mechanical stiffenss values
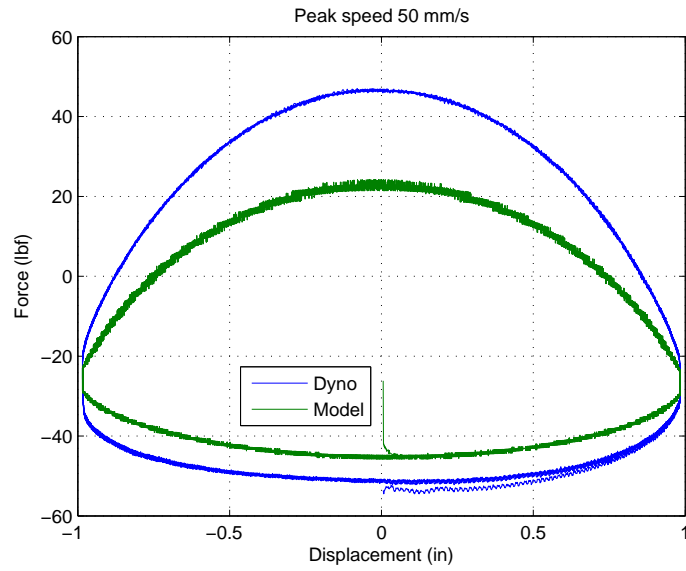
Figure E.3: Experimental validation of 50 mm/s peak speed test using traditional orifice flow equations and mechanical stiffenss values
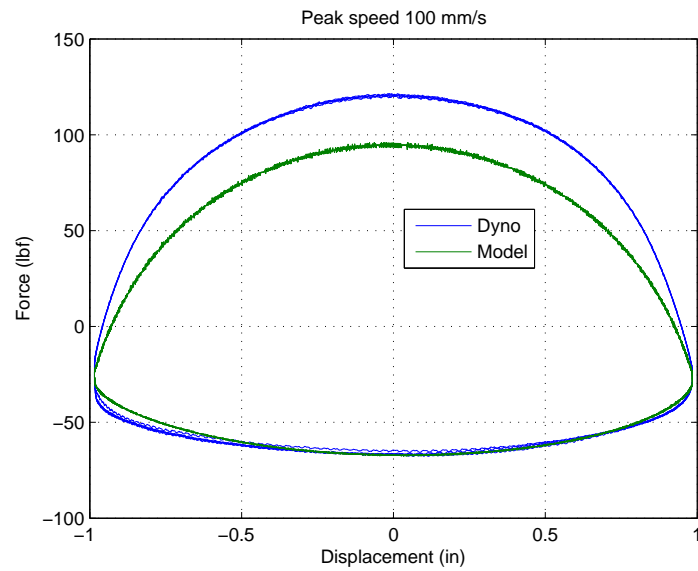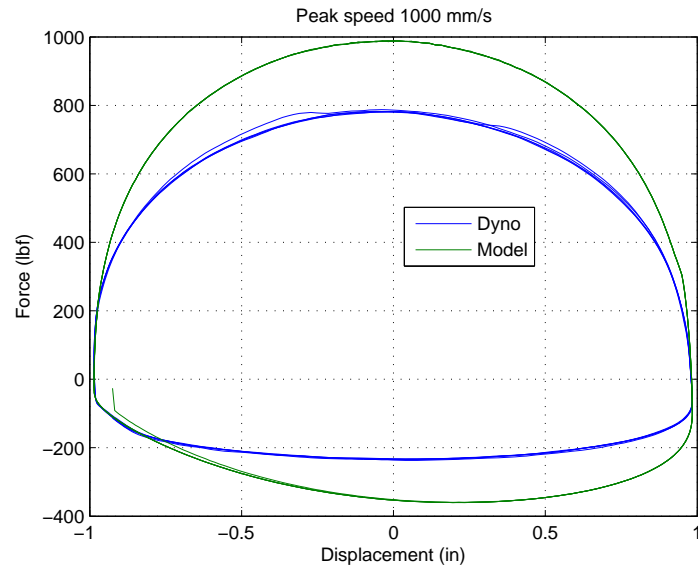

Figure E.4: Experimental validation of 100 mm/s peak speed test using traditional orifice flow equations and mechanical stiffenss values
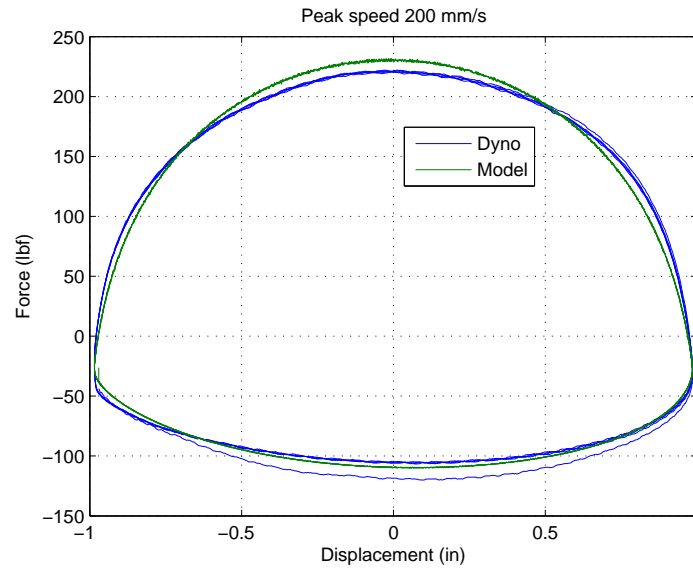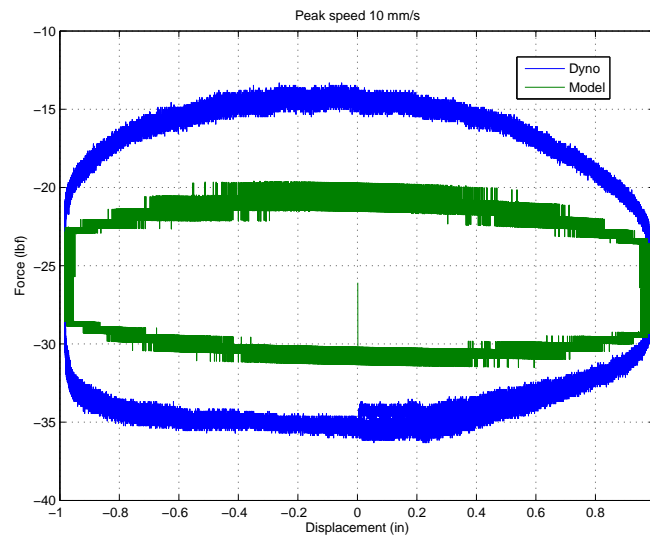
Figure E.5: Experimental validation of 200 mm/s peak speed test using traditional orifice flow equations and mechanical stiffenss values
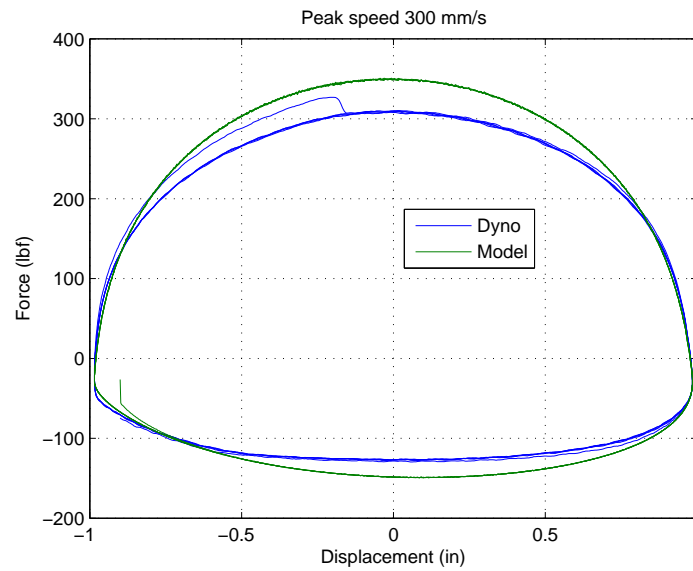
Figure E.6: Experimental validation of 300 mm/s peak speed test using traditional orifice flow equations and mechanical stiffenss values

Figure E.7: Experimental validation of 500 mm/s peak speed test using traditional orifice flow equations and mechanical stiffenss values

Figure E.8: Experimental validation of 1000 mm/s peak speed test using traditional orifice flow equations and mechanical stiffenss values
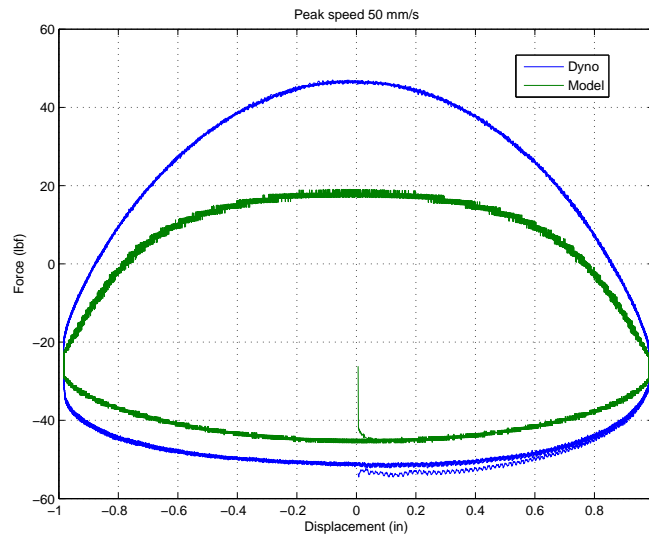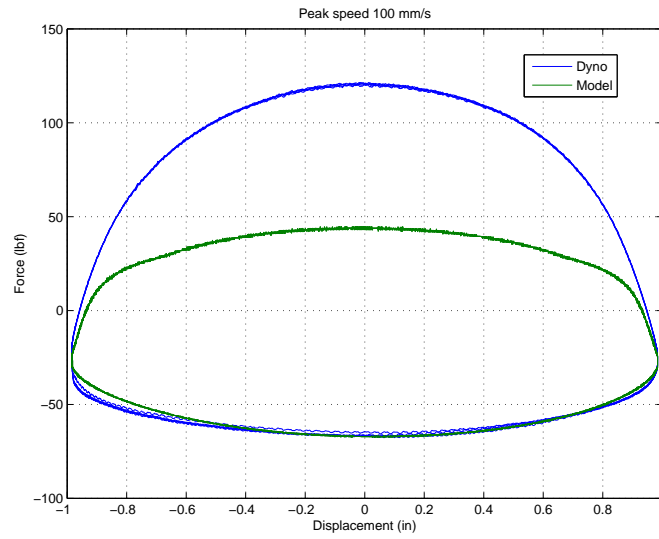
E.2 Fluid Stiffness

Figure E.9: Experimental validation of 10 mm/s peak speed test using empirical flow equations and fluid stiffenss values
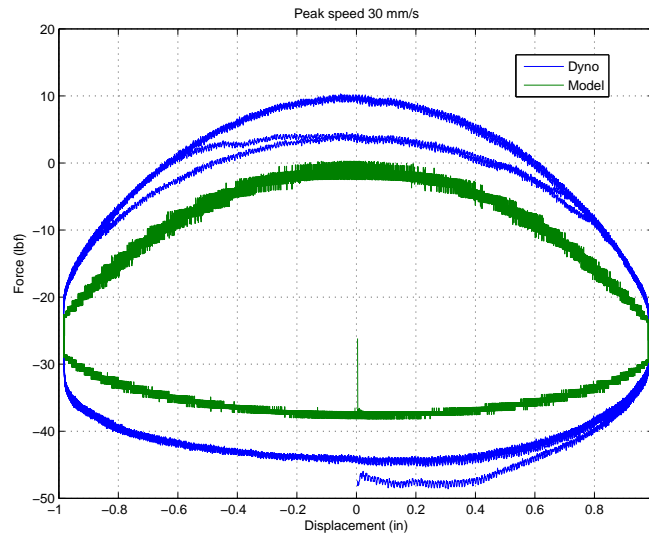
Figure E.10: Experimental validation of 30 mm/s peak speed test using empirical flow equations and fluid stiffenss values
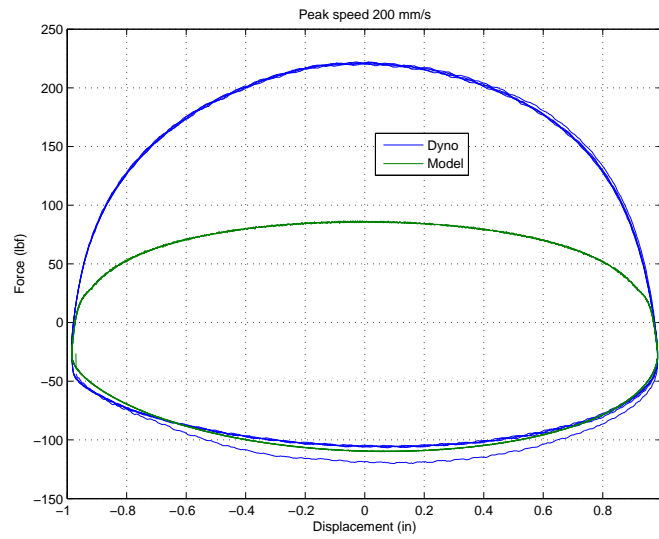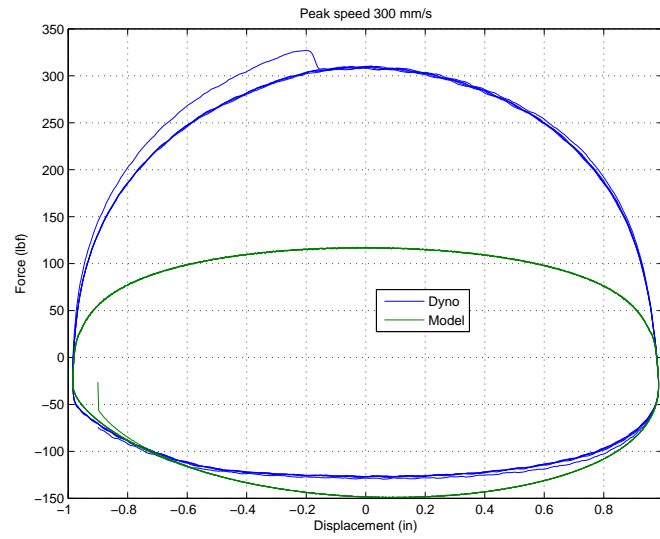

Figure E.11: Experimental validation of 50 mm/s peak speed test using empirical flow equations and fluid stiffenss values

Figure E.12: Experimental validation of 100 mm/s peak speed test using empirical flow equations and fluid stiffenss values
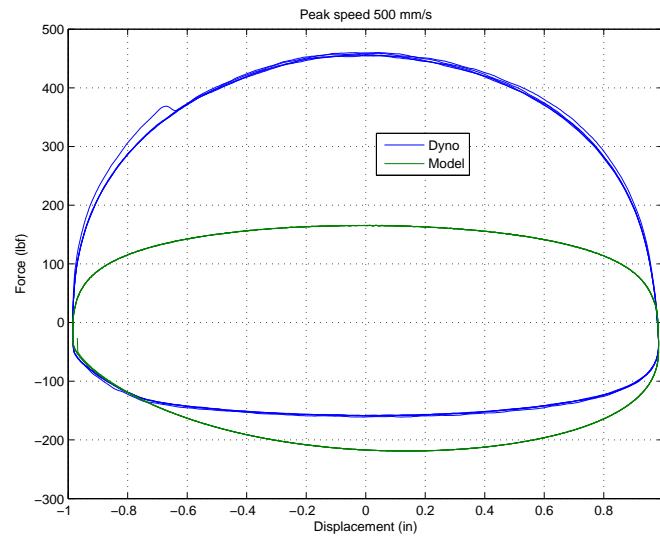

Figure E.13: Experimental validation of 200 mm/s peak speed test using empirical flow equations and fluid stiffenss values

Figure E.14: Experimental validation of 300 mm/s peak speed test using empirical flow equations and fluid stiffenss values

Figure E.15: Experimental validation of 500 mm/s peak speed test using empirical flow equations and fluid stiffenss values
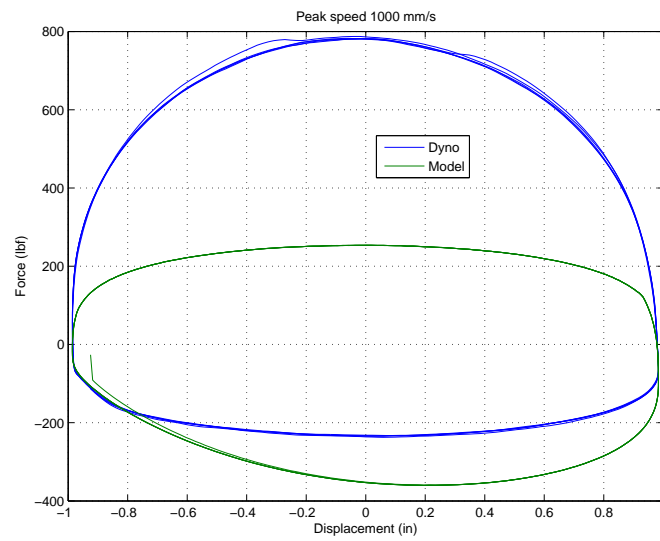
Figure E.16: Experimental validation of 1000 mm/s peak speed test using empirical flow equations and fluid stiffenss values

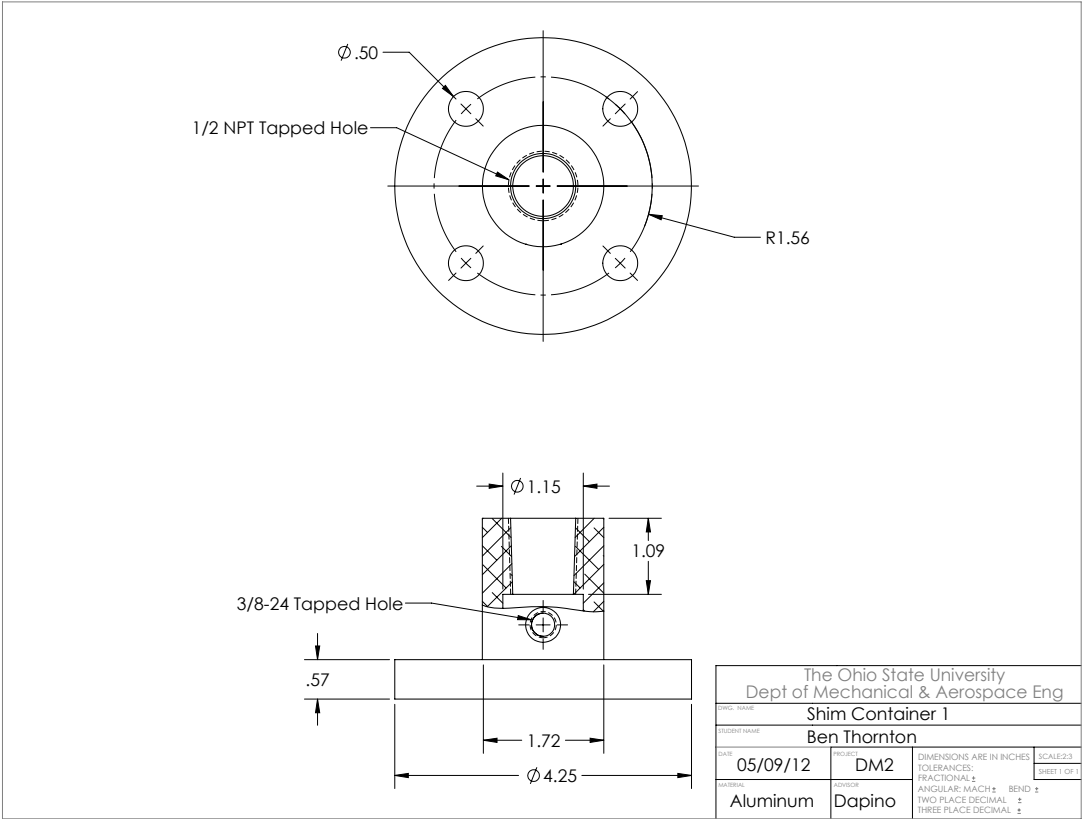# Appendix F: SHIM CONTAINER DRAWINGS
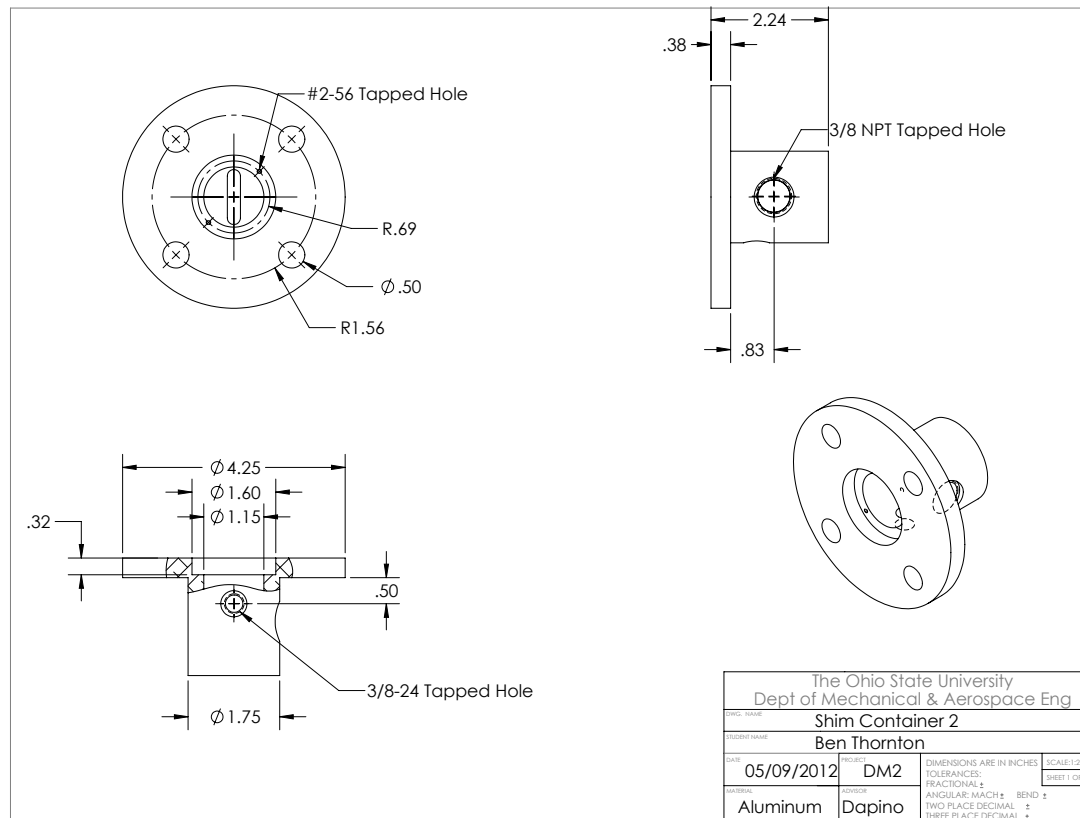

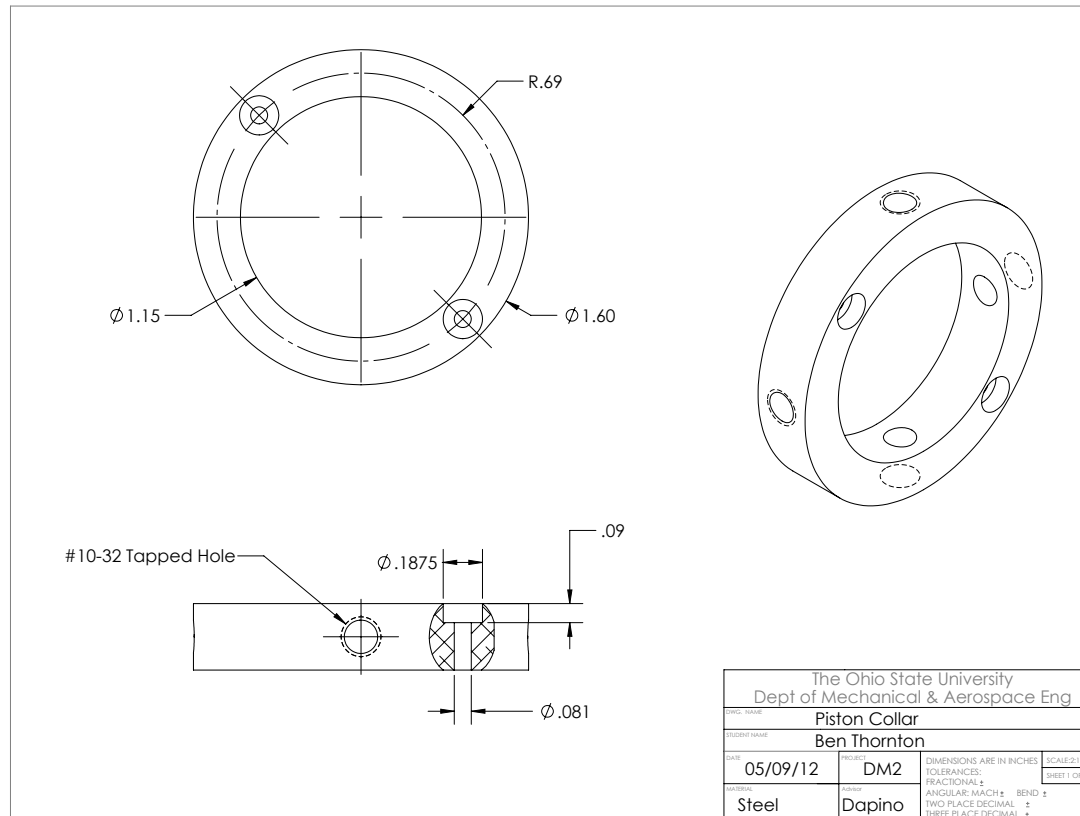Figure F.1: Drawing of Shim Container Part 1

Figure F.2: Drawing of Shim Container Part 2

Figure F.3: Drawing of Piston Collar